2009

Thermo-mechanical Characterization Of High-temperature Shape Memory Ni-ti-pd Wires

Matthew Fox
University of Central Florida

THERMO-MECHANICAL CHARACTERIZATION OF HIGH-TEMPERATURE SHAPE MEMORY Ni-Ti-Pd WIRES

by

MATTHEW D. FOX
B.S. University of Central Florida, 2007

A thesis submitted in partial fulfillment of the requirements
for the degree of Master of Science
in the Department of Mechanical, Materials and Aerospace Engineering
in the College of Engineering and Computer Science
at the University of Central Florida
Orlando, Florida

Summer Term
2009

ABSTRACT

Actuator applications of shape memory alloys have typically been limited by their phase transformation temperatures to around 100 degrees C. However, recently with a focus on aerospace and turbomachinery applications there have been successful efforts to increase the phase transformation temperatures. Several of these alloy development efforts have involved ternary and quaternary elemental additions (e.g., Pt, Pd, etc.) to binary NiTi alloys. Experimentally assessing the effects of varying composition and thermo-mechanical processing parameters can be cost intensive, especially when expensive, high-purity elemental additions are involved. Thus, in order to save on development costs there is value in establishing a methodology that facilitates the fabrication, processing and testing of smaller specimens, rather than larger specimens from commercial billets. With the objective of establishing such a methodology, this work compares thermo-mechanical test results from bulk dog-bone tensile $Ni_{29.5}Ti_{50.5}Pd_{20}$ samples (7.62 mm diameter) with that of thin wires (100 μm-150 μm diameter) extracted from comparable, untested bulk samples by wire electrical-discharge machining (EDM). The wires were subsequently electropolished to different cross-sections, characterized with Scanning Electron Microscopy, Transmission Electron Microscopy and Energy Dispersive X-Ray Spectroscopy to verify the removal of the heat affected zone following EDM and subjected to Laser Scanning Confocal Microscopy to accurately determine their cross-sections before thermo-mechanical testing. Stress-strain and load-bias experiments were then performed on these wires using a dynamic mechanical analyzer and compared with results established in

previous studies for comparable bulk tensile specimens. On comparing the results from a bulk tensile sample with that of the micron-scale wires, the overall thermomechanical trends were accurately captured by the micron-scale wires for both the constrained recovery and monotonic tensile tests. Specifically, there was good agreement between the stress-strain response in both the martensitic and austenitic phases, the transformation strains at lower stresses in constrained recovery, and the transformation temperatures at higher stresses in constrained recovery. This work thus validated that carefully prepared micron-diameter samples can be used to obtain representative bulk thermo-mechanical properties, and is useful for fabricating and optimizing composition and thermomechanical processing parameters in prototype button melts prior to commercial production. This work additionally assesses potential applications of high temperature shape memory alloy actuator seals in turbomachinery. A concept for a shape memory alloy turbine labyrinth seal is also presented. Funding support from NASA's Fundamental Aeronautics Program, Supersonics Project (NNX08AB51A) and Siemens Energy is acknowledged.

Dedicated to my family and friends, who have

given me unwavering support, encouragement,

and advice throughout my education.

ACKNOWLEDGMENTS

I would like to express my thanks and sincere gratitude to my advisor and mentor during my graduate research at the University of Central Florida, Dr. Raj Vaidyanathan. Without his undying drive to make every student that he advises better than they ever knew they could be, I would not be the person I am today.

My sincere gratitude also goes out to Dr. Kevin Coffey, Dr. C Suryanarayana and Dr. Ali Gordon for their sound advice and guidance during my graduate studies and for serving on my defense committee. I would also like to extend my sincere thanks to all of the students in our group who have provided great knowledge, wisdom, and most importantly, friendship, to me during my time here at UCF as a graduate student. I would especially like to express my gratitude to R. Mahadevan Manjeri for his great help in assisting me in all of my SEM and TEM investigations that I have presented in this work, and Glen Bigelow for providing the raw data for his bulk thermo-mechanical measurements of NiTiPd which I used in this work. I would also like to acknowledge the AMPAC administrative staff, Ms. Cynthia Harle, Ms. Karen Glidewell, Ms. Angelina Feliciano, and Ms. Kari Stiles for all of their great work, and for assisting me throughout my graduate studies. Without them, we would all be lost and confused.

Most importantly, I would like to express my absolute love and respect for my family and friends who have made my life so much more enjoyable and meaningful. Without their support, guidance and love, I would never have become the person I am today, or the person I hope to be in the future.

TABLE OF CONTENTS

LIST OF FIGURES

LIST OF TABLES

LIST OF ACRONYMS/ABBREVIATIONS

A_f	Austenite Finish
A_s	Austenite Start
BSE	Back Scattered Electron
CNC	Computer Numerical Controlled
DARPA	Defense Advanced Research Projects Agency
DMA	Dynamic Mechanical Analysis/Analyzer
DSC	Differential Scanning Calorimetry
EDM	Electrical-discharge Machining
EDS	Energy Dispersive Spectroscopy
EDX	Energy Dispersive X-ray Spectroscopy
FIB	Focused Ion Beam
HAZ	Heat-affected Zone
HTSMA	High-temperature Shape Memory Alloy
LED	Light Emitting Diode
LSCM	Laser Scanning Confocal Microscopy/Microscope
M_d	Martensite Desist
M_f	Martensite Finish
M_s	Martensite Start
NASA	National Aeronautics and Space Administration

PMMA	Poly-methyl Methacrylate
RMS	Root-mean Square
SE	Superelasticity
SEM	Scanning Electron Microscopy
SMA	Shape Memory Alloy
SME	Shape Memory Effect
STEM	Scanning Transmission Electron Microscopy
TEM	Transmission Electron Microscopy

CHAPTER ONE: INTRODUCTION

1.1 Motivation

NiTi shape memory alloys SMA have the ability to undergo a reversible, thermoelastic phase transformation between a low-temperature (B19') martensite phase and a high-temperature (B2) austenite phase. The martensite phase has a crystallographically twinned structure that can accommodate large strains by detwinning, and when heated to the (B2) austenite structure will return to the original macroscopic shape it had prior to deformation, even against an externally applied stress. This ability allows NiTi to be used in actuator applications, where it can perform work during the reverse transformation from martensite to austenite. Binary NiTi alloys are the most commonly used shape memory alloys in commercial actuator applications, though the transformation temperatures of binary NiTi do not exceed 120°C [Otsuka & Wayman 1998]. NiTi-based shape memory alloys have received much attention for their potential application in the fields of aerospace and turbomachinery engineering [Rey *et al*. 2001, Padula *et al*. 2007, Lattime & Steinetz 2002], though raising the operating temperature of these NiTi-based alloys is needed to make them operable as actuators in the environments present in some of those applications.

Alloying can significantly raise the transformation temperatures of NiTi, and both platinum and palladium have been considered some of the most promising ternary additions to NiTi for increasing these transformation temperatures [Noebe *et al*. 2006]. In order to certify the use of ternary NiTi-(Pd, Pt) alloys in actuators, they have to first be evaluated for their thermo-

mechanical performance [Bigelow *et al*. 2008], though the cost of producing large billets with upwards of 40 at% (Pd, Pt) can prove very expensive. Establishing a methodology that optimizes the compositional and thermo-mechanical processing parameters on small-scale button melts (~30 g) prior to large-scale commercial production would save money on developmental costs of novel high-temperature shape memory alloys. Such a methodology would require a comparative study between thermo-mechanical data sets from both bulk specimens machined out from large billets and micron-scale wires extracted from much smaller button melts, which is the primary focus of this work. In the process of achieving the above mentioned objective, any size-scale or geometry effects that were observed between the bulk tensile specimens and micron-scale wires were examined. This work additionally assesses some potential areas in turbomachinery where HTSMA actuator seals can be implemented. A concept for a shape memory turbine labyrinth seal is also presented.

1.2 Shape Memory Alloys

Shape memory alloys (SMAs) are a unique group of alloys that can undergo a solid-solid phase transformation between a low-symmetry martensite phase to a high-symmetry austenite phase [Orgéas and Favier 1998]. The crystallographically twinned martensite phase is able to accommodate large amounts of strain by means of detwinning, which it can then recover by a transformation to its parent phase, austenite (Fig. 1.1). This phase transformation can be accomplished by various means; such as changing temperature, stress, or even by application of a magnetic field for some SMAs [Otsuka & Wayman 1998]. When the SMA goes through the

reverse transformation upon heating from martensite to austenite it can return to the original macroscopic shape it had prior to deformation induced by elastic straining, coupled with detwinning-related processes, even against an applied external stress. This unique ability gives SMA the capability to play the role of both sensor and actuator for certain applications.

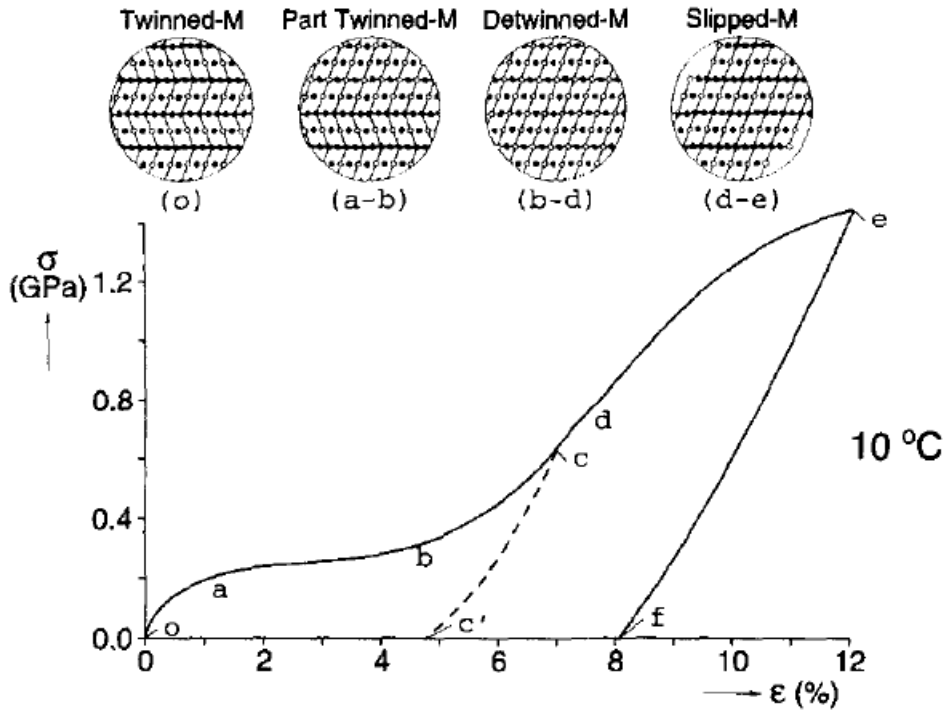

Figure 1.1: Ability of NiTi to accommodate large strains by means of detwinning in martensite [Shaw and Kyriakides 1995]

The shape memory effect (SME) was first discovered as early as the 1930s in the Au-Cd system, and then later discovered in the NiTi system in 1963 at the United States Naval Ordnance Laboratories [Otsuka & Wayman 1998]. NiTi alloys are the most widely used SMAs, as they are applied to many different fields of use; such as eyeglass frames, biomedical implants, orthodontics, robotics, and actuators. SMAs either use the shape memory effect or superelasticity (SE). SME can be utilized by keeping the alloy under a bias stress and cycling it through its phase transformation temperatures to provide a designed, repeatable displacement. SE can be utilized by stressing the alloy while it is in the austenite phase, whereby it will revert to a stress-induced, detwinned martensite phase [Otsuka & Ren 2005]. By releasing that stress the material will revert back to the austenite phase, and its original shape, without accumulating any residual plasticity.

1.2.1 Shape Memory Effect

The shape memory effect arises due to a diffusion-less, solid phase transformation where the material can be deformed in its low-temperature phase, martensite, and when heated past a certain higher temperature will return to its original shape in the higher temperature, austenite phase (Fig. 1.2). The "remembered" shape in the austenite phase can be chosen by the user and trained into the material before any deformation is to take place.

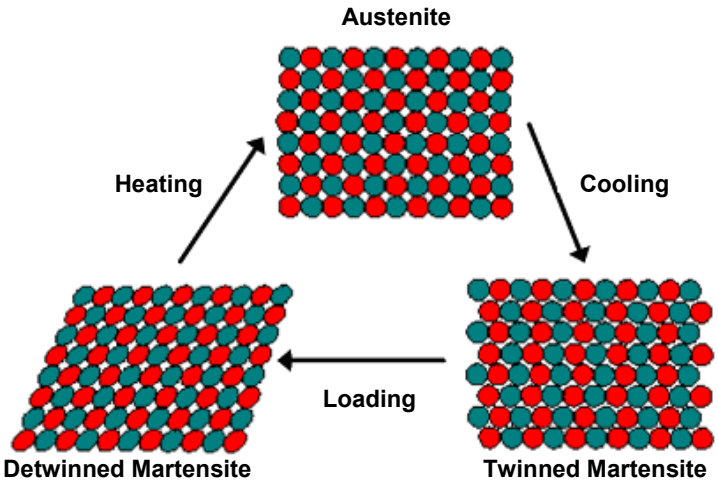

Figure 1.2: Atomic arrangements in the shape memory effect

The transformation process is determined by the transformation temperatures of the material. There is an austenite start temperature (A_s), an austenite finish temperature (A_f), a martensite start temperature (M_s), and a martensite finish temperature (M_f). This means that the material begins transforming into one of the two phases at the start temperature, and will be completely in that particular phase once the finish temperature is reached. If the material is being heated to austenite it will start transforming at the A_s temperature and complete the austenitic transformation at the A_f temperature, and if being cooled from austenite will start transforming into martensite at the M_s temperature and complete the martensitic transformation at the M_f temperature (Fig. 1.3). The gap between transformation paths between the two phases for the material is called the hysteresis. For actuator applications it is usually beneficial to have the hysteresis be as small as possible, since quick actuation is usually desired at a given temperature.

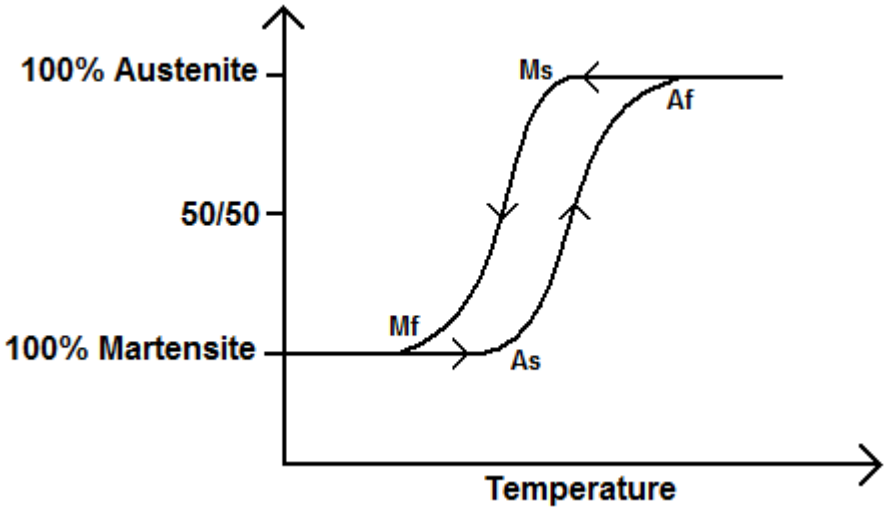

Figure 1.3: Transformation path for thermally induced phase transformation; where M_s is the martensitic start temperature, M_f is the martensitic finish temperature, A_s is the austenitic start temperature, and A_f is the austenitic finish temperature

Some shape memory alloys can even obtain a two-way shape memory effect, where the alloy remembers not only its high-temperature austenite shape, but its low-temperature martensite shape as well. This can be accomplished by many different experimental paths, though each one links back to the creation of internal stress fields in the austenitic phase which controls both the austenitic and martensitic phase transformations [Funakubo 1987].

1.2.2 Superelasticity

Certain shape memory alloys have the ability to behave "pseudo-elastically", when the alloy is at a temperature slightly above the A_f. These shape memory alloys have a martensite desist (M_d) temperature that is higher than the A_f temperature. This means it can accommodate

large strains under an applied stress by undergoing an isothermal phase transformation from the austenite phase to a detwinned martensite structure, without the accumulation of plasticity [Miura *et al*. 1986]. When the stress is released it reverts back to the austenitic phase and returns to its original shape due to the stress-induced martensite phase no longer being energetically stable at that temperature under no load (Fig. 1.4).

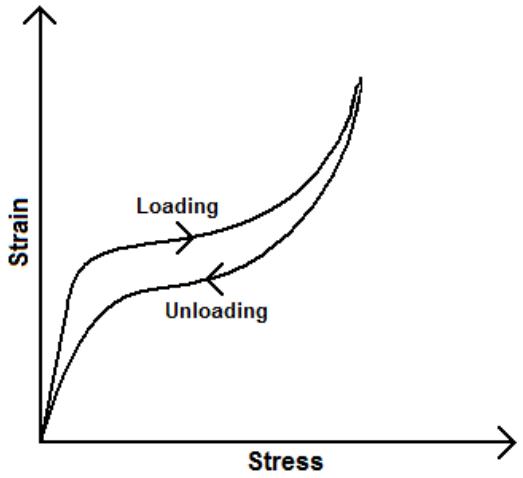

Figure 1.4: Superelastic response of NiTi

1.3 Applications of Shape Memory Alloys

The shape memory and superelastic effects are both used in various applications of SMAs. The shape memory effect requires biasing stress and thermal fluctuations to be viable actuators, and the superelastic effect requires the material to be in a certain temperature range to utilize its unique properties.

One of the first prominent applications of SMAs using the shape memory effect was in 1971, when a low-temperature NiTiFe *Cryofit* coupling was applied to connect titanium piping in a high-pressure hydraulic system on an F-14 fighter jet [Humbeeck 1999]. This successful demonstration in 1970 can be seen as the catalyst for engineering interest in SMAs, as a multitude of patents have since been filed that involve the use of SMAs [Wu *et al.* 2000].

The superelastic effect in NiTi was proposed as a viable dental arch wire material in 1986 [Miura *et al.* 1986]. Dental arch wires used in braces and other dental devices use NiTi-based alloys to provide the same effect steel wires do, with less fatigue and higher reliability. Miura *et al* suggested that superelastic NiTi could provide a wide range of stresses needed for these arch wires depending on the heat treatment used for shape-setting, and was least likely to undergo permanent deformation over time as compared to other alloys being used as dental arch wires.

Intravascular NiTi stents were first conceived of in 1983, and were tested for years on several different species of animals for their resistance to corrosion [Ryhanen 1999]. Stents are comprised of a wire mesh in the shape of a tube that is inserted into a clogged artery to keep the blood flowing through what used to be a blocked, or partially blocked, area. Stents utilize the superelastic effect by being deformed into a catheter and when it is released into an artery will expand and push on the blockage to expand the walls of the artery to open it. Since the mid-90s stents have been used extensively in humans, and have been scientifically proven to provide adequate function and excellent fatigue resistance, without invasive surgery [Berg 2008].

1.4 Electrical-Discharge Machining

Electrical-discharge machining (EDM) is a method used to cut hard materials that would otherwise require careful machining techniques. EDM requires the material being cut to be electrically conductive because EDM does not machine by conventional means, but locally melts small craters in succession using high-frequency electrical pulses between the electrode and the material. Wire-EDM uses the same principle, except the electrode used is a wire, and can locally melt along a line instead of a point or area (Fig. 1.5).

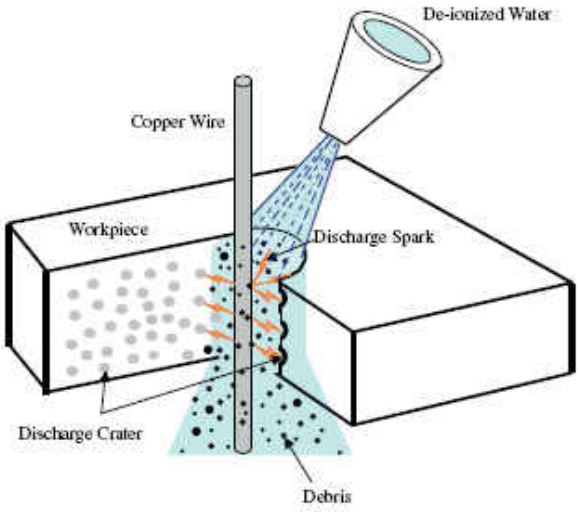

Figure 1.5: Material removal schematic for wire-EDM [Hsieh *et al.* 2009]

EDM produces a heat-affected zone (HAZ) on the surface of the material due to the rapid melting and solidification of the material. The thickness and composition of this zone for NiTi-based alloys has been shown to vary depending on the process parameters, and the surface roughness of the samples were also shown to vary depending on these parameters [Lin *et al.* 2001, Theisen *et al.* 2004, Hsieh *et al.* 2009].

1.5 Electropolishing

Electropolishing is an electrochemical etching process that smoothes the surfaces of metal parts. The part is submerged in an electrolytic bath, and serves as the anode when a direct current is applied to the part. The tank also contains cathodes to complete the circuit. When the current is applied, an anodic film will form on the surface of the part, with it being thicker at the surface, and thinner on the protrusions from the surface. This means that a higher current density will be present on the peaks and will be etched away faster than the surface, hence, smoothing the part. Electropolishing is used on NiTi parts to debur, decrease surface roughness, provide a shiny surface, to passivate the part, or a combination of the aforementioned. Electropolishing medical instruments and implants are especially important. Not only does the surface need to be completely deburred if it is going to be put into the human body, but a thin titanium dioxide film is formed on the surface during electropolishing that acts to prevent oxidation and corrosion, and to prevent toxic nickel from diffusing into the body. As previously mentioned in Section 1.4, the surface roughness of a part after EDM is dependant on the process parameters. Electropolishing

can lower the surface roughness of a part, but the time required to achieve the desired surface roughness is dependant on the starting roughness [Pohl *et al.* 2004, Theisen *et al.* 2004]. Electrolyte temperature can also play an important role in the material removal rate of the parts surface [Fushimi *et al.* 2006, Miao *et al.* 2006]. Depending on the material being electropolished different electrolyte compositions are necessary to achieve the best results. For NiTi, it has been shown that methanolic sulfuric acid shows some of the best results [Fushimi *et al.* 2006, Nishiura *et al.* 2007].

1.6 Dynamic Mechanical Analysis

Dynamic mechanical analysis/analyzer (DMA) can measure rheological conditions under both dynamic and static conditions. DMA can measure the modulus, compliance and damping, as a function of temperature, time, frequency, stress, atmosphere, or a combination of these parameters [Perkin Elmer]. Shape memory alloys have been tested in a DMA to determine transformation regions and damping capacity, but a DMA is not commonly utilized to characterize the actuator-type properties of the alloy; quasi-static stress strain or constrained recovery. Roy *et al.* showed that DMA is also a viable tool for assessing such properties by testing commercially available, trained NiTi wires of diameter 0.38 mm [Roy *et al.* 2008]. This work will further this development by testing novel HTSMA wires with diameters ranging from 0.10 mm – 0.15mm for their actuator-type, thermo-mechanical properties.

CHAPTER TWO: LITERATURE REVIEW

Nickel-titanium alloys are the most common shape memory alloys on the market. They are used in a wide variety of applications due to both their shape memory and superelastic properties. The operational temperature limit for these alloys cannot exceed 100°C in most circumstances; therefore, ternary elemental additions have been experimented with to increase these operational temperature limits. The effects of palladium and platinum addition to NiTi will be presented further in this chapter, along with potential applications of these alloys to turbomachinery.

2.1 Phase Transformations in NiTi Alloys

NiTi exhibits a phase transition between its high-temperature phase, (B2) austenite, to its low-temperature phase, (B19') martensite, and back again. The B2 lattice is of BCC structure and the B19' lattice is of monoclinic structure. There is also the possibility of an R-phase forming during the forward transformation when cooling from B2 → B19' (Fig. 2.1). The R-phase has a trigonal structure which causes little lattice distortion when formed from the B2 phase (B2 → R); otherwise, larger lattice distortions are noticed when going directly from B2 → B19' or R → B19' [Kim *et al.* 2004].

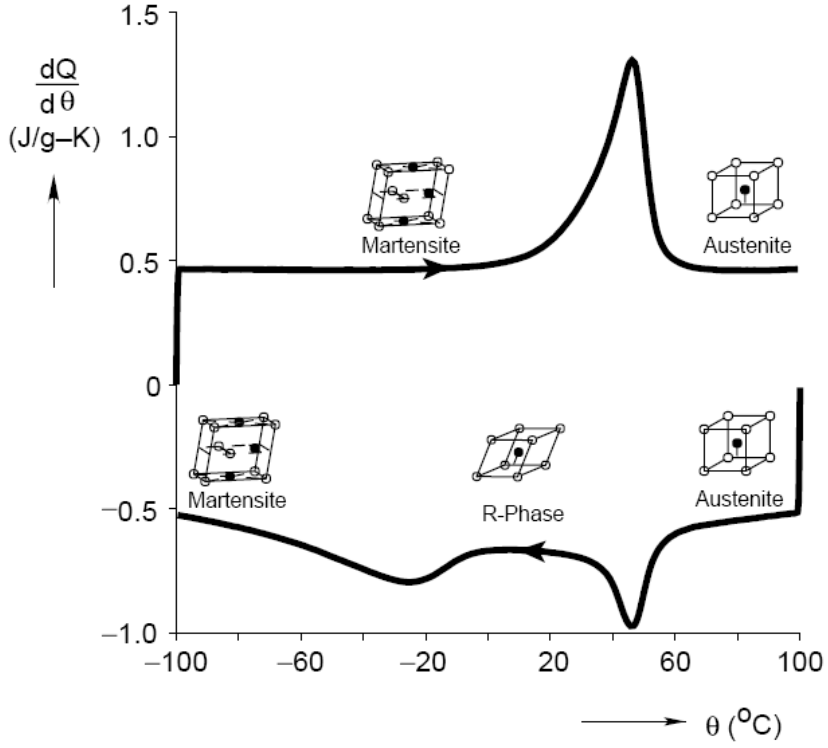

Figure 2.1: Forward and reverse transformation of NiTi showing intermediate R-phase [Elliott *et al.* 2002]

2.2 Effect of Thermo-mechanical Treatment in NiTi Alloys

There are many ways to control the hysteresis, transformation temperatures and yield strength of NiTi alloys. Cold-working NiTi induces dislocations in the material, which greatly strengthens the alloy, but these dislocations also prevent detwinning when strained in the martensitic phase, causing slip to occur prematurely. By subsequently annealing NiTi after cold-working the SME is reintroduced, but the yield strength decreases. Overall, the process of cold-

working and annealing increases the yield strength of the material from what it was before any thermo-mechanical processing.

Annealing can affect the transformation temperatures in NiTi. Annealing at increasing temperatures from 300°C can increase the transformation temperatures, but at a certain higher temperature the trend can reverse (Fig. 2.2). Therefore, optimizing the annealing temperature and time for a certain alloy can prove advantageous, and give the user more control over the properties. By annealing at certain temperatures below the recrystallization temperature an R-phase can be induced in the alloy.

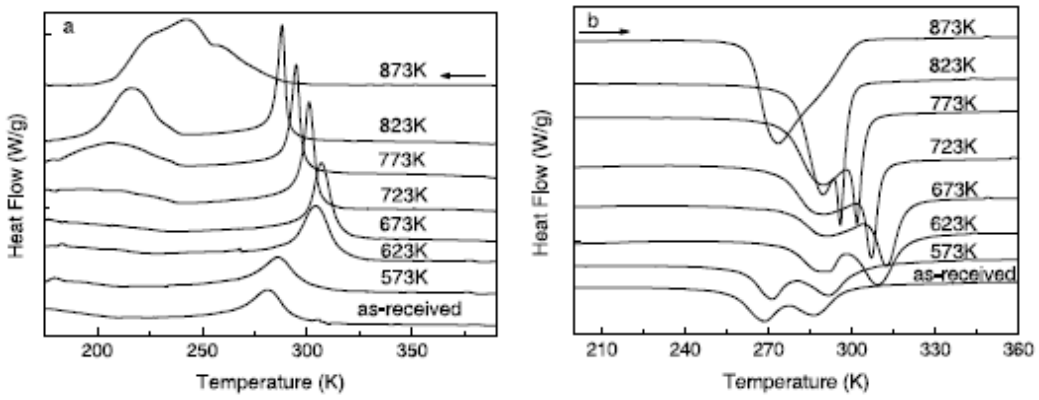

Figure 2.2: DSC curves for a Ti-50.85 at%Ni as a function of annealing temperature [Huang and Liu 2001]

Thermal cycling an alloy can also induce a two-way effect, otherwise known as "training," which can thermo-mechanically stabilize the material after a certain amount of thermal cycles under an applied stress (Fig. 2.3).

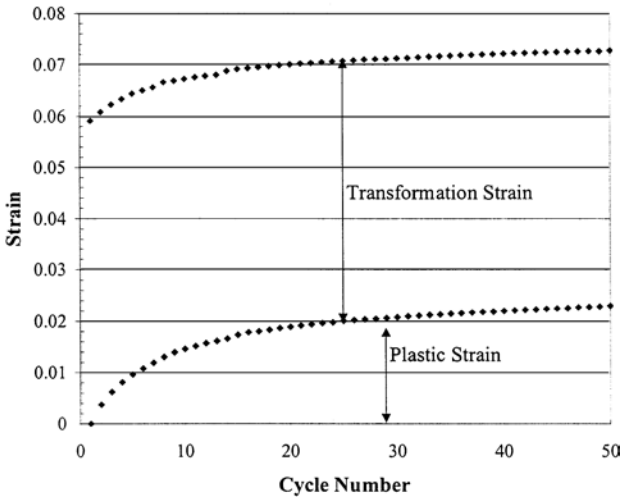

Figure 2.3: Effect of thermal cycling under an applied stress of 300 MPa for a given NiTi alloy that had been 20% cold-worked and annealed at 400°C for 15 min. [Miller and Lagoudas 2001]

Another similar method has been established and used for training of NiTiPd-based HTSMA tension samples by NASA Glenn Research Center [Bigelow 2008]. The samples are thermally cycled twice under no-load to relieve any stresses that might still be in the sample from fabrication, and then thermally cycled twice at 172 MPa to evaluate the effect of thermal cycling at no-load. After which, the sample was thermally cycled 10 times at 345 MPa, then cycled 10 more times back at 172 MPa to see if the high-stress cycling affected the stability of the alloy at lower stresses. The results of which can be seen in Figure 2.4. After plastically deforming the material at 345 MPa during thermal cycling the sample was able to undergo no further residual plasticity when thermally cycled at 172 MPa. Although, if the alloy was overheated during operation after training it would lose all of the training it had undergone, and go back to gaining significant residual plasticity after cycling.

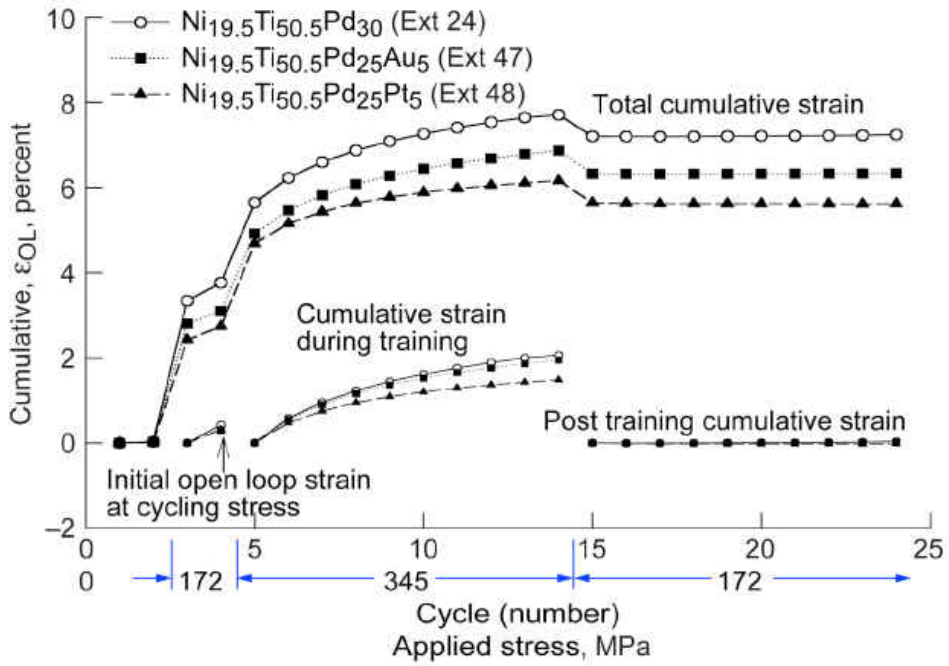

Figure 2.4: Effect of "training" on ternary and quaternary High-temperature NiTi-based alloys [Bigelow 2008]

The controlled stress or strain on a trained NiTi sample also significantly affects the fatigue behavior of the alloy. By actuating at lower stresses or strains the alloy has longer cycle life (Table 2.1).

Table 2.1: Fatigue of NiTi [Stöckel 1992]

# Cycles	Max. Strain	Max. Stress
1	8%	500 MPa
100	4%	275 MPa
10000	2%	140 MPa
100000+	1%	70 MPa

2.3 Physical Properties of NiTi Alloys

NiTi shows similar physical properties to that of nickel, one of its base elements, but does show differences between its two different phases; martensite and austenite. Table 2.2 shows many of the important physical properties of NiTi that are of value when designing a NiTi-based actuator.

Table 2.2: Physical Properties of NiTi [Dynalloy]

Density		6.45 g/cc
Specific Heat		837 J/(kg·K)
Melting Point		1250°C
Thermal Conductivity		0.21 W/(cm·°C)
Thermal Expansion Coefficient	Martensite	6.6×10^{-6}/°C
	Austenite	11×10^{-6}/°C
Electrical Resistivity	Martensite	7.0×10^{-7} Ω·m
	Austenite	8.5×10^{-7} Ω·m

2.4 Mechanical Properties of NiTi Alloys

Thermo-mechanical processing of NiTi can change some of the mechanical properties; i.e., yield strength and elongation at break. Repeatability of processing is also a factor in the mechanical properties, as all manufacturers of NiTi publish ranges of certain properties on their

technical data sheets, even for the same composition and processing parameters. Table 2.3 shows representative mechanical properties of NiTi.

Table 2.3: Mechanical Properties of NiTi [Mavroidis 2002]

Young's Modulus	Martensite	Approx. 28-41 Gpa
	Austenite	Approx. 83 GPa
Yield Strength	Martensite	70 -140 Mpa (onset of detwinning)
	Austenite	195 - 690 MPa
Ultimate Tensile Strength		895 MPa
Poisson's Ratio		0.33

2.5 Fabrication Techniques for NiTi Alloys

NiTi requires strict control when melting and forming the alloy. Titanium is highly reactive in air, and so requires vacuum conditions during melting and solidification. The weight% of nickel in the alloy has to be closely controlled due to the fact that a 1 weight% change in nickel for the melt can result in a transformation temperature shift of about 100°C. NiTi is typically rolled or extruded at 800°C temperatures to optimize the mechanical properties [Wu 2001]. The alloys are subsequently cold-worked and annealed to further strengthen the alloy and optimize it for a given application. Once an alloy has the desired mechanical

properties it can be formed to many different shapes. In order to have a prescribed austenite phase shape, the part can be mechanically deformed into a holding fixture and shape-set. Typically, shape-setting is done for NiTi between 350-550°C for 5-60 min., depending on the composition and size of the part.

Cold-drawing NiTi is a common practice in industry, but requires delicate procedures. By passing the material through several dies to achieve the desired final dimensions, frequent inter-pass annealing steps are performed. Inter-pass annealing refers to multiple anneals of the wire between 600-800°C after every few reduction steps, due to the rapid work-hardening of the NiTi wire [Wu 2001].

2.6 Scaling Effects in NiTi

Little research is available concerned on the scaling effects in NiTi-based alloys. Typically, bulk properties are tested for an alloy and are considered the standards for any sample that is extracted from it; e.g., wires or strips. McCormick *et al* addressed this issue by testing different size bulk tensile specimens and tensile coupons that had been extracted by EDM from those same bulk specimens. The focus of their work was cyclic loading effects on pseudoelastic NiTi, but it yielded some interesting qualitative explanations. McCormick *et al* describe that the coupons that had been extracted from different locations in the bulk specimen showed inconsistent responses from that of the bulk specimens tested, and that each coupon was considered heterogeneous and not representative of the bulk [McCormick *et al.* 2007]. They also

deduced that precipitates have a larger influence on the strength of hot-rolled NiTi than grain size, and that Lüders-like behavior is prevalent in all the coupons, but not the full-scale tensile specimens [McCormick *et al.* 2007].

2.7 NiTiPd Alloys

There are several ternary elemental additions that have been added to NiTi to increase the transformation temperatures; such as hafnium, zirconium, platinum, palladium and gold (Fig. 2.5). These alloys typically have lower transformation temperatures than binary NiTi for the first 10% ternary addition, but then increase linearly to exceed binary NiTi [Lindquist 1988, Noebe *et al.* 2006]. Though the transformation temperatures have been raised using ternary alloying, not much thermo-mechanical testing has been done to evaluate the prospect of using the SME of these alloys in an actuator application. Most of the ongoing research being done to assess the actuator-type performance of HTSMA is in the NiTiPd and NiTiPt systems [Lin *et al.* 2008, Bigelow 2008].

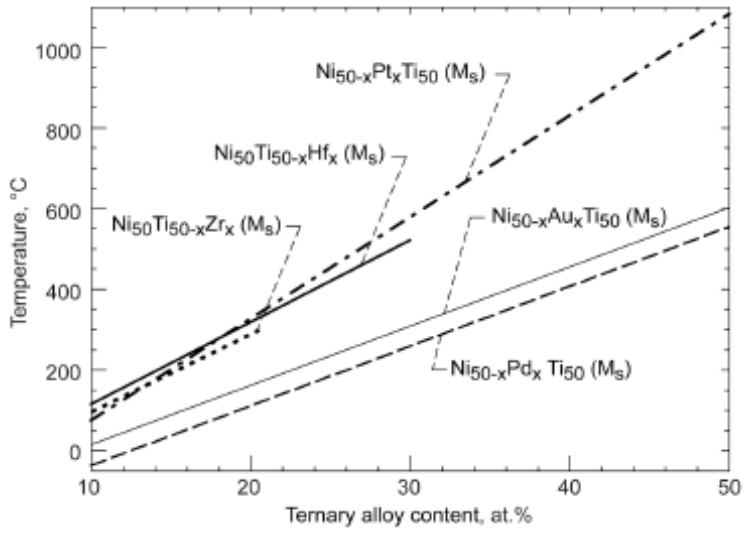

Figure 2.5: Effect of ternary alloying on the transformation temperatures of NiTiX (X=Hf, Zr, Pt, Pd, Au) [Noebe *et al.* 2006]

High-temperature NiTiPd does not have the same martensitic phase structure as binary NiTi. For compositions of NiTiPd with <10 at% Pd the structure is monoclinic B19' like NiTi, but at over 10 at% Pd the martensite structure becomes orthorhombic B19 [Lindquist 1988, Otsuka and Wayman 1998] (Fig. 2.6).

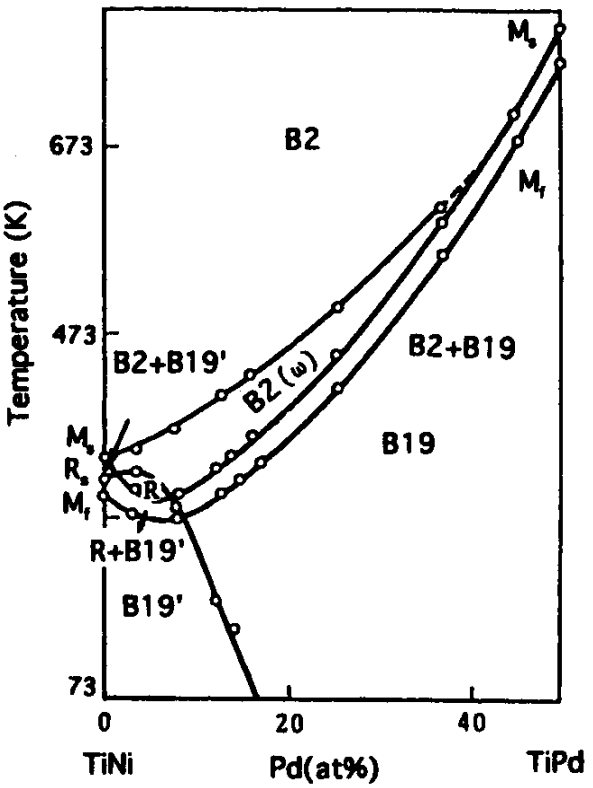

Figure 2.6: Phase Transformation path for various NiTiPd compositions
[Otsuka and Wayman 1998]

NiTiPd also exhibits superelasticity in certain temperature ranges, but does not follow the same stress-strain trend as NiTi (Fig. 2.7). The stress-induced B2 → B19 transformation (II) occurs very suddenly due to the reduced number of martensite variants for its orthorhombic martensitic structure, as compared to B19', and reorients quickly to begin elastic deformation of the detwinned orthorhombic structure (III) [Wu and Tian 2003].

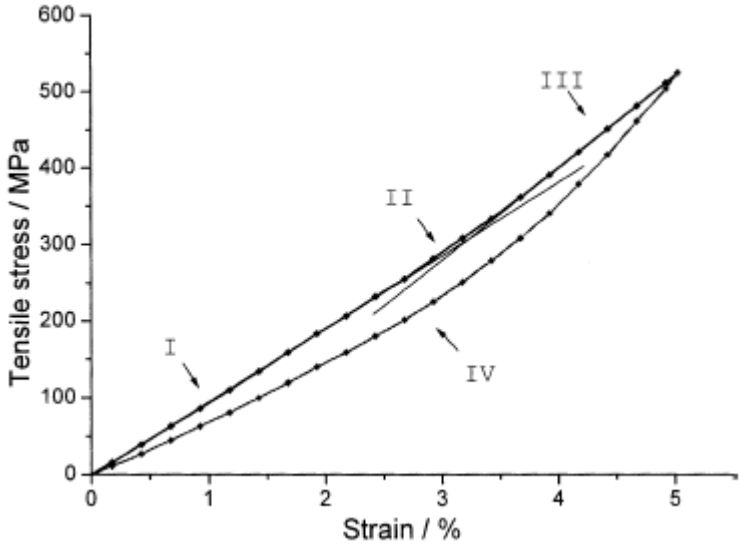

Figure 2.7: Stress-strain response of superelastic $Ti_{51}Pd_{30}Ni_{19}$ [Wu and Tian 2003]

Shimizu *et al.* have established ageing parameters to raise the critical stress for slip, thereby strengthening the alloy for actuator-type applications [Shimizu *et al.* 1998]. Tian *et al.* have also been able to improve the oxidation resistance of NiTiPd by doping it with 1 wt% Cerium, which impedes the outward diffusion of Ti to the surface [Tian *et al.* 2003].

2.8 Prospective Application of SMAs to Turbomachinery

Shape memory alloys have been used for many aerospace and aeronautical applications, but not in any roles requiring high transformation temperatures (>100°C). They have been used to extend solar panels on satellites [Carpenter *et al.* 1995], change the exhaust geometry on jet

engines [Calkins *et al*. 2006], and used to morph wing geometry [Lizotte and Allen 2005], but have not been used to control flow within a turbine. Both ground-based turbines and jet engines have internal temperatures during operation that far exceed the operational limit of any commercially available shape memory alloy. There are many other factors besides high temperatures that can influence the operation of an SMA material inside a turbine; i.e. high pressures, vibrations, and creep effects from rotating components (Fig. 2.8).

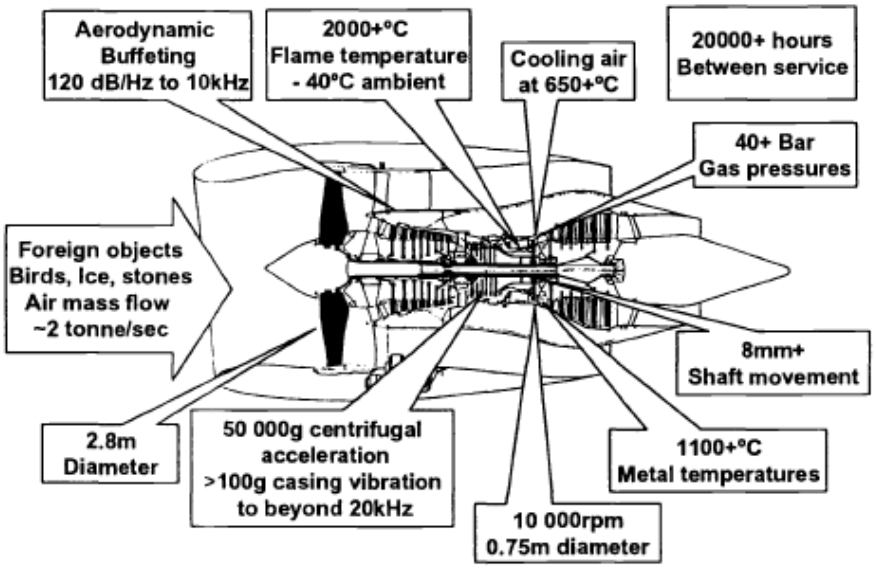

Figure 2.8: Schematic of jet engine and typical operating conditions [Webster 2003]

There are many potential applications for SMAs in turbines, but the development of viable high-temperature SMAs has not yet been established to survive in these environments (Fig. 2.9). Though an SMA-controlled jet engine inlet has been tested by DARPA, and Boeing has developed a variable area fan nozzle prototype and a flight-tested variable geometry chevron

array for use on the jet engine exhaust to reduce noise at takeoff/landing [Sander *et al.* 2004, Mabe *et al.* 2008, Calkins *et al.* 2006]. However, neither of these applications requires high-temperature survivability, and actuates using active heating at temperatures at or below 100°C. NASA has investigated using high-temperature shape memory alloys for active clearance control inside turbo-machines in the compressor and turbine sections to reduce the running clearance and increase efficiency [Schetky and Steinetz 1998, Lattime *et al.* 2003, DeCastro *et al.* 2005]. However, there is much more research that is needed before high-temperature SMAs can be certified for commercial turbomachinery applications.

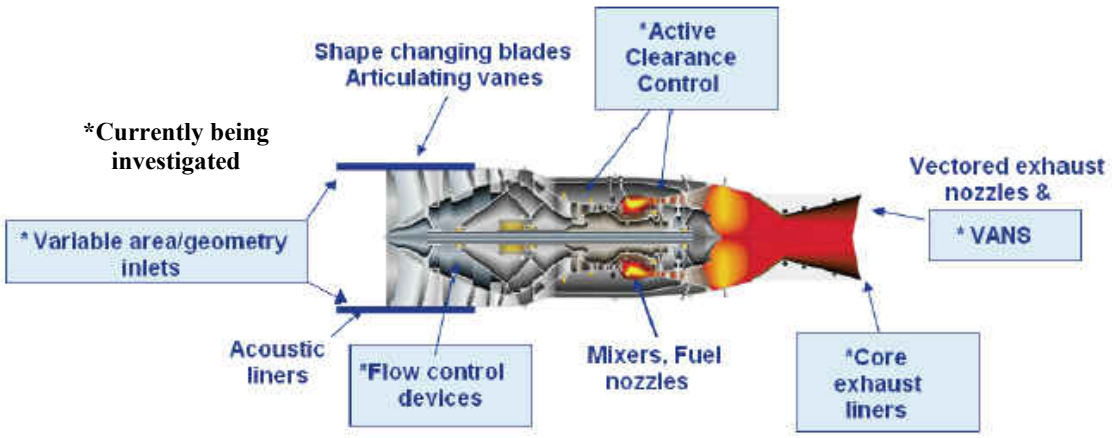

Figure 2.9: Potential Applications for SMA in Turbomachinery [Bigelow 2006]

Shape memory alloys have higher work output to weight ratios than any of the common actuator systems used in industry (Fig. 2.10). The shape memory effect can be harnessed by coupling an SMA spring with a biasing element (e.g., steel spring), and the desired actuation

displacement can be tuned by using bias springs with different spring constants (Fig. 2.11). SMAs can also be used in bending by biasing it with another plate of a different material.

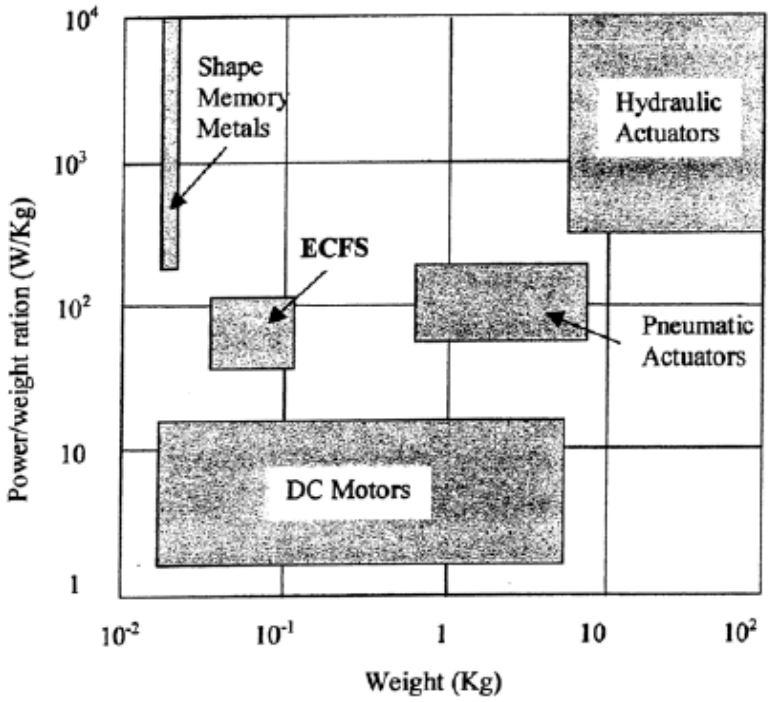

Figure 2.10: Power/weight ratios for common actuator systems [Mavroidis 2002]

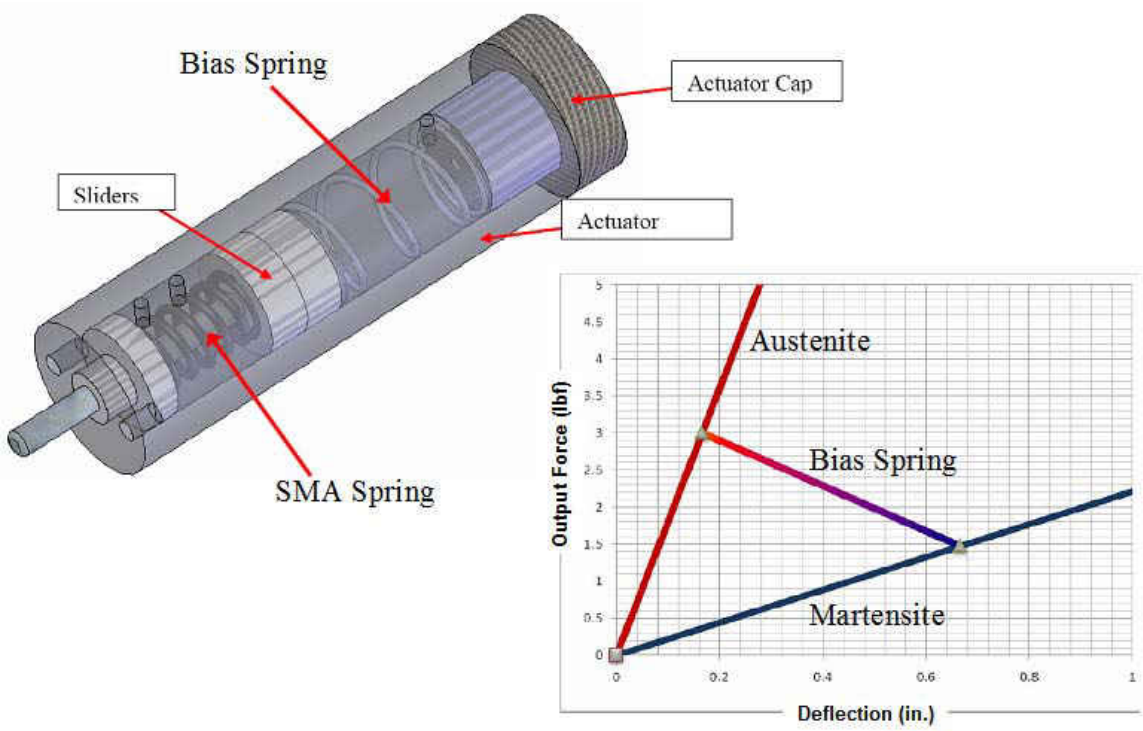

Figure 2.11: Linear SMA actuator design concept [Lam *et al*. 2007]

There are many patent filings that detail the use of actuators in turbines for the purposes of either active/passive clearance control, or variable geometry exhaust systems. None of these have come to fruition by the use of shape memory alloys as the main component for the actuators described.

For active clearance control, D. H. Evans has proposed using a feedback control system, coupled with a fluid reservoir, to control the position of a shroud segment over rotating turbine blades [Evans 1993]. By replacing the feedback control system with a shape memory alloy, coupled with a bias spring, the same function can be achieved using less weight and simpler

operation (Fig. 2.12). Similarly, a unison ring can be positioned circumferentially around the turbine blade shroud, and can rotate by active mechanical means using an external actuation system to radially position the shroud segments towards and away from the blade tips [Tseng and Hauser 1991]. The same function can be accomplished by using an active/passive shape memory alloy circumferential actuator system (Fig. 2.13). A passive system proposed by I. S. Diakunchak suggests using a bi-metal approach for clearance control [Diakunchak 2005]. This means forming a layered structure with two opposing materials, where each one has its own coefficient of thermal expansion that can passively alter position of the structure tips to come closer or further from the turbine blades during heating and cooling. By using the same approach, a shape memory alloy and a biasing material (e.g., Inconel 718) can be sandwiched together into a composite to form a bi-metal actuator (Fig. 2.14).

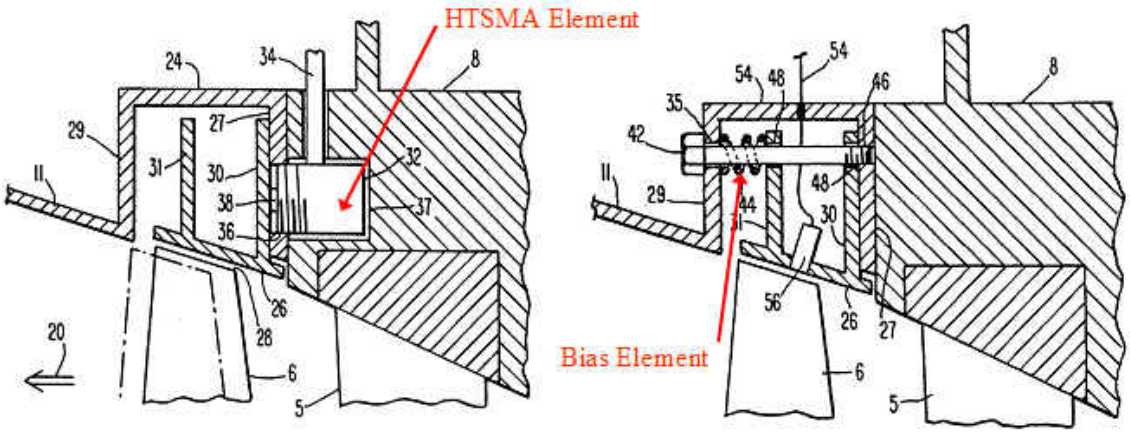

Figure 2.12: Designs proposed in patent detailing active clearance control, with suggested modifications for incorporation of shape memory alloys shown in red [Evans 1993]

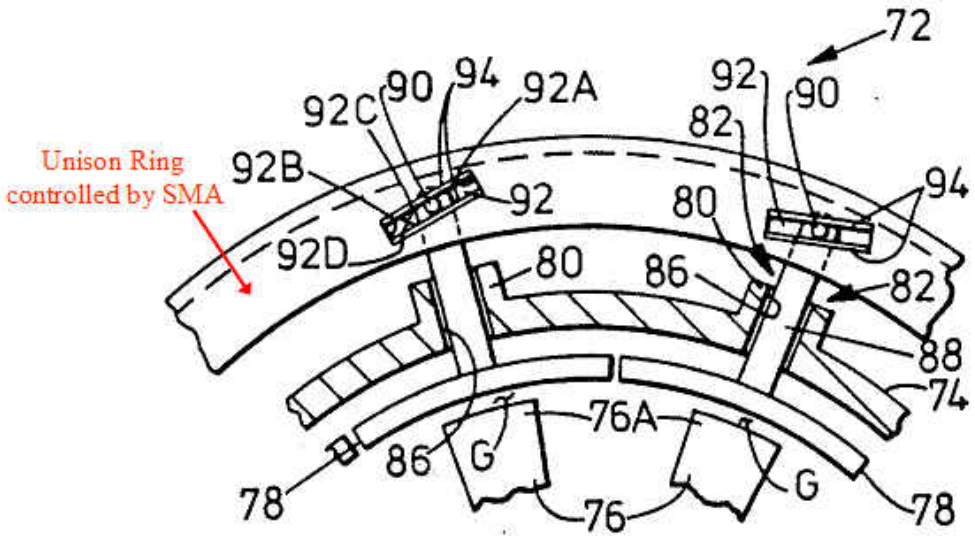

Figure 2.13: Design proposed in patent detailing active clearance control, with suggested modifications for incorporation of shape memory alloys shown in red [Tseng and Hauser 1991]

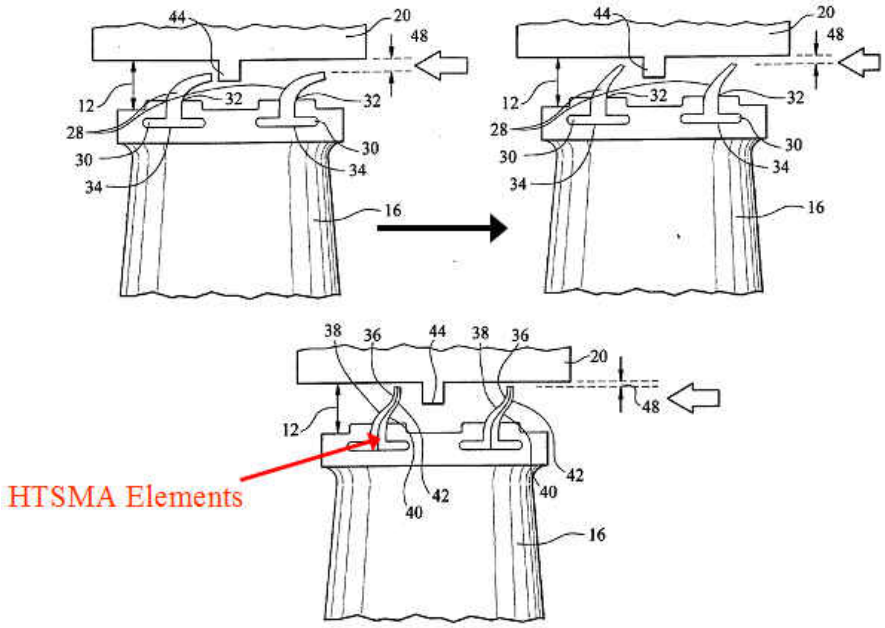

Figure 2.14: Design proposed in patent detailing passive clearance control, with suggested modifications for incorporation of shape memory alloys shown in red [Diakunchak 2005]

For variable geometry exhaust systems, V. L. James has proposed a mechanism which controls the expansion ratio of a turbine exhaust by using circumferentially positioned linear actuators to change the area of the throat [James 1980]; these linear actuators can be replaced with an SMA linear actuator, like the one seen in Figure 2.11 (Fig. 2.15). Also, two overlapping circumferential sleeves can be free to move backwards and forwards about the radial axis to alter the expansion ratio by repositioning the exhaust throat along the diffuser cone by using linear actuators [Renggli 2007]. These linear actuators can also be replaced with an SMA linear actuator (Fig. 2.16). A similar concept has circumferentially positioned linear actuators which control a mechanism to expand the exhaust area, while keeping the throat area and position constant [Elorriaga *et al*. 2000]; these linear actuators can also be SMA-based (Fig. 2.17).

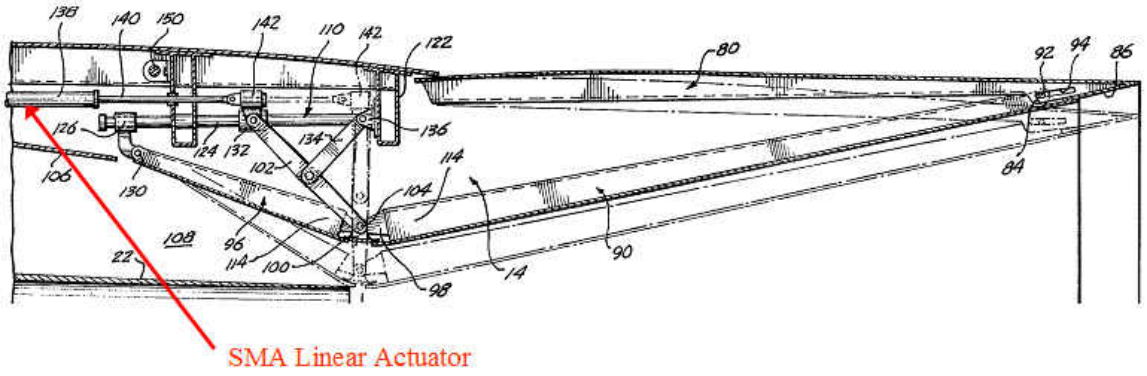

Figure 2.15: Design proposed in patent detailing variable geometry exhaust, with suggested modifications for incorporation of shape memory alloys shown in red [James 1980]

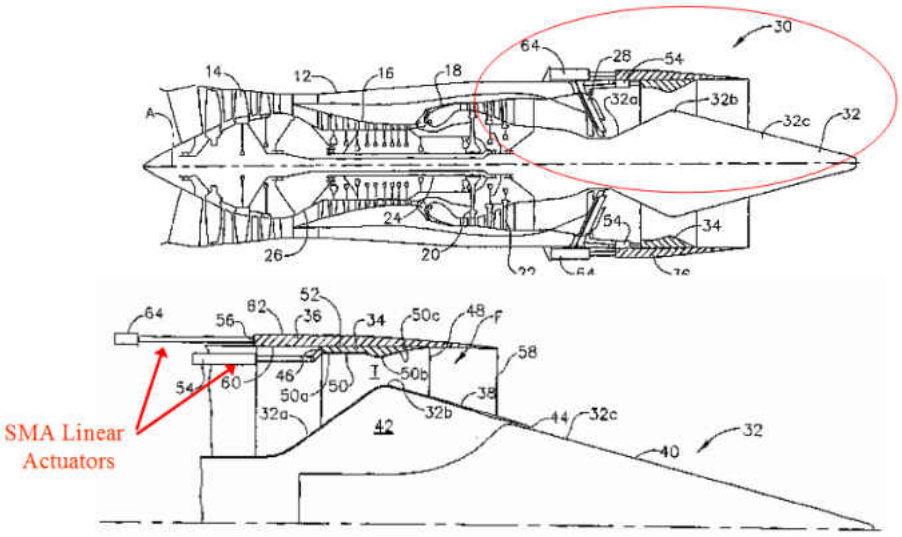

Figure 2.16: Design proposed in patent detailing variable geometry exhaust, with suggested modifications for incorporation of shape memory alloys shown in red [Elorriaga *et al*. 2000]

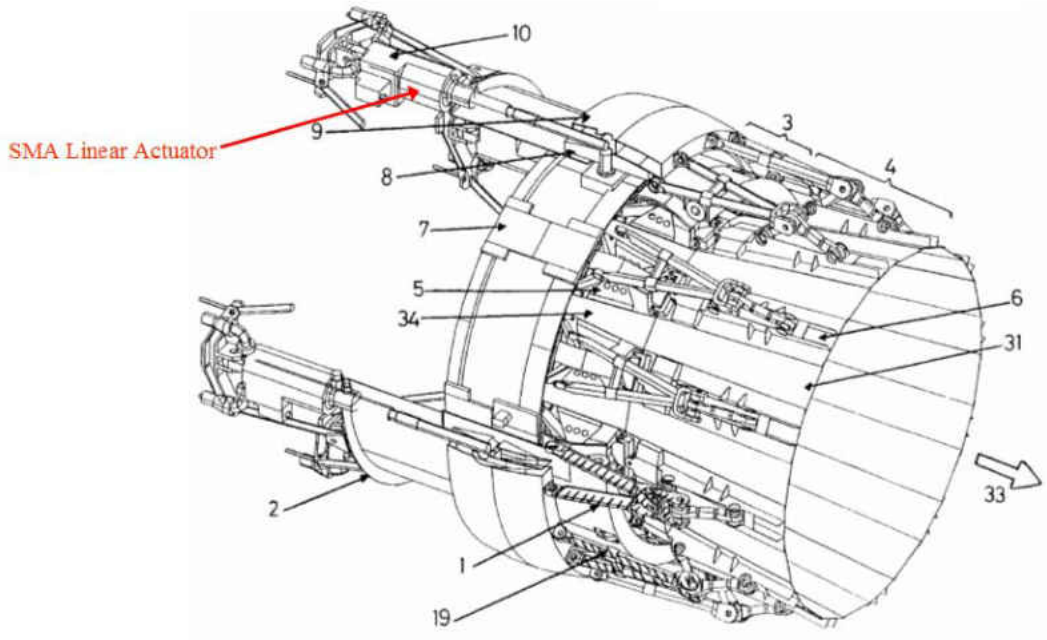

Figure 2.17: Design proposed in patent detailing variable geometry exhaust, with suggested modifications for incorporation of shape memory alloys shown in red [Renggli 2007]

CHAPTER THREE: FABRICATION OF MICRON-SCALE NiTiPd WIRES

The NiTiPd wires tested in this work were obtained by using a combination of wire electrical-discharge machining (EDM) and electropolishing. Rectangular cross-section wires with dimensions of 60 mm long and 0.2 mm sides were extracted from $Ni_{29.5}Ti_{50.5}Pd_{20}$ bulk tension specimens using wire-EDM. The cross-section dimensions were further reduced by electropolishing to uniformly remove material from the surface, as well as remove the heat-affected zone (HAZ) caused by EDM.

3.1 Bulk Sample Preparation

The as-received $Ni_{29.5}Ti_{50.5}Pd_{20}$ bulk tension sample used for extracting the wires by wire-EDM for this work was prepared using the procedure previously outlined [Bigelow 2006].

3.2 Electrical-Discharge Machining

To relieve any possible residual stresses from the machining operation of the bulk specimens, all of the samples were wrapped in titanium foil and annealed at 400°C for one hour and furnace cooled [Bigelow 2006]. Rectangular cross-section wire samples with cross-section dimensions of 210 ±7 μm x 200 ±7 μm and length 60 mm were obtained from one of the "virgin" bulk specimens by wire-EDM. An Elox-Model P wire-EDM with a Fanuc-6 controller was used

for the process. The controller was set to an operating voltage of 50V, a working current of 2.5A and used a 100 μm diameter brass wire as the electrode at room temperature, and deionized water as the dielectric fluid.

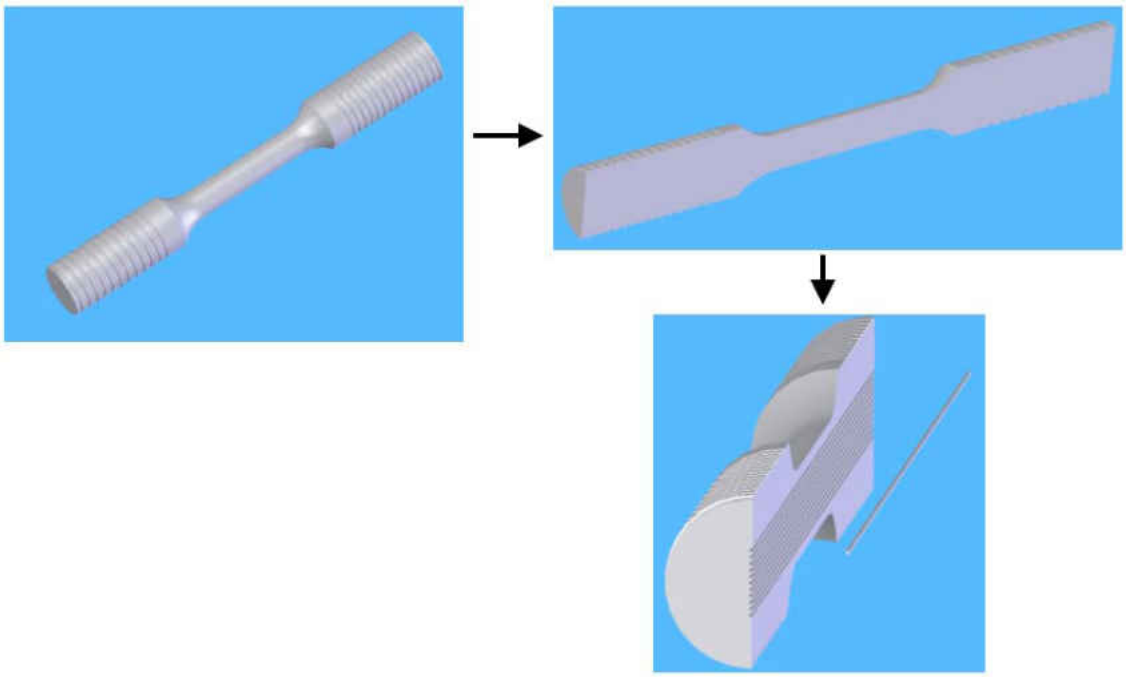

Figure 3.1: Sequence for extraction of wires from bulk samples by wire-EDM

3.3 Electropolishing

Selection of the proper electrolyte and operating voltage of the equipment was essential to providing both good material removal rates and surface finish. Two sets of wires produced by EDM were electropolished in a 3 mol·dm^{-3} methanolic sulfuric acid electrolyte [Fushimi *et al.*

2006] held at 24°C in an ESMA model E1085-1S electropolisher. One set had cross-sectional edge lengths which averaged 150 ±2 μm x 130 ±2 μm and the other set had cross-sectional edge lengths which averaged 110 ±2 μm x 100 ±2 μm. As a beneficial consequence of varying the electropolishing parameters to optimize the removal rate and uniformity of the wires, a pattern was established that could also control the relative curvature of the corners of each wire cross-section. It has been suggested that lower electrolyte temperatures provide a better surface finish [Fushimi *et al.* 2006]; however, due to the slow material removal rates that accompany it electropolishing was performed at room temperature. The 60 mm long wires that were extracted by wire-EDM were first cut into two 30 mm pieces before electropolishing.

3.3.1 Preparation of Electrolyte

To prepare the electrolyte 96% pure sulfuric acid and 99.8% pure methanol was used. By creating an electrolytic solution that is 16 volume percent sulfuric acid and 84 volume percent methanol, the desired 3 $mol \cdot dm^{-3}$ methanolic sulfuric acid was formed. The methanol was first measured out to be 84% of the volume necessary to fill the electropolisher tank to the desired fluid level. The remaining 16% volume of sulfuric acid was then measured out and mixed very slowly into the methanol. The reaction of sulfuric acid with methanol is a exothermic reaction that can easily become dangerous if precaution is not met. Care was taken to add sulfuric acid to methanol, and not the other way around. The following is the procedure to be followed to mix the electrolyte.

1. Make sure the container has a large opening (about the same diameter of the container) to allow for more gas escape.
2. Always mix under ventilation and while wearing the appropriate safety gear prescribed in the MSDS for sulfuric acid [Sulfuric Acid MSDS].
3. Pour the sulfuric acid very slowly into the methanol.
    - Stop immediately if the bubbles begin to burst outwards from the surface.
    - Small additions of sulfuric acid should be done at short intervals to allow for the reaction to settle down before proceeding.
    - The exothermic reaction of methanol and sulfuric acid produces a combination of dimethyl sulfate and water.
4. Once the final solution is prepared and mixed allow for the full reaction to complete and for the electrolyte to cool back to room temperature, as it will get hotter during mixing.

3.3.2 Electropolishing Procedure

An ESMA, Inc. brand electropolisher was used to polish the wires used in this work. The details of the model used can be seen in Table 3.1. Electropolishing was done in a ventilated area. The following procedure was used for setup and operation of the electropolisher.

1. Place tank into the recess at the top of the electropolisher so the post on the base plate of the polisher is aligned with the cylindrical recess in the tank.

2. Place the cooling coil rack into the tank so the open ends are facing to the right and out of the tank, and the rack is pushed all the way into the tank so it is resting on the bottom; may need to push cathode sheet against wall of tank to facilitate room for the cooling coils.
3. Hook up tubing to the input and output of the tank's cooling coil so that the cooling fluid is flowing from a source into one end of the cooling coil rack, through the output and draining into another location.
4. Ground the tank to the electropolisher base using a wing-nut and place the sample holding fixture setup onto the edge of the tank in the position shown in Figure 3.2.
    - See Figure 3.3 for configuration of the holding fixture setup.
5. With the titanium holding clip fixed into the sample holding fixture, pour the electrolyte into the tank until the fluid level is at the position seen in Figure 3.3.
6. Remove the titanium holding clip and rinse in a large water bath, then dry with a paper towel.

Table 3.1: Details of ESMA, Inc. brand electropolisher used

Model #	Unit Dimensions	Tank Capacity	Current Capacity
E1085-1S	17" x 11" x 10"	0.5 Gallons	12 A

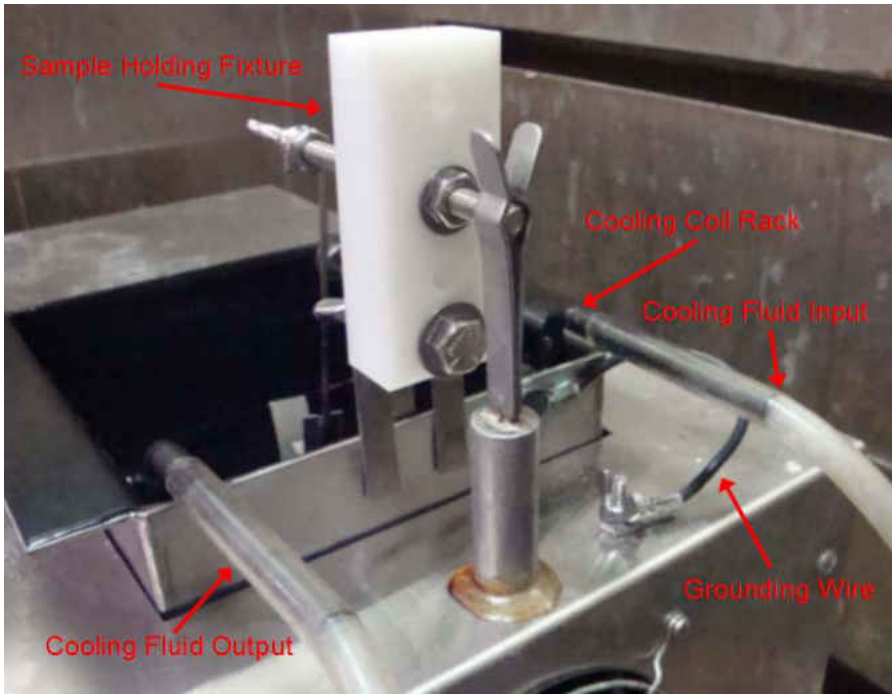

Figure 3.2: Positioning of sample holding fixture and grounding wire for electropolisher

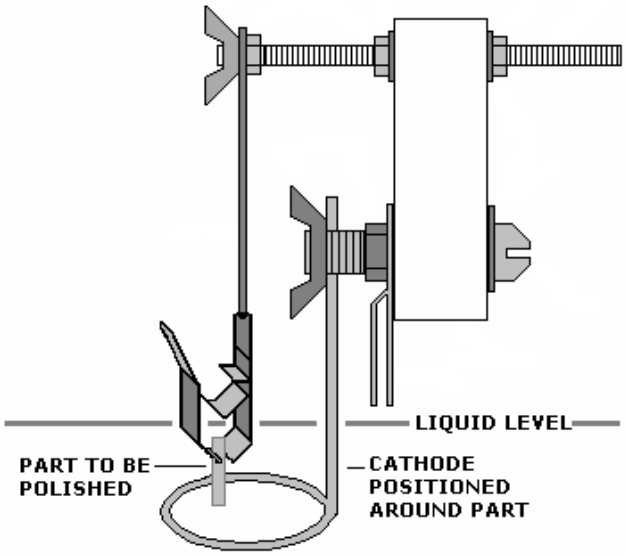

Figure 3.3: Configuration of sample holding fixture [ESMA, Inc.]

7. Plug the electropolisher into a standard wall outlet, turn on the system using the switch on the front face of the electropolisher, and set the fluid temperature using the input panel on the face of the electropolisher (Fig. 3.4).
8. Wait for the temperature to stabilize, then fix the sample into the titanium holding clip and fix the titanium holding clip back onto the sample holding fixture with the sample being completely submerged in the electrolyte and centered in the cathode ring.
9. Set the timer for the time you want to polish the sample.
10. When you are ready, hit the "Start" button, and adjust the voltage until the desired reading is met on the gauge.
11. After the timer goes off turn the voltage to zero and remove the titanium holding clip with the sample fixed in the clip.
12. After each trial it is important to neutralize the sample and clip in water, deoxidize the clip in ESMA, Inc. brand Nitric Deox®, rinse it in water to neutralize it and then dry it with a paper towel (Fig. 3.5).
13. Fix the sample into the clip again, this time with it being held at the opposite end that it was in the previous trial, and repeat steps 9-13.
14. When the desired material removal has occurred and the sample is polished, you can stop the cooling fluid flow to the cooling coil and turn off the electropolisher.
15. Remove the sample holding fixture from the tank and wash off all parts which came in contact with the electrolyte.

16. Remove the input hose from its source and drain all fluid from the hose through the cooling coil and into the drainage container.
17. Remove the cooling rack from the electrolyte and allow the electrolyte to drip back into the tank before rinsing it with water to neutralize the acid.
18. Remove the ground wire from the base of the electropolisher, remove the tank and drain the electrolyte back into its sealable holding container.
19. Rinse out the tank to neutralize the acid and dry it with a paper towel, then place all items back with the electropolisher.

Figure 3.4: Gauges and displays on front panel of electropolisher

Figure 3.5: Deoxidization of titanium holding clip and placement of sample back in the clip

3.3.3 Electropolishing Procedure

The electropolisher was set up and operated in the way described in Section 3.3.2. For the material removal and polishing of the NiTiPd wires to be tested for their monotonic tensile behavior, the first and second trial was done at 8 V for 1 minute each. After which the wires were rinsed in water and wiped using a propanol-soaked Kimwipe® to remove the remelt layer from the surface of the wires that formed during the EDM process. This alone will make the surface of the wires shiny, but further material removal must be done. The next trials were all done for 1 minute each, at 10 V. These trials were repeated until the desired dimensions were achieved. Each trial done in this way reduced the diameter of the wires by 10 μm. For instance, to go from a 210 μm x 200 μm wire cross-section to a 110 μm x 100 μm cross-section, it would take 10 trials of (10 V for 1 minute).

For the wires that were tested in constrained recovery conditions a different process was used to control curvature at the corners, while all having the same cross-section dimensions. They were initially polished at 8 V for 1 minute for 2 cycles to remove the remelt, and then were polished at different voltages to create individualized results. For the wire with a corner radius of 6 ±4 μm it was polished at 6 V for 30 s per trial. For the wire with 25 ±7 μm as the corner radius it was polished at 7 V for 30 s per trial. Lastly, for the wire with the corner radius of 37 ±5 μm it was polished at 8 V for 30 s per trial. The trials for each wire were repeated until the overall dimensions were at or slightly below 150 μm x 140 μm. This is not meant to be an exact procedure, but general guidelines for creating different shaped cross-section wires using an electropolisher.

CHAPTER FOUR: CHARACTERIZATION OF NiTiPd WIRES

Electrical-discharge Machining (EDM) can damage the surface of the samples machined in this way. Since the size of the wires being produced by this process were small (on the order of 100 μm) it was essential to know the depth of this damage, and to remove it so it does not influence the thermo-mechanical properties of the shape memory alloy wires. Scanning Electron Microscopy (SEM) was used to ensure the electropolished samples were polished uniformly and to determine the effect electropolishing had on the surface texture and composition of the wires. Transmission Electron Microscopy (TEM) was used to analyze the cross-sectional profile of the wires to determine if any Heat-affected Zone (HAZ) was still present in the material, and to establish if there were any deleterious side effects from electropolishing. The cross-sectional shape of the wires was determined using profile images taken using a Laser Scanning Confocal Microscope (LSCM) in confocal viewing mode, and then redrawn and cross-sectional area calculated using SolidWorks®.

4.1 Scanning Electron Microscopy

To assess the damage that had been incurred on the samples during the EDM process a JEOL 6400F Scanning Electron Microscope operating at 12 kV, with Energy Dispersive Spectroscopy (EDS) capabilities, was used to evaluate the surface structure that had formed on the samples following EDM. Surface roughness and composition was analyzed at various

locations on the wires, both post-EDM and post-electropolishing to establish the effect of EDM and the effect of electropolishing on the wires. Low-magnification images were also taken to verify that the wires were uniform along the length-wise dimension after wire-EDM, and if they remained uniform after electropolishing.

4.2 Transmission Electron Microscopy

An FEI Technai F30 TEM operating at 300 kV was used to determine the depth of the heat-affected zone, as well as profile any structural or compositional changes from the surface to the core of the sample. The TEM specimens were prepared using an FEI 200 Focused Ion Beam instrument (FIB) operating at 30 kV. After electropolishing, TEM specimens were prepared of the wire cross-section to determine if the HAZ had been completely removed from the sample, and if a purely martensitic structure was present at room temperature.

4.3 Measurement of Fabricated Wire Cross-sections

An Olympus brand LSCM was used to profile the NiTiPd wires. The wires were observed in optical mode and measured for their overall cross-section dimensions; i.e. width and height. Six measurements were taken along the length of each sample to measure the overall dimensions and the standard deviation. This entailed zooming into the wire at 480x zoom and taking 10 line measurements across the width of the wire for six equally spaced locations across

the length-wise dimension of the wires. The average of the 10 measurements for each location was calculated and recorded. The standard deviation for the wires' dimensions no higher than 2.2 μm. The average of the six measurements taken along the length-wise dimensions for each side of each wire was determined. Each wire surface was then observed in confocal viewing mode. Using the average determined width for the surface being viewed, a location was selected along the wire's length-wise dimension that represented that exact value. The wires were placed completely flat onto an opaque slide for imaging. The wires were then viewed at a magnification that fit the entire wire just within the boundaries of the software's image window. The instrument was then focused down to the surface of the slide and that point was selected as the bottom. Then, the instrument was focused up to the top most point on the surface of the wire and that point was selected as the top. 3-D profile images were then generated using a step image height of 0.5 μm (Fig. 4.1). This means that an image was taken on the bottom-most point designated in the previous step, the instrument then focused to a point 0.5μm up and took another image, and this process was repeated hundreds of times until the upper-most image was taken. The more in focus the surface was at a particular level, the higher the contrast was. By layering these images on top of each other the instrument's software was able to generate a 3-D image of the wire. These generated images were produced for two adjacent sides of each wire to get a generally accurate geometric shape.

The 3-D profiles were then viewed on a scaled 2-D coordinate system normal to the cross-section (Fig. 4.2). The instrument was not able to capture every point on the wire due to the reflective angle limitations of the incident beam. Hence measuring the width of the 2-D

representation and comparing it to the recorded value it was possible to verify that the outermost points of the wire were captured. The images were then converted into a system of coordinates; over 1,000 for each profile. The wire cross-sections were then redrawn and measured for their cross-sectional area using SolidWorks®. After mechanical testing of calibration wires and calculating the elastic modulus using the above method for cross-sectional area calculation, it was shown to be an accurate method for determination of wire cross-sectional area.

In addition, a wire was mounted in epoxy, mechanically polished and etched, and the surface analyzed using LSCM to determine the grain size for comparison to bulk samples analyzed in previous work [Bigelow 2006].

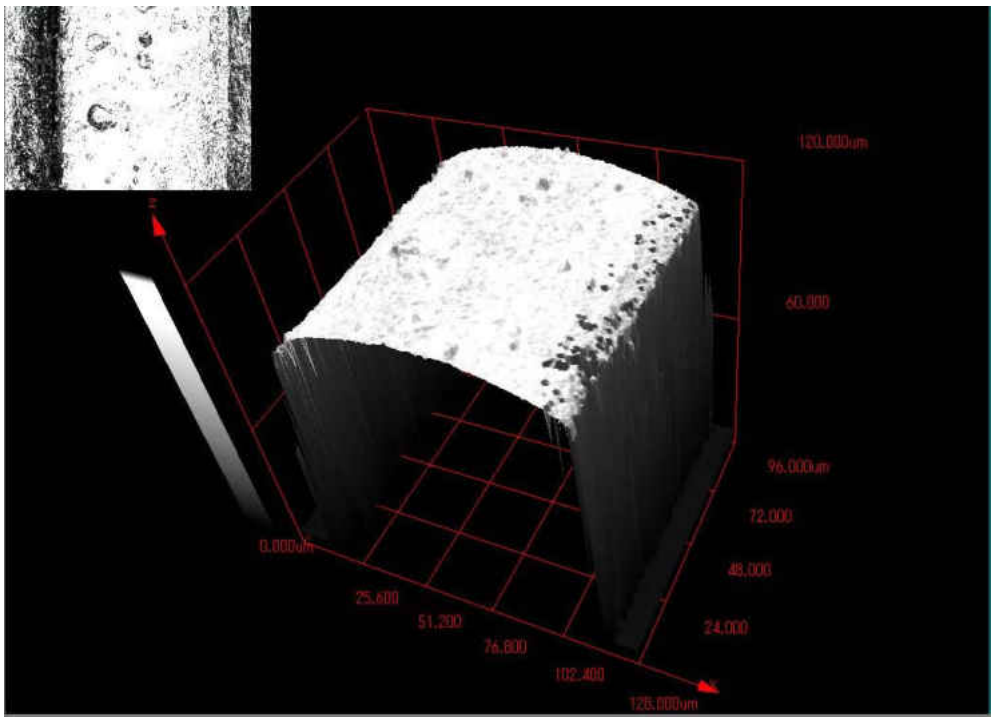

Figure 4.1: Example 3-D profile image using Laser Scanning Confocal Microscopy

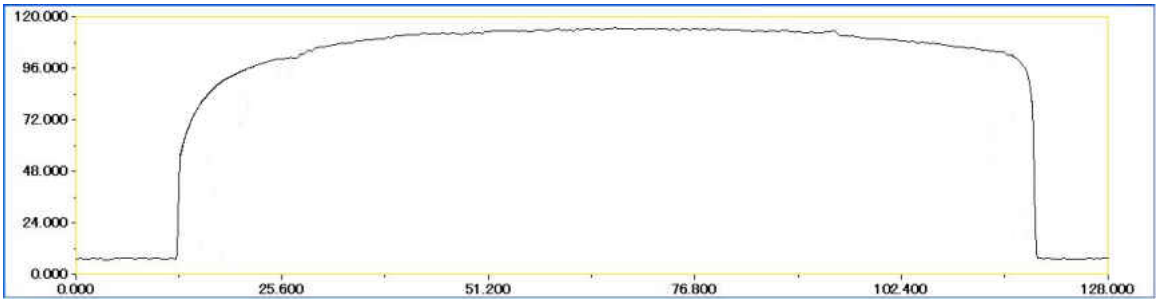

Figure 4.2: Example 2-D profile of cross-section after filtering out noise

4.4 Dynamic Mechanical Analysis

A dynamic mechanical analyzer (DMA) was used to determine the thermo-mechanical properties of the NiTiPd wires. A DMA "*supplies information about major transitions as well as secondary and tertiary transitions not readily identifiable by other methods*," [Menard 1999]. For this reason a DMA was considered suitable for testing such thin SMA wires. The following sections detail the components, operation and calibration of the DMA, as well as the thermo-mechanical testing that was performed on the NiTiPd wires in the DMA after full calibration, and in the process builds on work done by a previous author [Nandiraju 2006].

4.4.1 Equipment

The DMA setup consists of a cooling tank that, along with the cooling controller, helps control the temperature inside the test section, a cooling cylinder that cools the internal components of the DMA when operating at high temperatures, a computer-based software package which controls the system, and the DMA itself (Fig. 4.3).

Equipment List:

1. Perkin Elmer Diamond DMA
2. Computer – MUSE Software
3. Furnace Cooling Tank
4. Furnace Cooling Controller
5. DMA Cooling Cylinder

Figure 4.3: DMA Equipment

4.4.1.1 Perkin Elmer Diamond DMA

The Diamond DMA can measure the rheological behavior of a material under dynamic and static conditions, as a function of temperature, stress, time, frequency, or a combination of these parameters. The Diamond DMA uses Fourier transform to reduce signal noise, thereby being capable of detecting very weak transitions that may occur in the material during a particular test. The system utilizes a heater that encompasses the test section for controlled heating, an embedded LVDT which measures the probe displacement and a force generator to provide a static or oscillatory (dynamic) force. The specifications of the DMA are outlined in Table 4.1.

Table 4.1: DMA Specifications [Perkin Elmer]

Diamond DMA Specifications					
Deformation Mode	Bending	Tension	Shear*	Film Shear*	Compression*
Measurement Range	10^5–10^{12} Pa	10^5–10^{12} Pa	10^3–10^9 Pa	10^7–10^{11} Pa	10^5–10^9 Pa
Maximum Sample Size (length x thickness x width)	50 x 5 x 16 mm	5-35 x 3 x 10 mm	Cross section:100 mm^2 Thickness: 7 mm	50 x 0.5 x 10 mm	Area: ϕ10 mm Length: 15 mm
Probes	Metal				
Application Mode	Dynamic Measurement: Sine Wave Oscillation, Synthetic Oscillation Static Measurement: Program Stress Control, Program Strain Control				
Frequency	Sine Wave Oscillation: 0.01–100 Hz (Max. 13 Frequencies) Synthetic Oscillation: Max. 5 frequencies				
Temperature Range	-150 to 600 °C				
Automatic Cooling Accessory	Forced Air or Liquid Nitrogen Vaporization Method				
Scanning Rate	0.01 – 20 °C/min				
Sample Length	Automated measurement				
Atmosphere	Air, Inert Gas, Swelling**, Humidity Control**				
Maximum Load	Static: +/- 10 N Dynamic: +/- 8 N				
Dimensions	43 x 50 x 77 cm (width x depth x height)				
Weight	81 kg				

4.4.1.2 Computer – MUSE Software

The MUSE software is the computer program which controls the total operation of the DMA setup, and is user-controlled. The user can give inputs to the software to calibrate the machine, as well as design the experiment and plot the resulting data.

4.4.1.3 Furnace Cooling Tank

The furnace cooling tank contains liquid nitrogen which is evaporated by a controlled, internal heater and fed directly into the test section during operation and along with the internal DMA heater can control the internal temperature of the test section between -150° to 600°C. The supply line from the liquid valve of the tank must be screwed into the front of the DMA furnace prior to testing, and the connection should be encapsulated using insulating material to avoid losses. There are gauges on the tank which indicates the fluid level and the internal pressure. The following instructions are to be used.

- **Do not fill tank past 90% full to avoid over-pressurizing.**
- **Always have the gas release valve open during refilling of the tank.**
- **If pressure gauge on the cooling tank begins to rise, reduce flow of liquid nitrogen from supply tank and open the release valve on the cooling tank more until pressure stabilizes near 0 psi.**
- **Always use protective cryogenic gloves when filling tank.**
- **Do not move tank during use, whether it is being filled or feeding to the DMA.**

4.4.1.4 Furnace Cooling Controller

The cooling controller links the user-controlled temperature program input to the MUSE software to a control output valve on the furnace cooling tank which releases liquid nitrogen at controlled rates to the DMA test section. The indicator lights on the controller tell the user, and the system, how much liquid nitrogen is remaining in the tank (Fig. 4.4).

If the top indicator LED is lit then it is considered safe to operate the DMA for extended periods of time (usually no more than 2-3 days). If the second LED is lit it is safe to run short experiments (a few hours), but recommended to fill the tank a bit more before test. If the third LED is lit the tank is at dangerously low levels and should be filled prior to use. If the bottom light is lit the system will consider the liquid nitrogen levels unfit for use and not draw any liquid nitrogen from the tank, regardless of the user writing a temperature program requiring controlled cooling. Therefore, it is always recommended to refill the tank before programming any cooling step in the experiment program which may exceed the levels available.

Figure 4.4: Furnace cooling controller showing fluid level indicator lights

4.4.1.5 DMA Cooling Cylinder

The cooling cylinder contains nitrogen gas and is a back-up measure that feeds into the DMA inner components section. It is triggered automatically by the system when the test section reaches a minimum of 400°C to ensure the DMA components do not overheat.

4.4.2 System Operation

This section explains how to turn on the DMA, replace the tension and bending fixtures, load a sample, design and program an experiment, and properly turn off the DMA.

4.4.2.1 Turning on the DMA

1. Open the valve on the DMA cooling cylinder and adjust the release valve until the pressure gauge reads between 45 – 55 psi.
2. Ensure the furnace cooling tank is full and plugged into the DMA furnace, and then switch on the cooling controller.
3. Switch on the DMA power and wait for the display to read "LINKwait".
4. Open the MUSE software application located on the computer and double-click on the "measure" icon.
5. Go to "File" → "Open Communication Port"; ensure "Com 1" is highlighted and click "OK".
6. The MUSE software will begin linking to the DMA; allow the DMA to display "READY" before proceeding.
7. The MUSE software will display a message asking the user to initialize the system. Before clicking to initialize, make sure there is no sample loaded in the test section and that the probe is free to translate in the vertical direction when the force generator is activated during initialization, i.e., nothing is contacting the probe that could impede its movement. The user must take the following precautions.
    - **Do not put excessive force on the probe when removing samples or you could damage the load-train.**
    - **See Section 4.4.2.2 for directions on opening and closing the furnace.**
    - **See Section 4.4.2.3 for directions on mounting and removing samples.**

8. Click “OK” to initialize the system when the previous step is complete; make sure the “Move to the target position” box is unchecked, and the “Adjust the offset load” box is checked.
9. The system will take 1-2 minutes to initialize; the MUSE software will say “Ready” in the upper left hand portion of the screen when done.
    - **The display on the DMA must read between ±5 μm, otherwise you must re-initialize until that range is met.**
10. At this point it is safe to load your test sample, begin writing the program and test.
    - **See Section 4.4.2.4 for procedure on writing the program.**

4.4.2.2 Replacing the Fixtures

There are many different types of fixtures which can be used in the DMA; these include bending, tension, shear, film shear, compression, and three-point bending. For the purposes of this work only the tension and bending fixtures will be discussed. In order to replace the fixture or mount a sample you must first switch on the DMA and allow it to display “LINKwait” before opening the furnace. To open the furnace, see Figure 4.5. When opening the furnace, you must wait until the furnace moves down and then all the way back before releasing the buttons. When closing the furnace, you must wait until the furnace moves forward and then all the way up until it seals with the DMA before releasing the buttons.

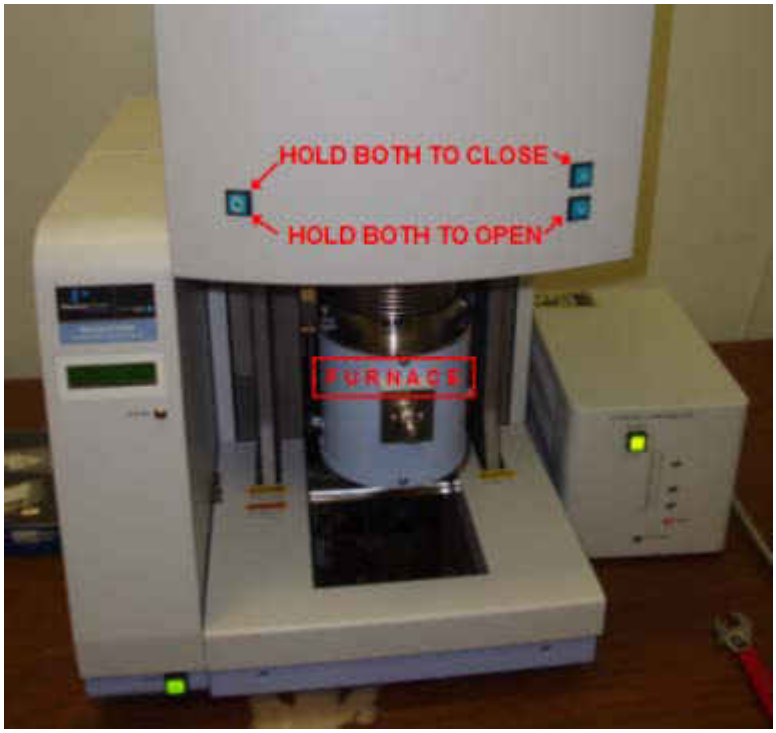

Figure 4.5: How to move the DMA furnace

4.4.2.2.1 Tension to Bending

First you must turn on the DMA in order to open the furnace. Keep the furnace fully open and moved back into the recess before attempting to replace the fixture or you risk dropping pieces into the test chamber.

1. Remove the (4) hex screws from the bottom of the base of the tension fixture that are holding it to the protruding DMA pegs (Fig. 4.6).
2. Open the "Module" → "Motor Control" box in the MUSE software and type in "-16" as your "Target Position" and click "Move".

3. When the position is reached, loosen the (2) probe screws from the probe and remove the upper portion of the tension fixture (Fig. 4.6).
4. The bending fixture should already be assembled, and held together with a custom plate gap setting provided by Perkin Elmer (Fig. 4.7).
5. Loosen the (2) probe screws on the bending fixture and affix the bending fixture into position onto the bottom of the protruding DMA pegs and make sure the plates being held together by the (2) probe screws are wrapped around the probe tip (Fig. 4.8).
    - **Make sure the probe is resting naturally and not being forced in any direction by the plates on the bending fixture being held together by the (2) probe screws.**
6. Lock the bending fixture into position with the (4) hex screws and then tighten the (2) probe screws so the probe is secured to the bending fixtures top portion.
7. Loosen the (2) sample set screws all the way and remove the steel locking bar.
8. Open the "Module" → "Motor Control" box in the MUSE software and click the "Auto adjustment" button for the system to assess the new weight of the probe attachment, and click the "Close" button when it has completed.
9. Initialize the system again to ensure accuracy, and the system is ready for testing using the bending fixture.

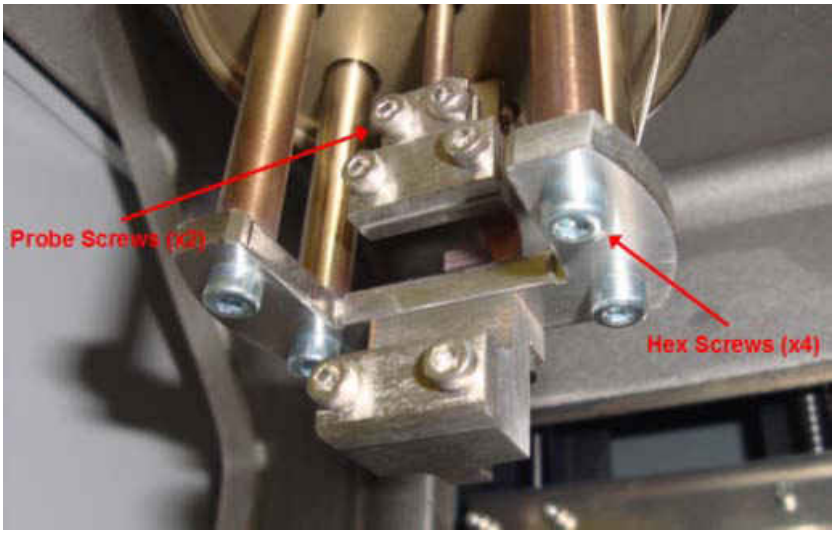

Figure 4.6: Tension fixture assembled to the DMA

Figure 4.7: Fully assembled bending fixture

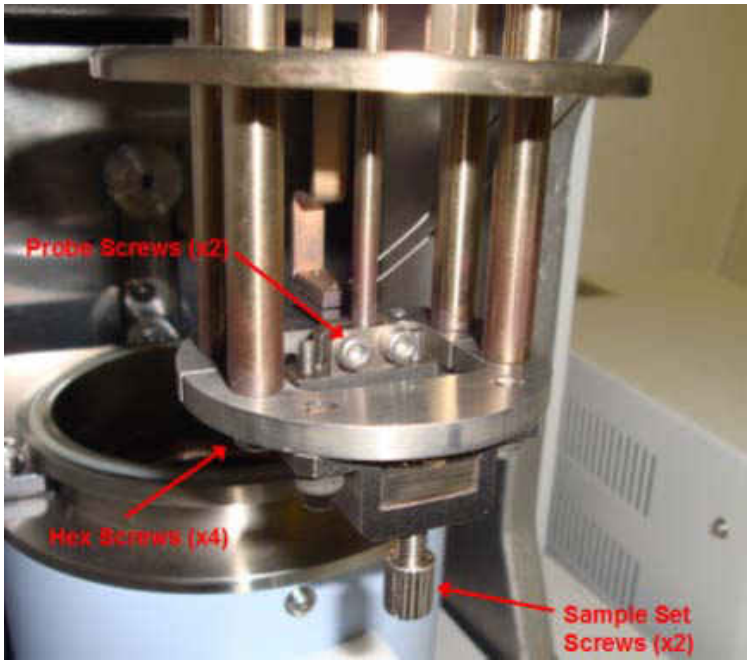

Figure 4.8: Bending fixture assembled to the DMA

4.4.2.2.2 Bending to Tension

1. Insert the steel locking bar into the bending fixture and tighten the (2) sample set screws.
2. Loosen the (2) probe screws and remove the (4) hex screws to remove the bending fixture.
3. Open the "Module" → "Motor Control" tab and set the "Target Position" to "0", and click "Move".
4. When the probe is in position fix the 20 mm plate gap setting, provided by Perkin Elmer, to the bottom and top portions of the tension fixture (Fig. 4.9).

- **Fix the spacer into position so both portions of the tension fixture are flush against the insets of the 20 mm spacer to ensure accuracy.**

5. Loosen the (2) probe screws and affix the tension fixture into position so the DMA protrusions are recessed into the base of the tension fixture, and the plates being held together on the upper portion of the tension fixture by the (2) probe screws are enveloping the probe.
    - **Make sure the probe is resting naturally and not being forced in any direction by the plates on the tension fixture being held together by the (2) probe screws.**
6. Tighten the (2) probe screws and remove the steel 20 mm spacer.
7. Re-tighten the tension fixture screws and use the “Auto adjustment” to reset the new probe attachment weight.

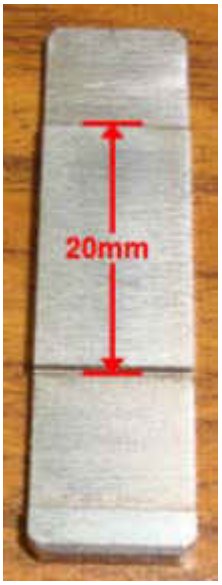

Figure 4.9: 20 mm steel spacer for tension fixture

4.4.2.3 Loading the Sample

For the tension fixture:

1. Loosen the (2) top screws and the (2) bottom screws that are holding the set plates together so there is a sufficient gap between the plates to insert your sample safely.
2. Hold the sample in position with a set of tweezers and re-tighten the (4) screws to pin your sample between the top and bottom sets of plates.
    - **For more delicate samples it may be necessary to remove the front plate of the bottom set to make sure you do not bend the sample when positioning it into the tension fixture; replace the front plate of the bottom set once the top set is tightened down and holding your sample in position.**

- **Make sure the sample is long enough to extend at least 1 mm into the voids between the plates pinching the sample, for both the bottom and top set plates.**
- **Keep the probe as still as possible while positioning the sample.**
- **Do not over-tighten; once the screws are in tight enough to provide some resistance you do not need to force it tighter. Doing so can induce stress concentrations which may cause your sample to fail prematurely during test/provide inaccurate data.**
- **The sample must be as vertical as you can get it, but not necessarily centered. Although, it should be as centered as possible.**
- **You will notice the display on the DMA reading varying positions while adjusting the sample. The display should read between ±25 µm when the probe settles after you stop adjusting the sample. Otherwise, you must loosen the grips and re-tighten until the probe is as relaxed as possible, and the DMA display is reading between ±25 µm.**

3. Close the furnace once the sample is fixed and the above conditions are met.

For the Bending Fixture:

1. Loosen the screws holding the horizontal set of probe plates together to allow enough room to slide in the sample you are mounting.

2. Unscrew the (2) sample set screws all the way and slide your sample all the way though the fixture so that it is resting midway between the probe attachment.
3. Tighten the (2) sample set screws all the way, then re-tighten the set of screws loosed in step 1 to fix the sample completely.
    - Make sure the sample is centered in the fixture and not at an angle.

4.4.2.4 Running an Experiment

Once the machine has been turned on, initialized, the sample has been loaded properly and the furnace closed, you can begin programming the experiment.

1. On the MUSE software main screen open the "Conditions" → "Condition Editor" screen.
2. On the "Sample Condition" tab you must enter the sample name, shape and dimensions, and then select the folder in which you want the program to save the results, along with giving it a file name.
3. Open the "Method" tab, and select the type of measurement you would like to run.
    a) SS control: Static tension mode.
    b) Tension: Dynamic tension mode.
    c) Bending: Dynamic bending mode.
    - For the purposes of this work only SS control will be discussed further.

4. While staying in the “Sample Condition” tab, open the “Temperature Program” tab and program in the temperature steps in which you would like the DMA to follow.
    a) Select the starting temperature in the first step to be the same upper temperature read on the DMA display.
    b) Enter the next temperature you would like to ramp to under the “Limit (Cel)” column in the first step row.
    c) Enter the rate at which you would like to increase or decrease the temperature for the first step (between 0 - 20°C/min).
    d) Enter the amount of time you would like the system to hold at that limit temperature under the “Hold (min)” once the program temperature is reached.
    e) Fill in the additional temperature steps you would like to use for the experiment, and check the end step you want the experiment to end with.

- Each step will begin at the exact time that the previous steps hold time has ended.
- The program will end once the last temperature steps hold time has ended.
- It is necessary to enter higher than normal values for the temperatures in your program because the resultant sample temperature will always settle lower than the program temperature, i.e. if you want the sample to cycle up to 250°C you must enter 269 as your program temperature. The higher

the temperature you program the larger the disparity between the actual settled sample temperature and the program.

5. While staying in the "Sample Condition" tab, open the "SS Program" tab and program in the loading steps in which you would like the DMA to follow.
    - "F Control" will control force, and "L Control" will control displacement.
    - "L control" will not work under certain material conditions.
6. Follow the same general procedure as you did for the temperature program.
7. After the temperature and load programs are set you can refer to the plot displayed on the "Sample Condition" tab for a visual of the entire program to ensure the temperature and loading steps match up correctly (Fig. 4.10).
8. Click "OK" on the bottom of the "Sample Condition" tab to open the MUSE software profile screen.
9. Click the play button to begin the test, and then click on "View" → "Profile".
10. To customize the profile, double-click the axes to select the unit you would like to follow, and with the axis highlighted you can expand or contract the range it displays with the mouse wheel.
11. Once the program has ended you can analyze the results by going to the initial MUSE software screen, and double-click the "Standard Analysis" button.
12. Open the file that you saved your experiment as and go to "File" → "Output to Excel," for raw data.

13. If another experiment is to be run, you must remove the tested sample and reset the motor control to the initial position before loading the next sample.

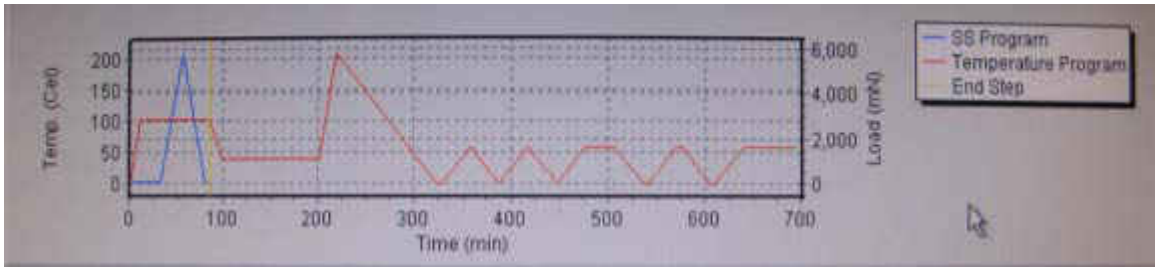

Figure 4.10: DMA experiment sequence plot viewed in MUSE software

4.4.2.5 Turning off the DMA

Whenever an experiment is not running, and you are going to be leaving the instrument idle, you should turn off the DMA.

1. Remove any sample that may be mounted in the test section and re-tighten all screws.
2. Close the furnace and go to "File" → "Close Communication Port". This will power off the DMA and cooling controller.
3. Close the valves on the DMA cooling cylinder and close the MUSE software.

4.4.3 Calibrating the DMA

It is recommended to perform the full calibration procedure every 6 months. The following procedures are arranged in the same order in which they need to be performed. Any

other order will result in a failed calibration, as the system recalculates certain constants after each step is performed. As an exception, the temperature calibration can be performed anytime with either the tension or bending fixture.

For the calibration procedure you will need the following testing materials:

1. PMMA (Poly-methyl Methacrylate) Plate (1.5 mm x 10 mm x 50 mm)
2. PMMA Plate (0.2 mm x 8 mm x 40 mm)
3. Stainless Steel Plate (3 mm x 10 mm x 50 mm)
4. Pure Iron Plate (0.4 mm x 10 mm x 50 mm)
5. Aluminum Plate (0.1 mm x 3 mm x 40 mm)

4.4.3.1 Temperature

The temperature calibration matches the recorded glass-transition temperature of PMMA in the DMA to a reference value of 117°C.

Tension:

1. Set the motor control position to “0 mm”, so the gage length becomes 20 mm.
2. Open the “ABC Condition” tab and record the “0 order value”.
3. Measure the exact dimensions of the 0.2 mm thick PMMA sample and record in the “Sample Condition” window, and then mount the PMMA sample (dimensions 0.2 mm x 8 mm x 40 mm) in the DMA.

4. In the “Temperature Program” select “Tension” as the mode, enter in a starting temperature of 30°C and a limit temperature of 150°C for step one. Enter 2°C as the heating rate, 0 min as the hold time, and 1 (s) as the sampling. Select step 1 as the end step.
5. Select only 1 Hz as the DMS frequency.
6. Under DMS Tension Settings, select 10 μm as the L amp, 300 mN as the min. tension/compression force, 1.5 as the tension/compression force gain, 4000 mN as the force amplitude initial value, 10000 μm as the approved maximum deformation, 8 (s) as the position movement wait time, and 0.0 sec/mN as the creep wait time.
7. Run the experiment, and then open the plot in the standard analysis window.
8. Measure the peak temperature of the E” curve and using the equation (“New 0 order value” = a +117-b; where a = the initially recorded “0 order value”, and b = the previously determined E” value), enter the “New 0 order value” into the ABC condition window as the “0 order value”.

Bending

1. Load the bending fixture and mount the PMMA sample (dimensions 1.5 mm x 10 mm x 50 mm), making sure to record the exact dimensions into the “Sample Condition” window.
2. Open the “ABC Condition” tab and record the “0 order value”.

3. In the “Temperature Program” select “Bending” as the mode and select sinusoidal oscillation in the “DMS Frequency” tab. Enter in a starting temperature of 30°C and a limit temperature of 150°C for step one. Enter 2°C as the heating rate, 0 min as the hold time, and 1 (s) as the sampling. Select step 1 as the end step.
4. Select only 1 Hz as the DMS frequency.
5. Run the experiment, and then open the plot in the standard analysis window.
6. Measure the peak temperature of the E” curve and using the equation (“New 0 order value” = a +117-b; where a = the initially recorded “0 order value”, and b = the previously determined E” value), enter the “New 0 order value” into the ABC condition window as the “0 order value”.

4.4.3.2 Compliance Correction

Before beginning the rest of the calibration, open the “DMS” tab under the “ABC Condition” tab (Fig. 4.11), and enter the following values: set “F/L Gain” and “Tension Gain” to “1”, set the “Load Span” to 11768, and set the remaining constants to “0”.

1. Load the bending fixture.
2. Measure and record the dimensions of the 3mm thick stainless steel plate into the “Sample Condition” window.
3. Mount the 3 mm thick stainless steel plate into the bending fixture.
4. Open the “Method” tab and set the DMS mode to “Shear”.

5. Open the “Temperature” tab and set the control mode to “Step” mode, and set the start temperature to “0”, the limit temperature to “10”, the step temperature to “0.5”, and the soak time to 2 (s).
6. Open the “DMS Frequency” tab and select sinusoidal oscillation and 1 Hz as the frequency.
7. Open the “DMS Tension Setting” and enter 20 μm as the L amplitude, 300 mN as the force amplitude default, and click “OK” to complete the condition editor.
8. Click the “Test” button on the measurement screen, and when it is completed, make sure the value falls with in the range on the screen. The “Test” measurement initializes the DMS control system.
9. Click the play button to begin the actual measurement, and open the results using standard analysis when it is completed.
10. Set the x-axis to “time”, and calculate the average value of G’
11. Open the “DMS” tab under the “ABC Condition” tab, and click the ellipses icon next to the “Compliance Correction” box.
12. Enter the E’ value obtained in step 10 into the “Actual Calculation” box, and click “OK”. If correct, the new calculated value in the Compliance Correction box should read between 10^{-4} and 10^{-3}. Click “OK” to close the condition editor.

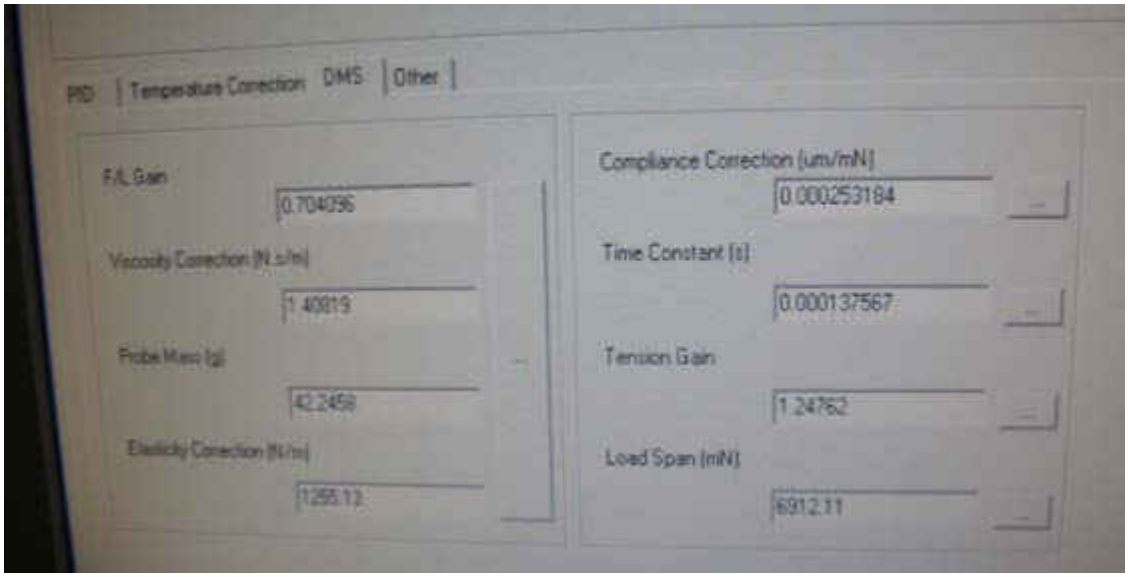

Figure 4.11: DMS calibration tab viewed in MUSE software

4.4.3.3 Time Constant Correction

1. Enter the exact measured dimensions of the 0.4 mm thick iron plate into the condition editor.
2. Load the 0.4 mm thick iron plate into the bending fixture.
3. Check only the 100 Hz frequency under the "DMS Frequency" tab.
4. Keep all the remaining settings from the Compliance Correction procedure.
5. Click "OK" to close the "Condition Editor" window, and select "View" → "Profile" from the menu.
6. Open the "Axis Settings" from the tanD axis, make sure the "Logarithmic Display" box is unchecked, and then click "OK".
7. Click the "Test" button, and make sure the value falls within the range.

8. Click the play button and enlarge the tanD axis to view the maximized curve, and record the average tanD value.
9. Open the “DMS” tab under the “ABC Condition”, and click on the ellipses next to the “Time Constant” box.
10. Enter the recorded tanD value into the “Actual Measurement” box, enter “0.005” in offset, 100 Hz in frequency, and then click “Apply” and “Close”.
11. If correct, the new calculated value should be on the order of 10^{-4}.
12. Click “OK”, and close the “Condition Editor” window.
13. Perform the measurement again and repeat the process until the tanD value has dropped to 0.005 or lower.

4.4.3.4 Viscosity Correction

1. Remove any samples from the fixture.
2. Open the “DMS Frequency” tab and check only 20 Hz.
3. Open the “DMS Tension Condition”, and enter 10 mN for the force amplitude default value, and then click “OK” to close the “Condition Editor” window.
4. Open the “Motor Control” window, and click “Auto Adjustment” for the offset load. Click “Close”.
5. If the DMA display reads greater than the absolute value of 0.5 μm, initialize the instrument before proceeding further.
6. Click the “Test” button on the measurement window, and then click “Close”.

7. Click the play button to run the sample-less experiment, and increase the tanD range to 0 - 0.4.
8. Open the “DMS” tab under the “ABC Condition” tab, and enter a value between 0.5 – 2 for the viscosity correction.
9. Click “OK” and click play to measure the tanD range again.
10. Adjust the viscosity correction value in the “DMS” tab until the measured tanD value falls within the range of 0.002 – 0.02. This can be seen by looking at the results in standard analysis.

4.4.3.5 Probe Mass

1. No sample should be loaded for this calibration step.
2. In the dimensions section of the “Condition Editor”, Enter 0.01 mm for the length, 1 mm for the width, and 5.1 mm for the thickness.
3. In the “DMS Frequency” tab, check only the 1, 10, and 20 Hz frequencies.
4. Click “OK” to exit the “Condition Editor”, and then click the “Test” button to initialize the DMS control parameters.
5. Click the play button, go to “View” → “Profile” on the measurement screen while it’s testing and enlarge the G’ axis to bring the 3 frequencies just within the screen.

6. Enter a value of 50 – 100 in the "Probe Mass" box under the "DMS" tab in the "ABC Condition" section after each measurement until the conditions of step 7 are met.
7. The goal of this exercise is to have all 3 frequency responses as flat and parallel as you can get it, and within 1 decade of each other. Adjust the "Probe Mass" value until this condition is met. Will take several trial-and-error measurements.

4.4.3.6 Elasticity Correction

1. Open the "Standard Analysis" results of the final measurement from Section 4.4.3.5, and select the 1Hz curve for G' from the drop-down menu on the results screen. You should see brackets form around the curve of interest on the plot.
2. Read the value recorded for that curve (should be between 1000 – 3000).
3. Open the "DMS" tab under the "ABC Conditions" tab and enter in the value recorded from step 2 into the "Elasticity Correction" box, and then click "OK" to accept the changes to the "DMS" values.

4.4.3.7 F/L Gain

1. Record the exact dimensions of the 0.4 mm thick iron plate into the "Condition Editor" main screen, and then load the 0.4 mm thick iron plate into the bending fixture.

2. Open the “DMS Tension Setting” tab, and enter 2000 mN as the force amplitude default value.
3. Make sure the DMS measurement mode is set to “Bending”, set the frequency mode to “Sinusoidal Oscillation”, and check only the 1 Hz box under the “DMS Frequency” tab.
4. Click “OK” to exit the “Condition Editor”, click the “Test” button to initialize the settings, and make sure the elasticity ratio is displayed in the range.
5. Click the play button to begin testing, and then open the results in the “Standard Analysis” when it has completed.
6. Set the x-axis to “Time”, and calculate the average E’ value.
7. Open the “DMS” tab under the “ABC Condition” tab, and click on the large box marked with ellipses next to the “F/L Gain” box.
8. Enter 1.92E+11 as the E’ literature value, the value calculated from step 6 as the actual measured E’, and then check the “F/L Gain”, “Viscosity Correction”, “Probe Mass”, and “Elasticity Correction” boxes.
9. Click “Apply”, and then “Close”. The values in the left-hand boxes have now all recalculated based on the value you entered for the “F/L Gain”.
10. Click “OK” to close the “Condition Editor” and accept the changes.

4.4.3.8 Tension Gain

1. Remove any sample that may be in the ending fixture and load the steel locking bar and re-tighten all the screws, fixing the bar into position. This will hold the entire bending fixture together.
2. Remove the bending fixture, reset the motor control to "0" to bring the gage length to 20 mm, and then load the tension fixture. Make sure to use the "Auto Adjustment" in the motor control tab to account for the new probe weight.
3. Initialize the instrument to bring the dL on the DMA display as close to "0".
4. Record the exact measurements of the 0.1 mm thick aluminum sample in the "Condition Editor", and then load the 0.1 mm thick aluminum sample into the tension fixture.
5. Open the "Condition Editor", set the measurement mode to "Tension", the frequency mode to "Sinusoidal Oscillation", and check only the 1 Hz box under the "DMS Frequency" tab
6. Open the "DMS Tension Setting" tab, and enter 300 mN for the "Minimum Tension/Compression", 1.5 for the "Tension/Compression Gain", 4000 mN for the "Force Amplitude Default Value", and then click "OK" to accept all changes.
7. Click the "Test" button to initialize the DMS control system.
8. Click the play button to run the measurement, and when it completes, open the results under "Standard Analysis".
9. Set the x-axis to time, and record the average E' value.

10. Open the “DMS” tab under the “ABC Condition” tab, click on the ellipses next to the “Tension Gain” box, record the literature value as 6.91E+10, and the actual value as the E’ value calculated in step 9.
11. Click “Apply”, and then “Close” to save the changes.
12. Click the play button to run the measurement once more to ensure the new E’ value measured from the results is 6.91E+10 (±0.01E+10).

4.4.3.9 Load Sensitivity Correction of Static Control Mode

1. Remove any sample that may be loaded in the tension fixture.
2. Remove the base of the tension fixture so that only the upper portion is connected to the probe.
3. Open the “Motor Control” window and perform an “Auto Adjustment”.
4. Initialize the DMA to bring the dL on the DMA display as close to “0”.
5. Open the “Method” tab under the “Condition Editor” window, select “SS Control” mode, and under the “SS Control” tab put it in “L Composite” control.
6. Open the “ABC Condition” tab and enter 11768 mN for the load span, then click “OK” to save and close the “Condition Editor” window.
7. Using a known 50 g weight, hang it from the upper portion of the tension fixture that is attached to the probe using a string, which will add an insignificant amount of weight.

- Make sure the weight is hanging directly below the probe, so there is no moment generated.

8. Open the “Condition Editor”, and enter in the “Temperature Program”, in step 1, a start and finish temperature of whatever the current temperature is in the furnace, enter an arbitrary rate (ex. 10°C/min), a hold time of 10min, sampling of 1 (s), and select step 1 as the end step.
9. For the “SS Program”, in step 1, enter 0 μm as the start and limit point, enter an arbitrary rate (ex. 10 μm/min), and a hold time of 10 min.
10. Click “OK” to save the changes, and then click the play button to start the measurement.
11. The DMA will adjust until the dL on the DMA display stabilizes at/near 0μm, then record from the measurement screen of the MUSE software what the Force output was at the moment the dL stabilized at 0 μm, and stop the measurement.
12. Open the “Condition Editor” window, then navigate to the “DMS” tab under the “ABC Condition” tab and click on the ellipses next to the “Load Span” box.
13. Enter 490.333 mN as the literature value, and enter the measured force output from step 11 as the actual value.
14. Click “Apply” to re-calculate the new load span, click “Close”, and then “OK” to save all the changes.

4.4.4 Thermo-mechanical Testing of NiTiPd Wires

First, to verify the calibration procedure has adequately prepared the DMA for testing of the fabricated NiTiPd wires, monotonic tensile tests were performed on materials of known thermo-mechanical properties, as well as constrained recovery tests on a known commercial HTSMA wire. Once the verification was complete, two different types of tests were performed on the NiTiPd wires in the DMA; monotonic tensile tests and constrained recovery tests. These tests can yield the most important thermo-mechanical data for a shape memory alloy that is being developed for use in any actuator application. The data sets achieved during these tests will be directly compared to thermo-mechanical results of the $Ni_{29.5}Ti_{50.5}Pd_{20}$ bulk tension specimens obtained in previous work [Bigelow 2006].

4.4.4.1 Calibration Verification

To ensure the DMA was functioning correctly and capable of providing valid, real thermo-mechanical data, strain and temperature verification tests were performed on materials with known thermo-mechanical properties after completion of the prescribed calibration procedure detailed in Section 4.4.3. Room-temperature stress-strain tests were performed on Steel, AlMgSi, and Superelastic NiTi wire to see if there was any additional compliance correction to account for in SS Control mode. A commercial HTSMA wire was also tested in constrained recovery to determine if the compliance correction made better agreement between the literature response and the DMA response for the transformation strain. The commercial HTSMA wire received had a diameter too large to test in the DMA under a 172 MPa hold stress,

which was the hold stress used in the reference curves for constrained recovery of that alloy. Therefore, the wire was electropolished to bring down the diameter from 500 μm to 150 μm. The transformation temperatures were also determined from the DMA response of the commercial HTSMA wire and compared to the literature response to verify that the temperature calibration was valid.

4.4.4.2 Monotonic Tensile Testing

Monotonic isothermal tensile tests were performed on "virgin" $Ni_{29.5}Ti_{50.5}Pd_{20}$ wires with rectangular cross-sections, with averaged dimensions of 150 ±2 μm x 130 ±2 μm for one set of wires and averaged dimensions of 110 ±2 μm x 100 ±1 μm for a second set of wires. The grain size for the wires was found to be equal to the grain size of the bulk samples (10 μm), which makes about 200 grains to be present in the cross-section of the thicker wires, and about 100 grains present in the cross-section of the thinner wires. The reason for testing two sets of wires with different cross-sectional areas was to evaluate any size-scale effects due to the number of representative grains in the cross-section. Untested wires from each set were tested in the martensitic and austenitic phase. For the martensitic phase tensile tests, untested samples from both sets were loaded in the DMA at no-load and heated up to 73°C (M_f-50°) at a rate of 10°C/min and allowed to soak for a minimum of 15 minutes. Once equilibrium temperature was established the samples were stressed at a rate of 250 mN/min up to a maximum of 5.8 N before being unloaded at the same rate. For the austenitic phase tensile tests, untested samples from both sets were loaded in the DMA at no-load and heated up to 193°C (A_f+50°) at a rate of

10°C/min, through its phase transformation, and allowed to soak for at least 15 minutes. Once equilibrium temperature was established the samples were stressed at a rate of 250 mN/min up to a maximum of 5.8 N before being unloaded at the same rate. Tensile testing in the austenitic phase was also carried out at 243°C (Af+100°) to determine if there could have been retained martensite in the samples at Af+50°. The reference Mf and Af temperatures used for these tests are presented in Section 5.3.2. The apparent yield stress for these responses were calculated and compared to the previously reported bulk sample data [Bigelow 2006].

4.4.4.3 Constrained Recovery

Load-bias tests were performed on electropolished $Ni_{29.5}Ti_{50.5}Pd_{20}$ wires using 20 mm as the gage length and rectangular cross-sections with average overall dimensions of 150 ±2 μm x 130 ±2 μm. The cross-sectional shape of the electropolished wires was determined using profile images taken using an Olympus LEXT OLS3000 Laser Scanning Confocal Microscope in confocal viewing mode. The previous work which measured thermo-mechanical data from NiTiPd bulk specimens had thermally cycled the bulk tension samples twice under no-load conditions in a mechanical tester, but since the DMA had proven to respond inaccurately during the cooling cycles at no-load it was safer to thermally cycle the wires in a furnace, rather than subject them to conditions which may induce plasticity when none should be expected. Thermal cycling can affect a shape memory alloy's performance, therefore it was considered a necessary step to thermally cycle them anyway to make sure they compared well to the bulk samples' testing procedures. After thermal cycling in a furnace, the untested wires were loaded in the

DMA at no-load and heated up to 50°C at a rate of 10°C/min, which is well below the M_f established in previous work for bulk NiTiPd specimens [Bigelow 2006]. The samples were then loaded up to 99 MPa at a rate of 250 mN/min and allowed to settle for about 5 minutes before being heated up to 250°C at a rate of 2°C/min, and allowed to soak for 1 minute before being cooled back down to 50°C at a rate of 2°C/min. After being allowed to soak at 50°C for 1 minute the sample was heated again in the same manner up to 250°C at 2°C/min and cooled back down to 50°C at 2°C/min. The sample was then loaded isothermally up to 197 MPa at a rate of 250 mN/min and thermally cycled twice at this stress level in the same manner as was done under the previous load. The sample was loaded isothermally up to 295 MPa in the same manner and thermally cycled twice between 50°C and 250°C. The second thermal cycle at each stress level is what was plotted and compared to the constrained recovery data from the previously reported bulk sample data [Bigelow 2006].

Figure 4.12 shows a schematic of how actuator-type performance data was extracted from the constrained recovery curves for the micron-scale wires and bulk tensile sample thermally cycled at incrementing stress levels. The transformation temperatures (As, Af, Ms, and Mf) were measured from the second thermal cycle at each stress level using the intersection of fit lines through the transformation and the linear coefficient of thermal expansion (CTE) regions of the curves. The transformation strains (ε_{TF}) were measured as the difference between the strains at the austenite finish and austenite start intersections, and the work output at each stress level was calculated by multiplying the transformation strain by the applied stress. The

open-loop strain (ε_{OL}), or irrecoverable strain, was measured as the strain difference between the beginning of the heating curve and the end of the cooling curve.

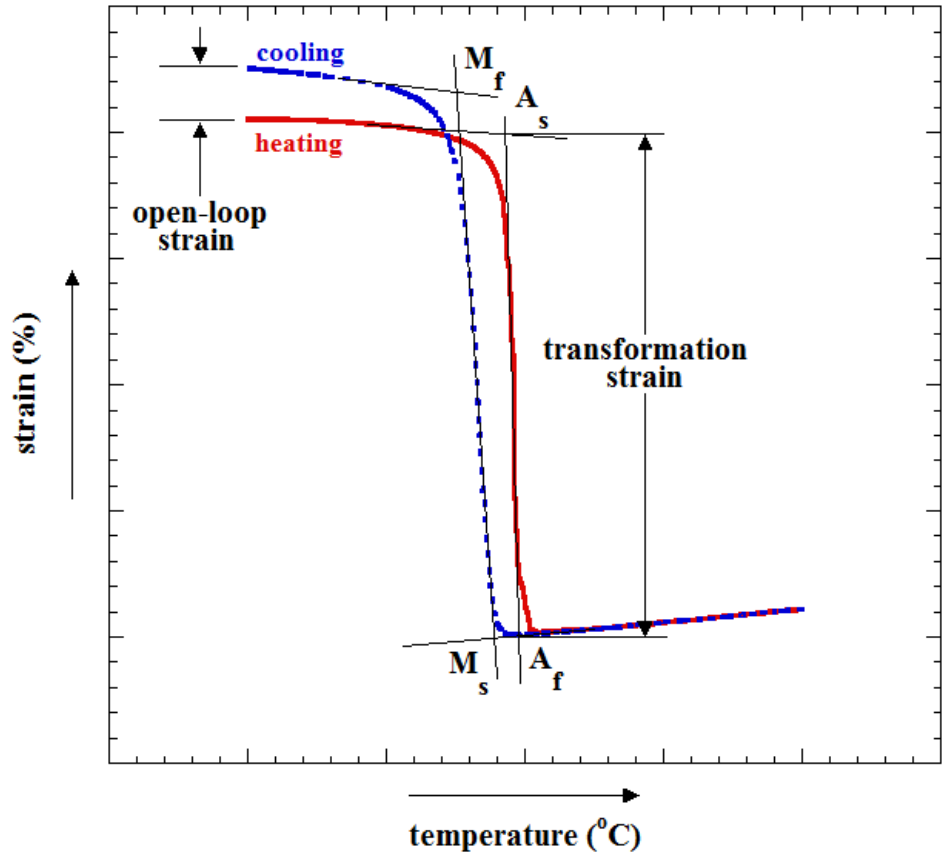

Figure 4.12: Schematic showing data extracted from constrained recovery experiments

CHAPTER FIVE: RESULTS AND DISCUSSION

Following EDM of the bulk sample to produce rectangular cross-section wires on the order of 200 μm in diameter, a heat-affected zone is formed on the new surfaces caused by the rapid local heating and cooling from the pulse current which creates very high thermal gradients. Successful removal of the entire HAZ from the samples was considered crucial to attaining representative bulk thermo-mechanical responses from the wires to be tested in the DMA. For this reason, EDM sample dimensions were made moderately larger than the desired final electropolished wire dimensions. In going from an EDM sample with initial cross-section dimensions of 210 μm x 200 μm to an electropolished sample with cross-section dimensions of 150 μm x 130 μm, and 110 μm x 100 μm, 6-10 minutes is required to remove material from the wires to make them sufficiently small to go up to large stresses in the DMA. The time associated with this process has been shown to increase surface roughness, although the finish surface roughness of the wires was within the range established in previous work [Pohl *et al.* 2004]. After fabrication of the wires by wire-EDM and electropolishing, they were tested in a DMA for their thermo-mechanical response and compared to previously reported results for a bulk tension specimen similar to the one used for extraction of the wires [Bigelow 2006].

5.1 Effects of Electrical-Discharge Machining

After EDM, the wires were shown to have a rough surface from where the rapid re-melting and solidification occurred (Fig. 5.1). Backscattered electron (BSE) images were taken using SEM and Energy Dispersive X-ray Spectroscopy (EDX) of the surfaces was performed. The results showed a combination of oxides and remelt on the wire's surface (Fig. 5.2, 5.3). An SEM image of a 3.2 mm section of the wire shows the wire to be uniform along its length (Fig. 5.4). TEM shows changes of the near-surface layer of the wires where oxides have now formed due to the EDM process (Fig. 5.5). Another cross-section of the EDM wire was extracted by FIB and a Scanning TEM (STEM) image obtained. The profile shows that the damage zone is rich with oxide particles, but after a depth of 5 μm the sample is free of any damage from the EDM process (Fig. 5.6).

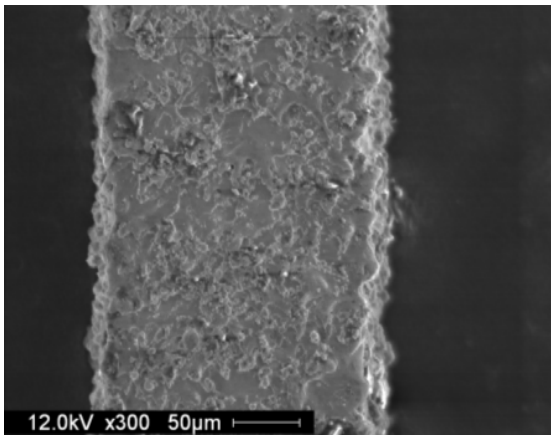

Figure 5.1: SEM image of wire surface after EDM

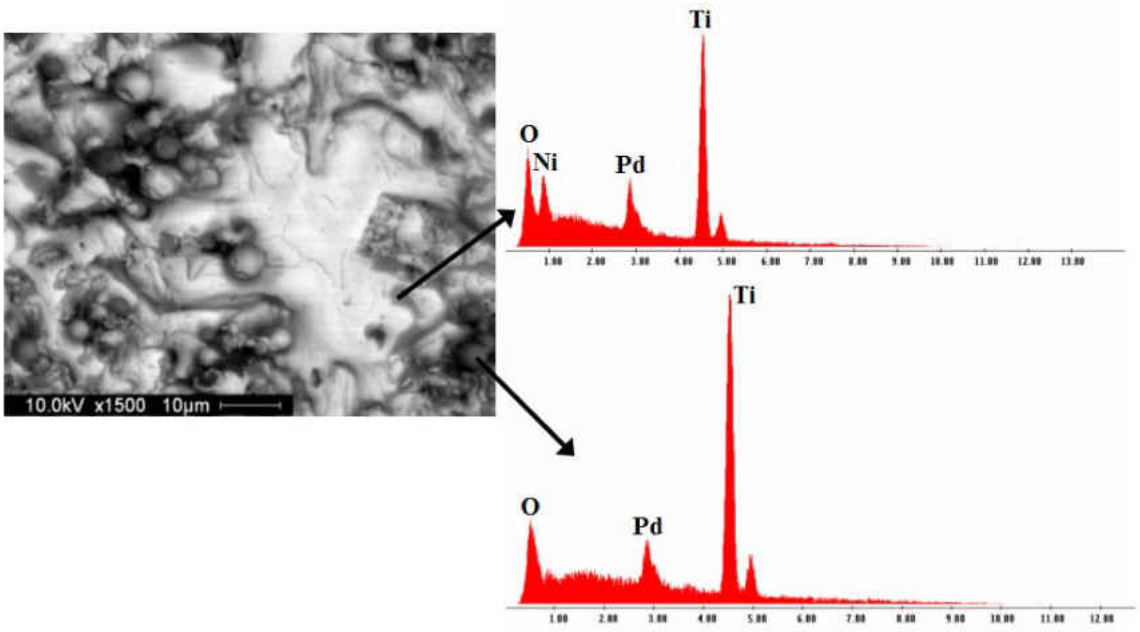

Figure 5.2: EDX of oxides on wire surface after EDM

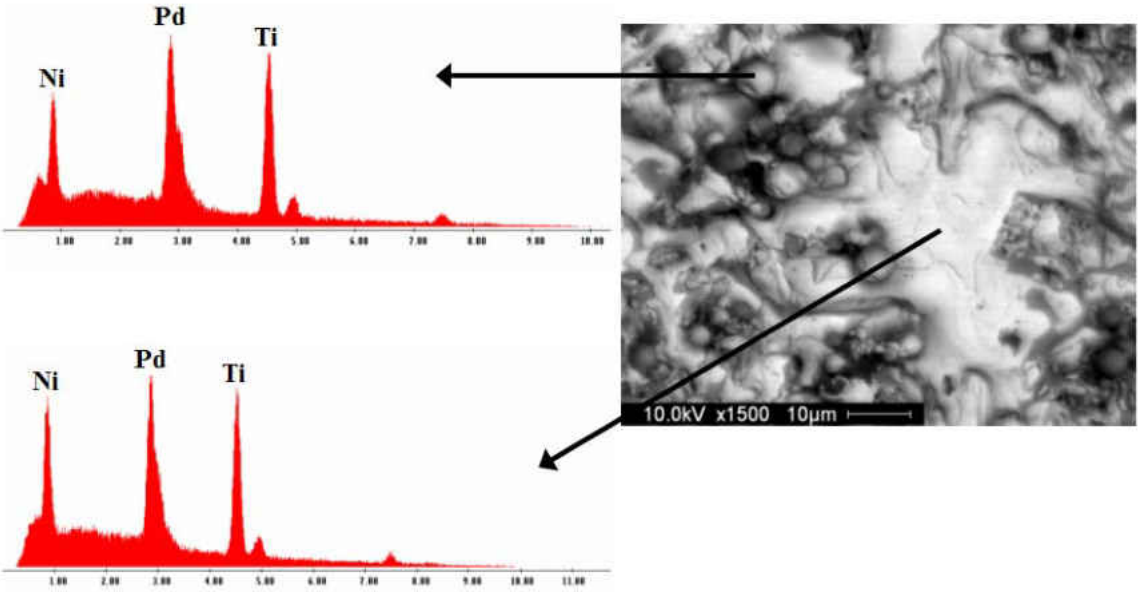

Figure 5.3: EDX of remelt on wire surface after EDM

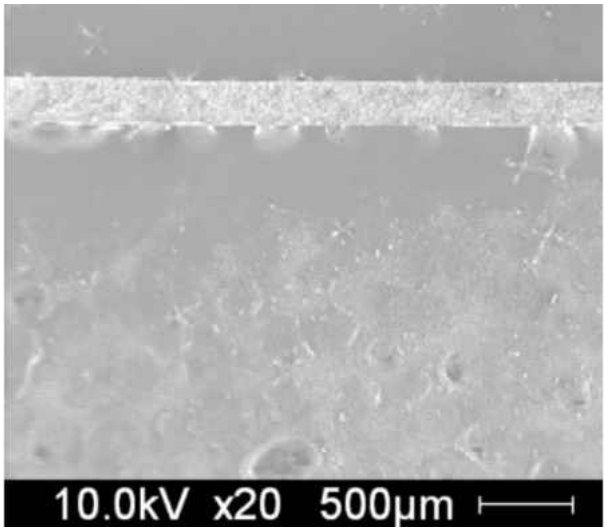

Figure 5.4: Uniformity of wire after EDM

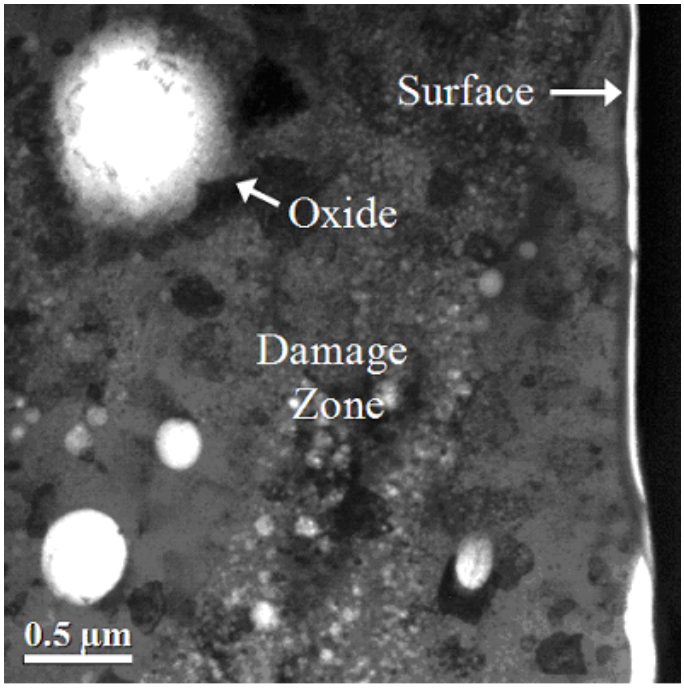

Figure 5.5: Formation of oxide particles near surface of wire after EDM

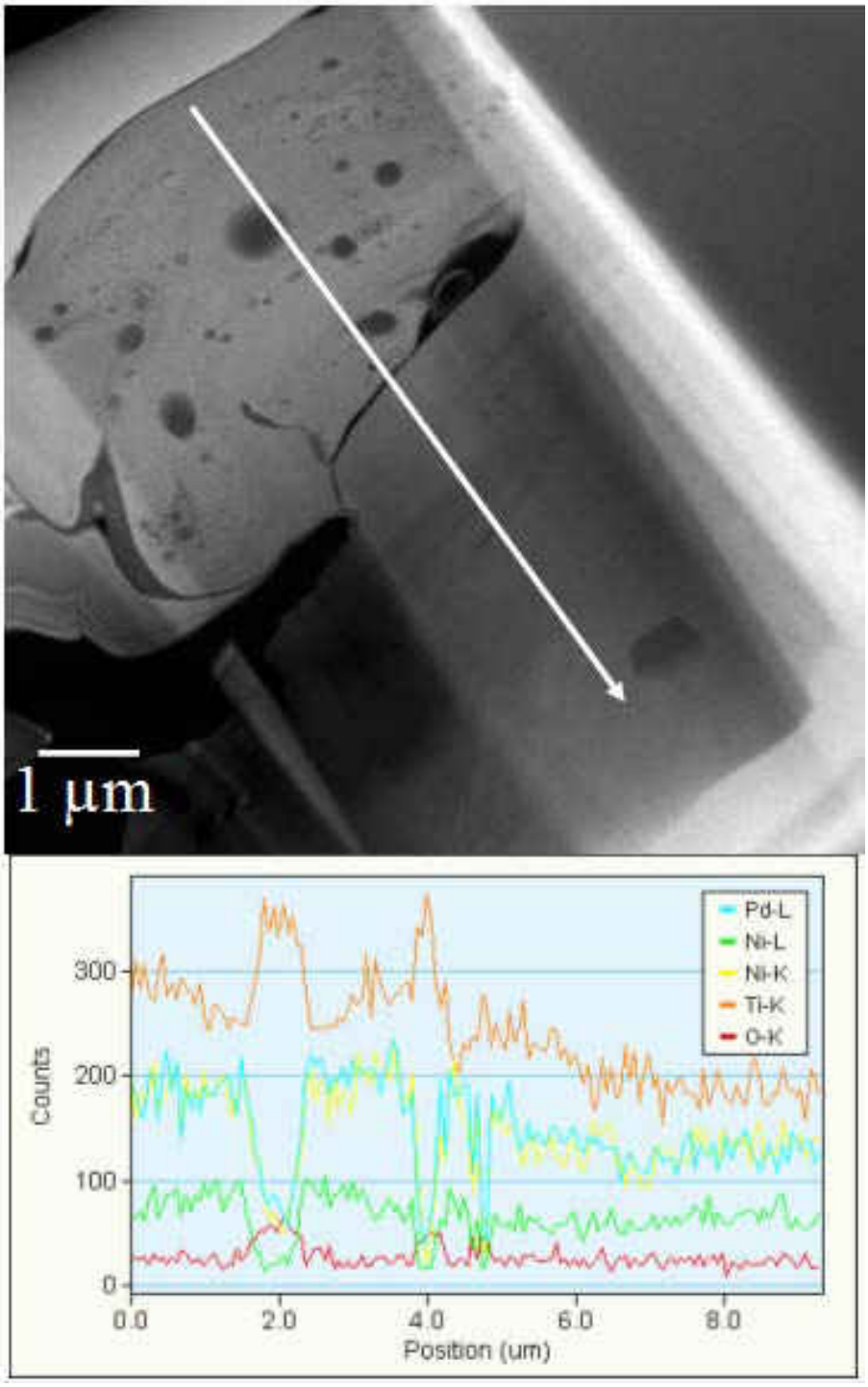

Figure 5.6: STEM image of wire cross-section after EDM and line EDX profile

5.2 Effects of Electropolishing

The wires produced by EDM were electropolished from their original dimensions of 210 μm x 200 μm down to no greater than 150 μm x 140 μm for any of the DMA-tested wires presented in this work. While the depth of the HAZ appeared to be no more than 5μm, the true microstructural impact the EDM process could have had on the material could be slightly deeper. To ensure the HAZ would be completely removed and not affect the thermo-mechanical response of the wires when tested in the DMA, a minimum of 30 μm was removed from the surface of each wire on each side.

The electropolished wires were observed in the SEM and shown to have a smooth surface (Fig. 5.7). The samples also maintained uniformity throughout the electropolishing process (Fig. 5.8). However, some small particles presented themselves on the surfaces of the electropolished wires, which are represented by the small contrast spots on the surface seen in Figure 5.7. STEM confirms these particles are nearly pure titanium (Fig. 5.9). It is not clear from the literature why the presence of these nearly pure titanium particles have formed on the surface as a result of electropolishing. Figure 5.9 also shows that the expected $Ti_2(Ni,Pd)$ phase was present throughout the core of the wires, as they are the same ones present in the microstructure analysis done in previous work on bulk NiTiPd specimens [Bigelow 2006]. TEM verifies that the HAZ had been removed from both the 150 μm x 130 μm wires and the 110 μm x 100 μm wires, and there was a fully martensite structure present at the surface (Fig. 5.10, 5.11).

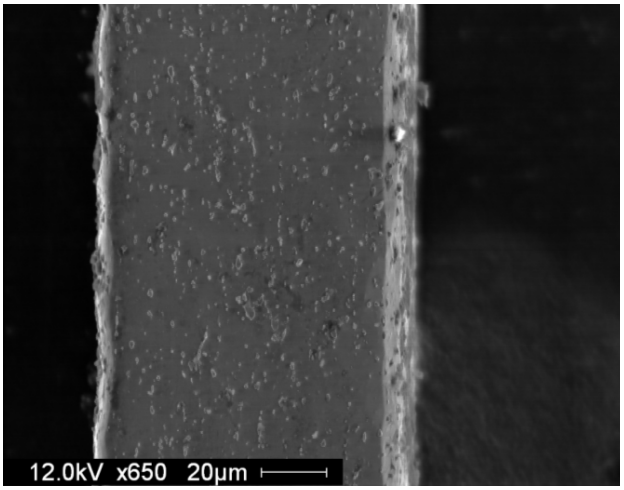

Figure 5.7: SEM image of wire surface after electropolishing

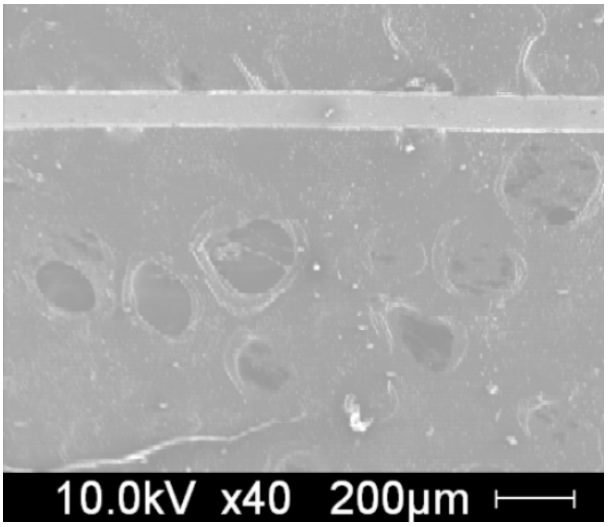

Figure 5.8: Uniformity of wire after electropolishing

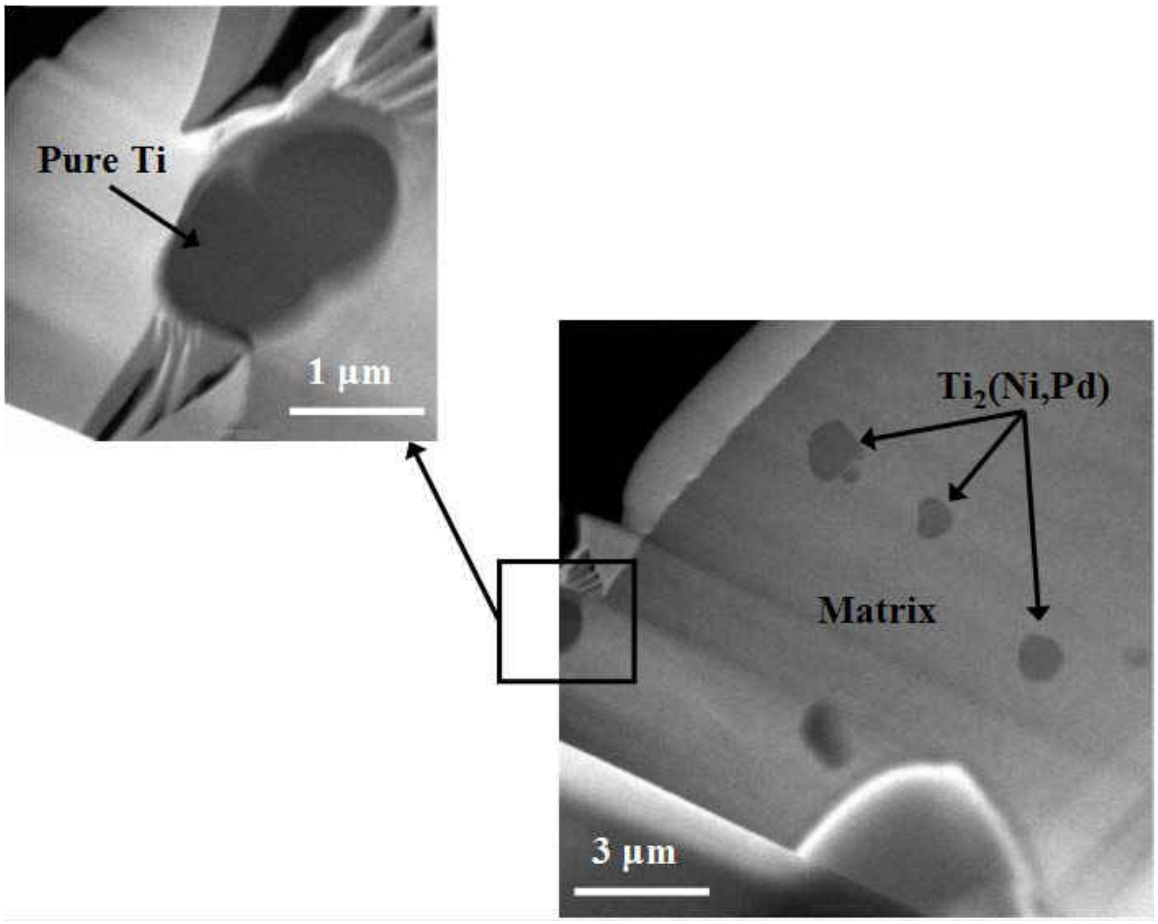

Figure 5.9: STEM images from electropolished wire

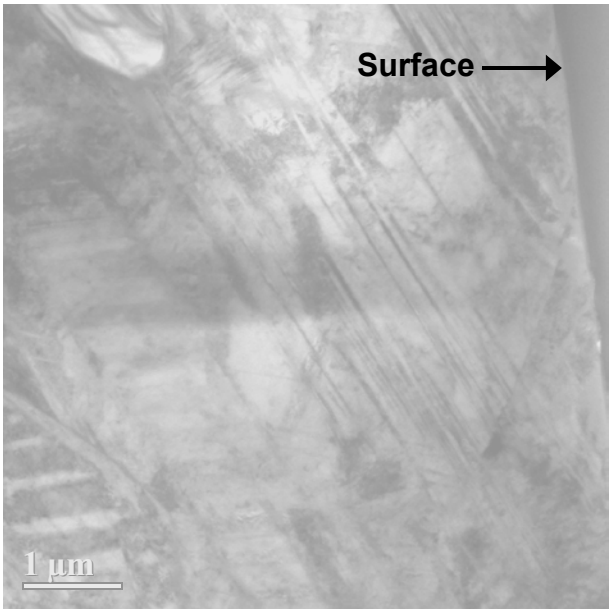

Figure 5.10: TEM image of 150 μm x 130 μm wire showing absence of HAZ

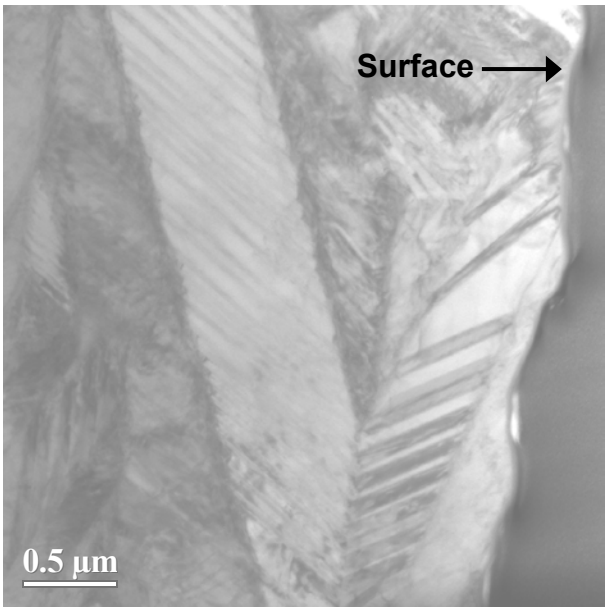

Figure 5.11: TEM image of 110 μm x 100 μm wire showing absence of HAZ

3-D images were compiled for each wire to determine the cross-section shape by taking a step height of 0.5 μm from the bottom to the top of each wire for two orthogonal surfaces of the cross-section, as previously outlined in Section 4.3. By viewing these images normal to the cross-section plane (Fig. 5.12), a 2-D map was created and drawn using solid modeling software, using the overall edge dimensions and average calculated corner radii. Cross-sectional area was then calculated by the software which was then used in the calculations needed to determine the mechanical response of the wires in the DMA. The three different shape wires tested in constrained recovery had the following average corner radii – R_{wire_1} = 37 ±5 μm, R_{wire_2} = 25 ±7 μm, R_{wire_3} = 6 ±4 μm.

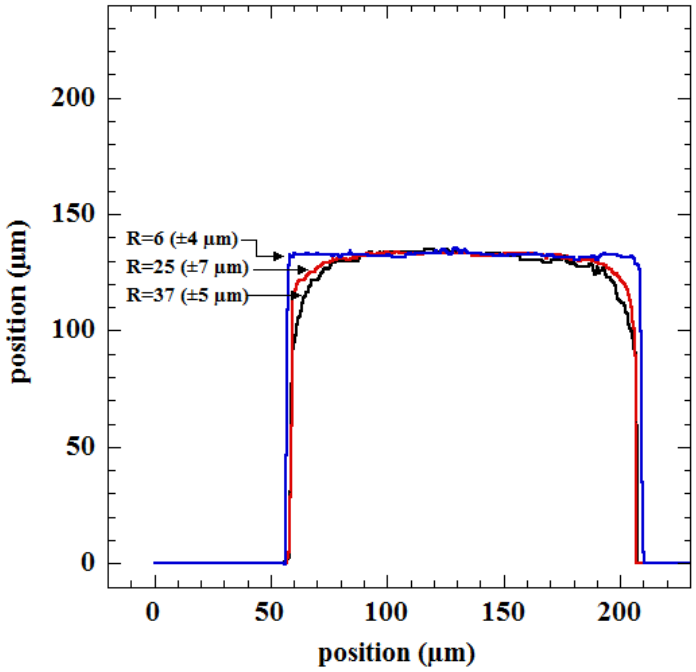

Figure 5.12: 2-D cross-section profiles of the three wires with different corner radii tested in constrained recovery, which were generated from 3-D LSCM images

The surfaces of the electropolished wires were also viewed using LSCM in confocal mode at a magnification of 2400x to determine surface roughness. The wire was imaged in 3-D at a step height of 0.01 μm (Fig. 5.13). The root-mean square (RMS) surface roughness was determined using the LSCM software to be 0.4 μm.

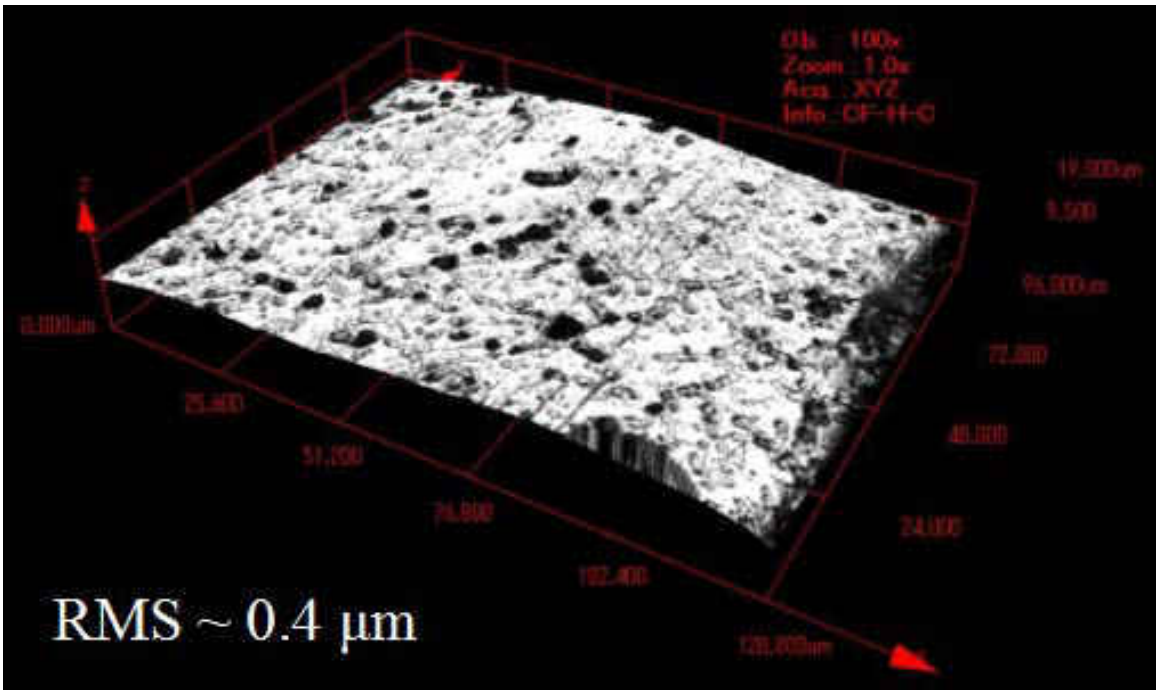

Figure 5.13: 3-D surface image of wire using LSCM after electropolishing

5.3 Thermo-mechanical Testing

To determine the thermo-mechanical response of the NiTiPd wires they were tested in a DMA in SS Control mode using the tension fixture, as outlined in Section 4.4. The results of the calibration verification, monotonic tensile testing, and constrained recovery testing are reported in the following sections.

5.3.1 Verification of Instrument Calibration

The temperature calibration step described in Section 4.4.3.1 yielded accurate results for the glass transition temperature of PMMA after calibration (Fig. 5.14). Monotonic tensile tests were performed on stainless steel, Aluminum (98 at.% Al 1 at.% Mg and 0.6 at.% Si), and superelastic NiTi wires to see if the Young's modulus matched the reference values. After loading each sample in tension mode and running a "Test" measurement in dynamic mode the storage modulus (E') of the material was established. The E' values found using the "Test" measurement method all fell within the reference value range for each of the tested alloys. After recording the E' of these three alloys, they were tested in the static "SS Control" mode, which is the mode needed to determine actuator-type performance of the NiTiPd wires. Each alloy was tested at room temperature, and stressed in force control at a rate of 250 mN/min up to a predetermined stress that kept the material in the elastic region throughout the entire test (Fig. 5.15-5.17).

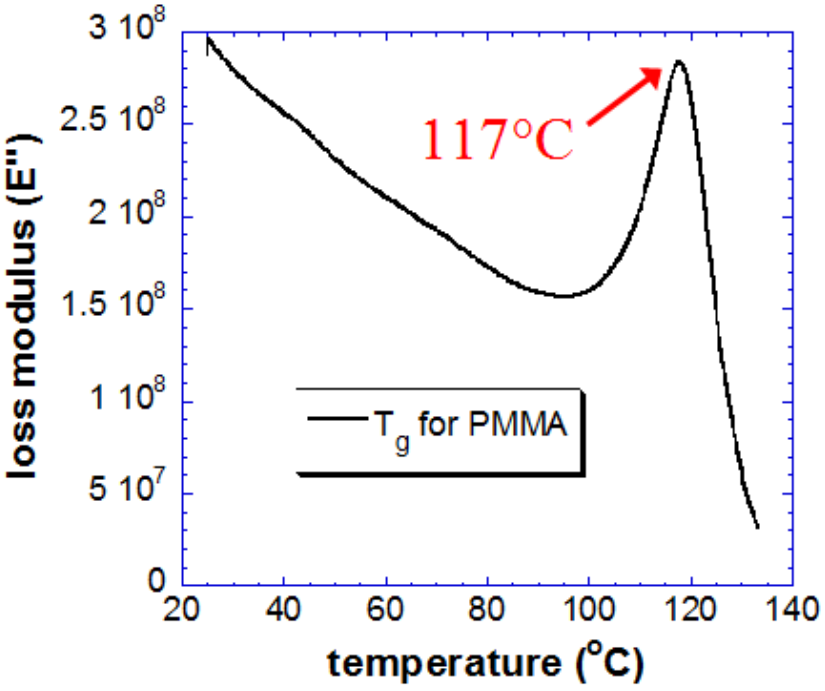

Figure 5.14: Temperature calibration results for T_g of PMMA in the DMA

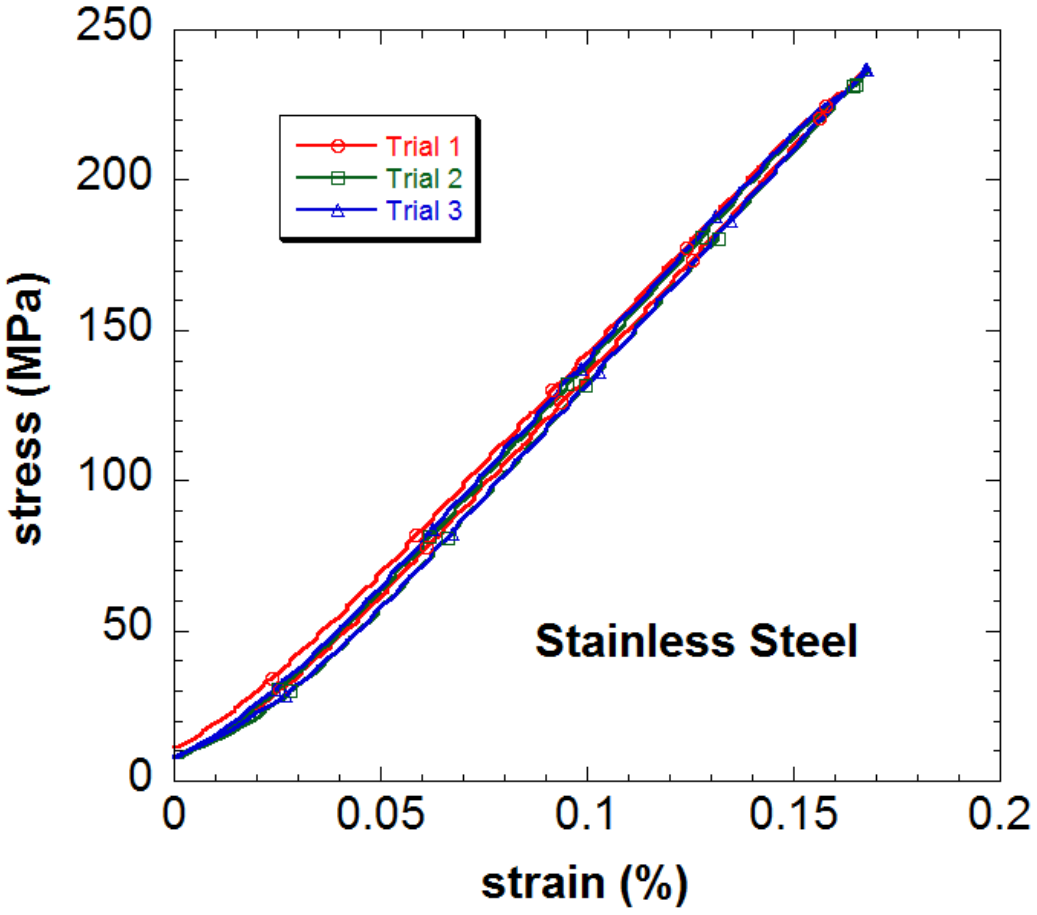

Figure 5.15: Stress-strain response of 127 μm diameter stainless steel wire in the DMA

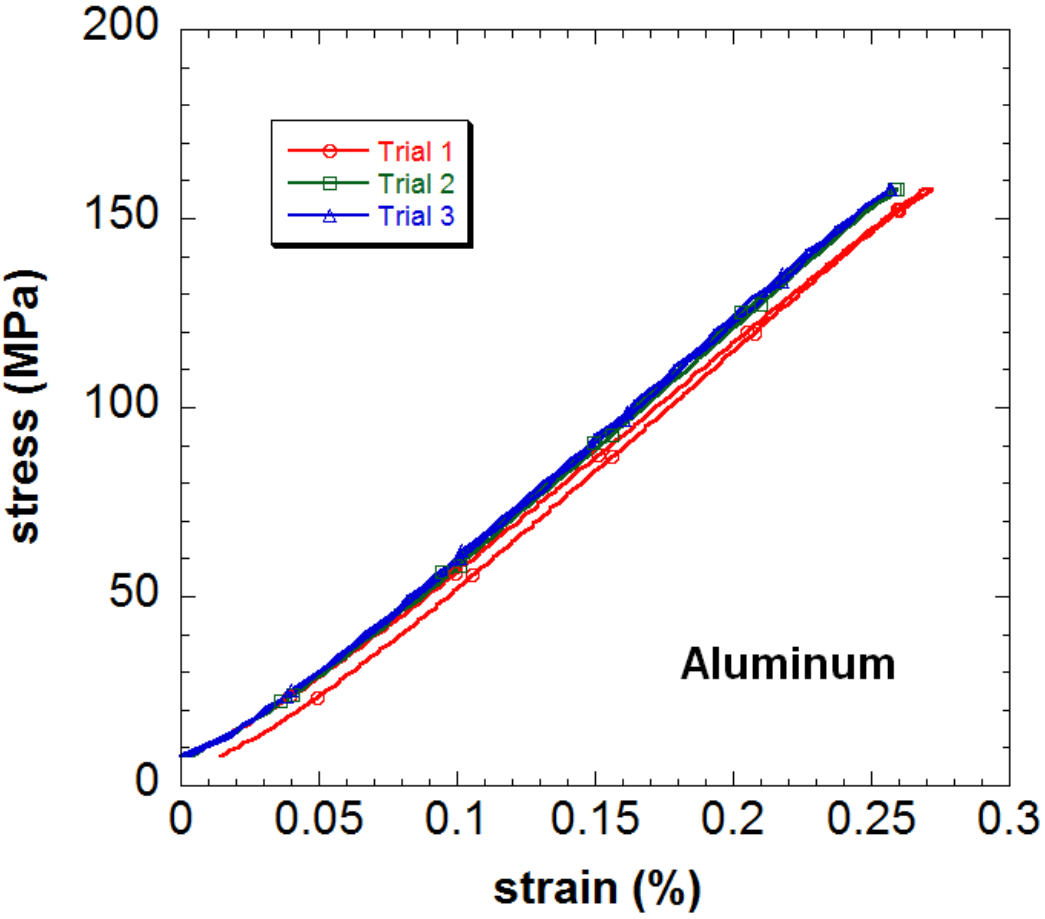

Figure 5.16: Stress-strain response of 127 μm diameter Al wire in the DMA

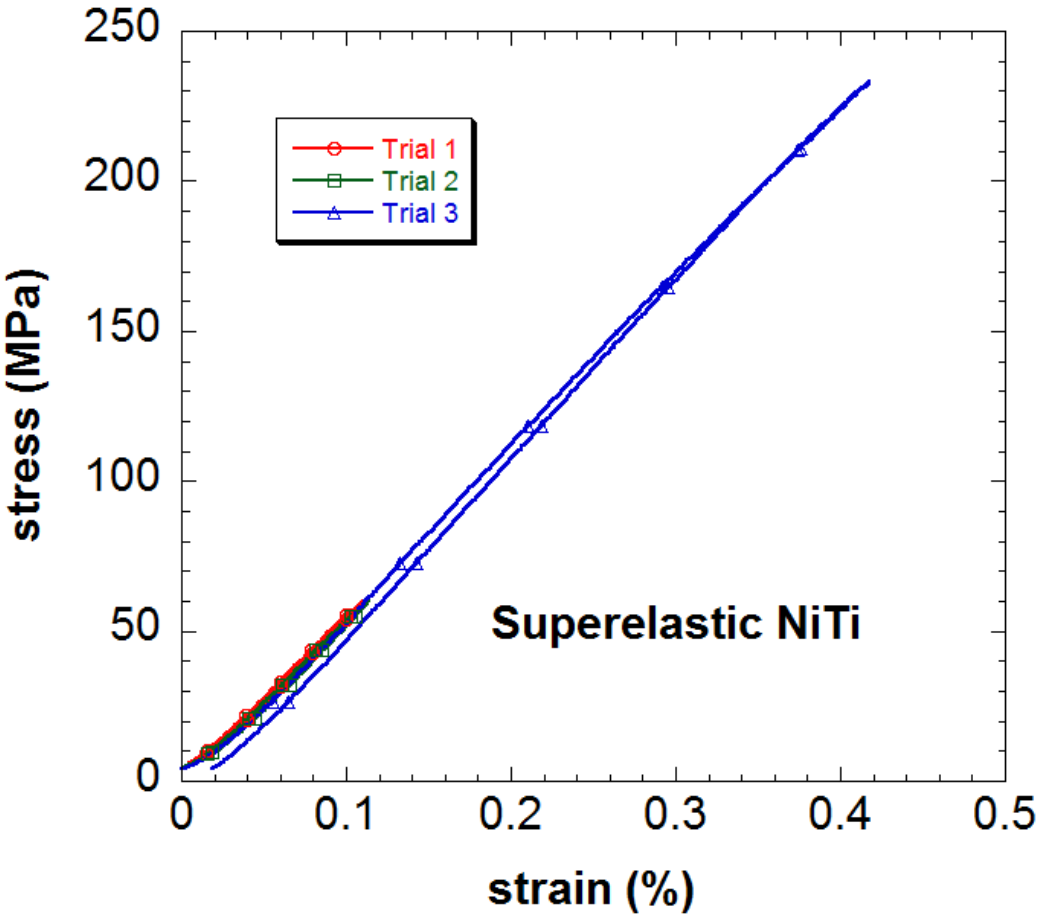

Figure 5.17: Stress-strain response of 178 μm diameter superelastic NiTi wire in the DMA

The calculated E/E' ratios for each of the three alloys resulted in a 3:4 ratio (Table 5.1). These results led to an additional instrument compliance that was factored into static tests conducted in the DMA in "SS Control" mode.

Table 5.1: Comparison of moduli in DMA

	Stainless Steel	Aluminum	Superelastic NiTi
E'	200 GPa	83 GPa	79 GPa
E	150.7 GPa	62.7 GPa	59 GPa
E/E'	0.7535	0.7554	0.7468

The electropolished commercial HTSMA wire was strained in force control up to 172 MPa at a rate of 250 mN/min at room temperature. After reaching the hold stress, the wire was heated up to about 240°C at 2°C/min and then cooled down to about 40°C at 2°C/min. After applying the instrument compliance determined in the beginning of this section, the DMA constrained recovery response was plotted vs. the reference curve supplied with the wire (Fig. 5.18).

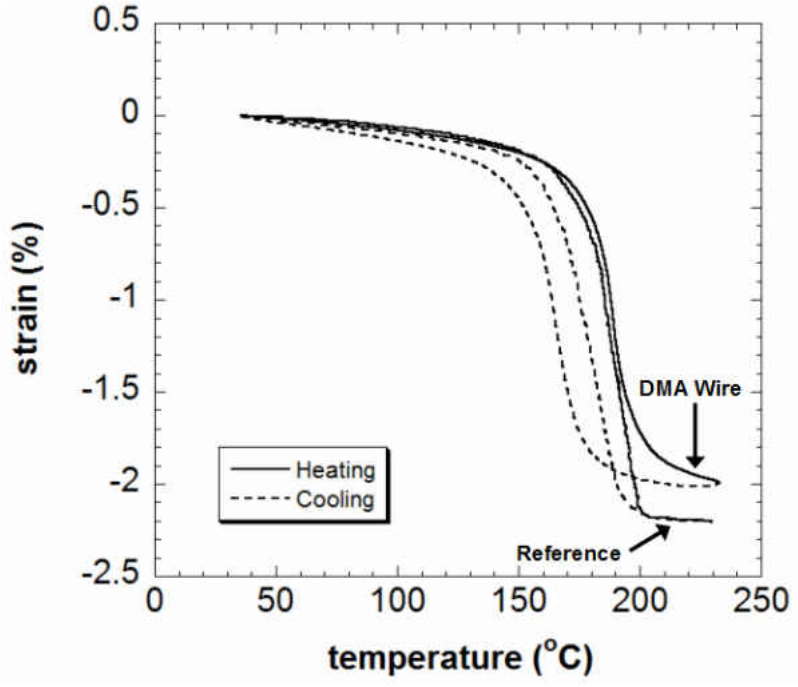

Figure 5.18: Comparison of constrained recovery of commercial HTSMA wire at a hold stress of 172 MPa (reference curves from manufacturer and the DMA response of the wire after electropolishing to reduce size)

The transformation strain (ε_{TF}) of the reference HTSMA wire was 1.99%, whereas the electropolished version of that wire in the DMA had a transformation strain of 1.69%. The A_s for the wire was 4°C higher than that of the reference curves, the A_f was 2°C lower, the M_s was 18°C lower, and the M_f was 10°C lower than the reference curves (Table 5.2). The differences in the thermo-mechanical response are discussed later in the context of comparisons with the bulk specimens. Regardless of the reason for the differences in the thermo-mechanical response of the commercial HTSMA wire, a conclusion can be drawn that the DMA is properly calibrated,

and fully capable of assessing the actuator-type properties of a given shape memory alloy when the additional instrument compliance is accounted for.

Table 5.2: Comparison of commercial HTSMA wire (reference values from manufacturer and DMA response of electropolished wire)

	M_f (°C)	M_s (°C)	A_s (°C)	A_f (°C)	ε_{TF} (%)	Work Output (J/cm^3)
Reference	165	193	177	200	1.99	3.42
DMA	155	175	181	198	1.69	2.91

5.3.2 Monotonic Tensile Testing

Untested wires from both the 150 μm x 130 μm wire set and 110 μm x 100 μm wire set were tested at 73°C and 193°C, which are M_f-50°C and A_f+50°C, respectively. Those values were established in previous work for the bulk samples of $Ni_{29.5}Ti_{50.5}Pd_{20}$ [Bigelow 2006], and the micron-scale wires were tested in the DMA at those same temperatures to ensure the alloy was completely one phase of either martensite (B19) or austenite (B2).

Figure 5.19 shows the response of both the 150 μm x 130 μm wires and the 110 μm x 100 μm wires tested in the martensitic phase. The apparent elastic moduli of the two wires were comparable, with the 150 μm x 130 μm wire having a modulus of 44 ±2.5 GPa, and the 110 μm x 100 μm wire having a modulus of 38 ±2.5 GPa. The critical stress for detwinning was 131 MPa for the bulk sample, and 124 MPa and 112 MPa for the 150 μm x 130 μm and 110 μm x 100 μm wires, respectively.

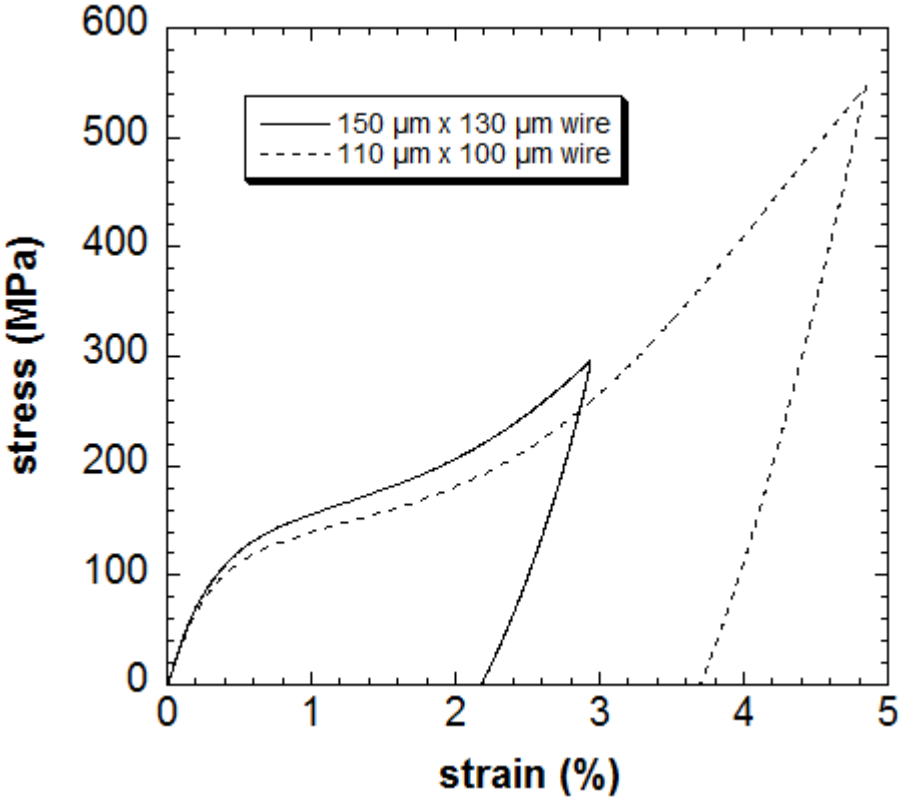

Figure 5.19: Stress-strain response of wires at M_f-50^{o}C

Figure 5.20 shows the response of both the 150 µm x 130 µm wires and the 110 µm x 100 µm wires tested in the austenitic phase. The elastic modulus for both wires was within error (72 ±2.5 GPa, but given the DMAs force limitations, the 150 µm x 130 µm wire could not be loaded to a stress high enough to induce plasticity. Therefore, the yield stress for the 150 µm x 130 µm wire in its austenite state could not be determined.

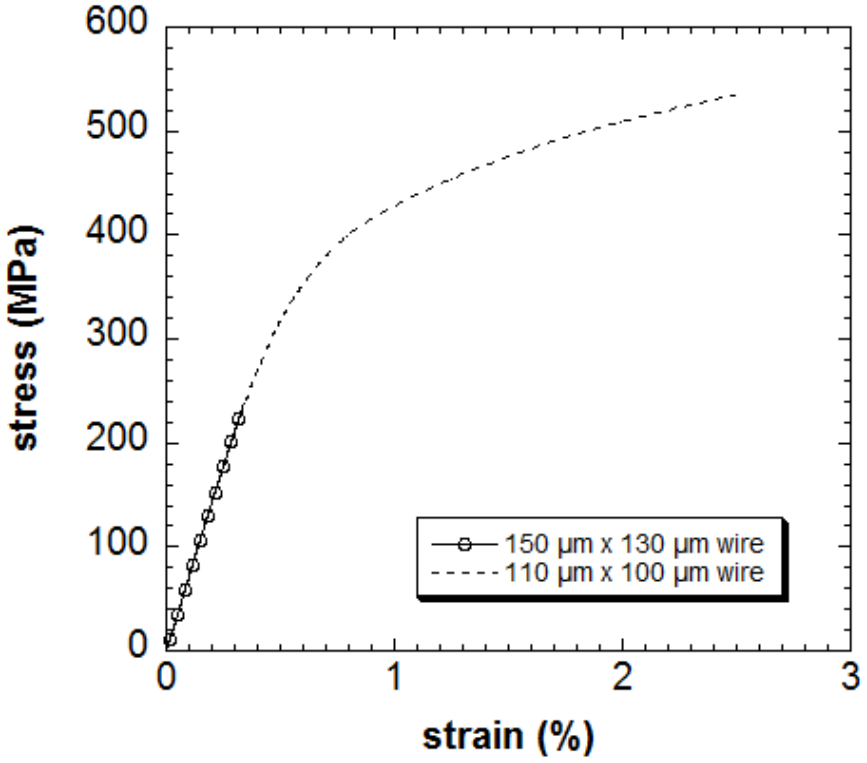

Figure 5.20: Stress-strain response of wires at A_f+50°C

The modulus for the 150 μm x 130 μm wires were near equal between A_f+50°C and A_f+100°C, with a modulus of 65 ±2.5 GPa, indicating that if retained martensite contributed to the deflated modulus it is still stable at those higher temperatures (Fig. 5.21). The 110 μm x 100 μm wires also had similar elastic moduli, with a modulus of 62 ±2.5 GPa, but the yield stress of the 110 μm x 100 μm wire tested at A_f+100°C was higher than that of the one tested at A_f+50°C by 23 MPa, with the wire tested at A_f+50°C yielding at 364 MPa and the wire tested at A_f+100°C yielding at 387 MPa (Fig. 5.22).

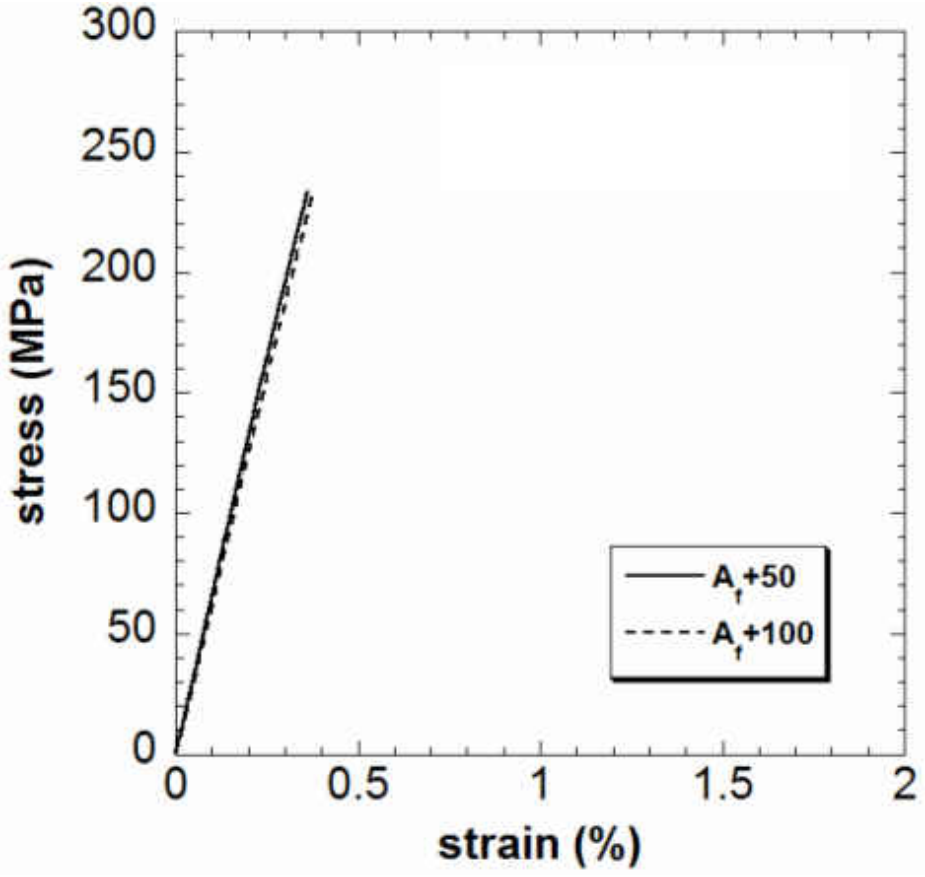

Figure 5.21: Stress-strain response of 150 μm x 130 μm wires at A_f+50°C and A_f+100°C

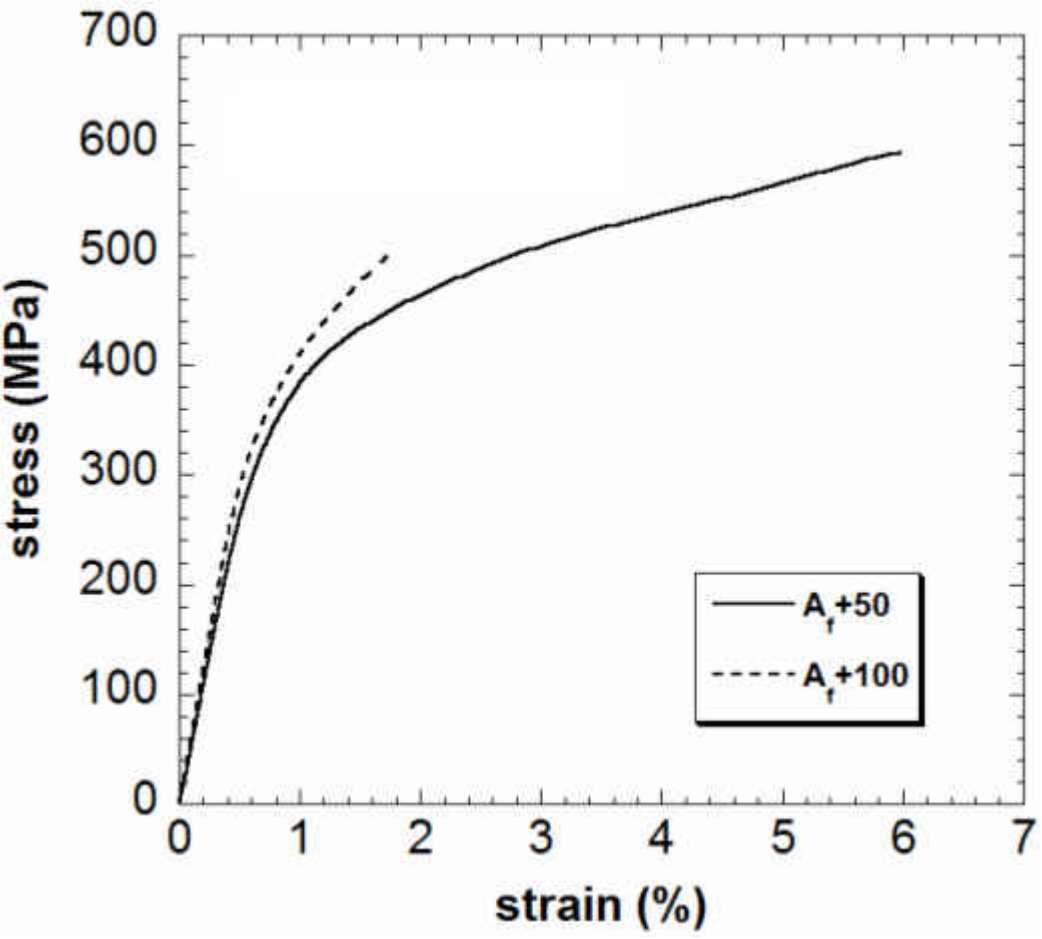

Figure 5.22: Stress-strain response of 110 μm x 100 μm wires at A_f+50°C and A_f+100°C

5.3.3 Constrained Recovery

Three 150 µm x 130 µm wires with different cross-sections (Table 5.3) were tested in constrained recovery. The wires were first thermally cycled twice in a furnace from room temperature to 250°C before being tested in the DMA. This was done to mimic the tests that were previously reported for the bulk specimens [Bigelow 2006]. The wires were thermally cycled from 50°C to 250°C twice for each stress level and the second cycles for each level were plotted. The first cycles were disregarded because when a sample is loaded to a higher stress level it takes one cycle to develop the microstructure at that new load. The results for constrained recovery are presented and discussed in Section 5.4.2.

Table 5.3: Average corner radius of electropolished wires tested in constrained recovery

	Corner Radius (µm)
Wire 1	37 (±5)
Wire 2	25 (±7)
Wire 3	6 (±4)

5.4 Comparison of Micron-scale Wires to Bulk Tension Samples

After analyzing the thermo-mechanical responses of the NiTiPd wires in the DMA they were compared to the bulk responses that had been previously reported [Bigelow 2006]. All of the results for the NiTiPd bulk samples presented in this work are from previous work [Bigelow 2006], and were re-plotted from the original raw data for better visual comparison to the results obtained in the DMA for NiTiPd wires of the same composition and bulk processing. The raw data for the bulk samples were converted to engineering strain to match the engineering strain plotted for the DMA results of the electropolished NiTiPd wires. For the purposes of direct comparison the DMA wire results for constrained recovery have been offset to reflect the same starting strains for each stress level as that of the bulk sample results. All of the results presented in this section are directly responsible for the actuator-type performance of the alloy, and will establish a confirmation that the DMA is a powerful tool for analyzing such properties.

5.4.1 Monotonic Tensile Testing

On comparing the martensitic stress-strain response of the two wires to the bulk sample, it can be seen that the moduli are comparable, with the bulk sample having a modulus of 44 GPa [Bigelow 2006], the 150 μm x 130 μm wire having a modulus of 44 ±2.5 GPa, and the 110 μm x 100 μm wire having a modulus of 38 ±2.5 GPa (Fig. 5.23).

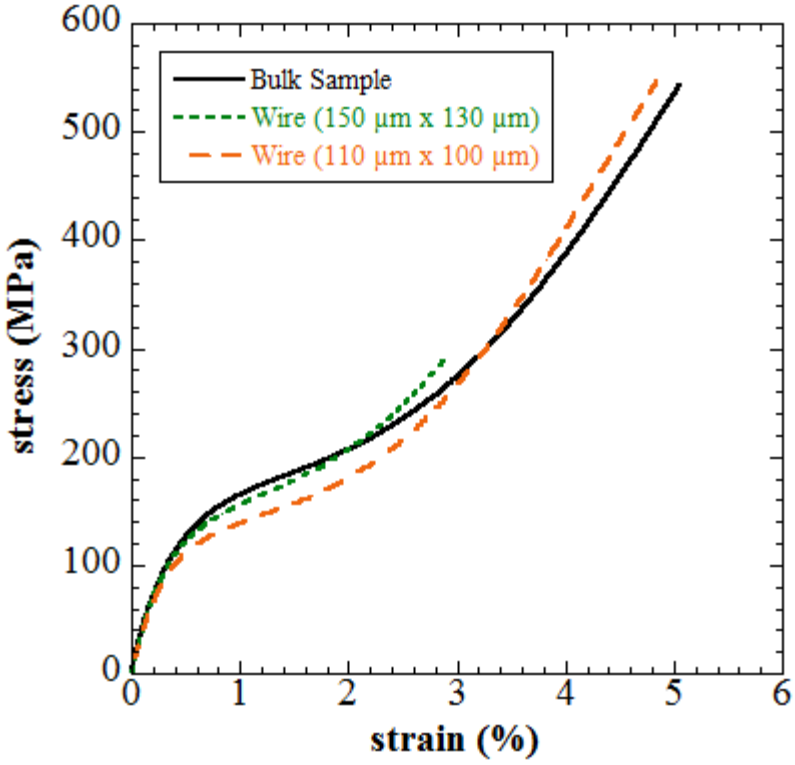

Figure 5.23: Comparison of the stress-strain response of NiTiPd wires and the bulk sample; tested at M_f-50^{o}C

For the austenitic stress-strain responses, the wires displayed a slightly lower elastic modulus of 72 ±2.5 GPa, as opposed to the 81 ±2.5 GPa for the bulk sample [Bigelow 2006], possibly due to retained martensite in the samples, even at Af+50°C (Fig. 5.24). The 110 µm x 100 µm wire was able to be loaded to the point of yielding, and was seen to plastically deform at a lower stress than that of the bulk.

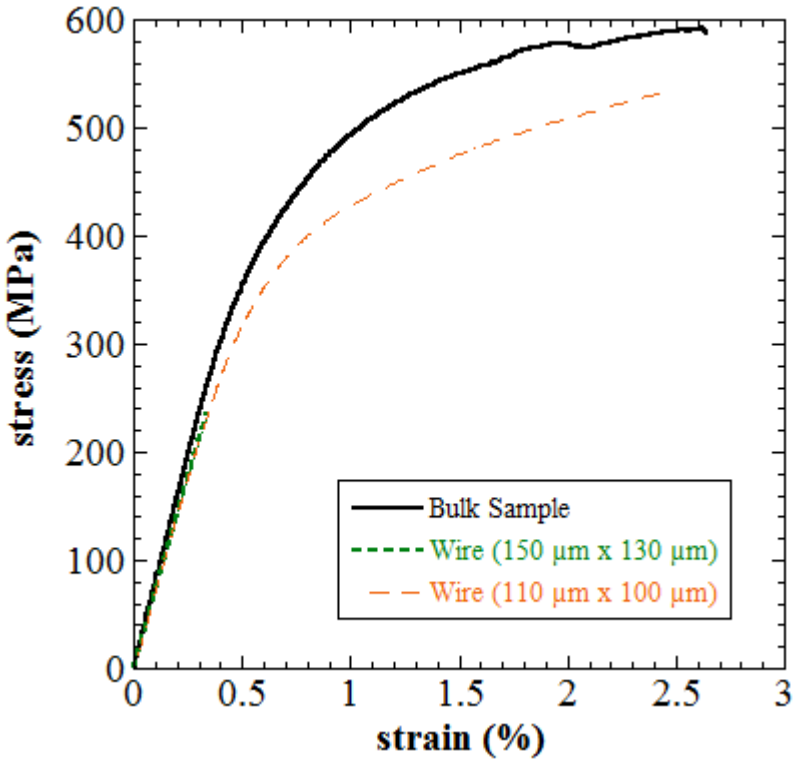

Figure 5.24: Comparison of the stress-strain response of NiTiPd wires and the bulk sample; tested at A_f+50°C

The critical stress for detwinning of martensite and the yield stress of austenite were determined and compared to that of the bulk sample which had been determined in previous work in Table 5.4 [Bigelow 2006]. The stresses for the onset of detwinning in the martensite phase and the onset of plasticity in the austenite are generally lower in the wires than in the bulk sample. This difference may be a result of variations in the uniformity of the wire that locally increases the stress while the reported values are based on a uniform cross-section.

Table 5.4: Comparison of the critical stress for detwinning in martensite and the yield stress of austenite for the wire and bulk samples

Sample	Martensite 0.2% Detwinning Stress (MPa)	Austenite 0.2% Yield Stress (MPa)
Bulk	131	443
150 μm x 130 μm	124	indeterminate
110 μm x 100 μm	112	387

5.4.2 Constrained Recovery Testing

A 150 μm x 130 μm and 110 μm x 100 μm wire were thermally cycled under no-load to ascertain if the DMA would respond well to no-load experiments of such fine wires. The heating curve responded quite clearly (Fig. 5.25). However, the DMA did not respond well to the cooling cycle and after the experiment completed it was realized that the wire had buckled and the probe did not re-position to maintain a no-load condition. On comparing the austenitic transformation temperatures the wires transformed at lower temperatures than that of the bulk

sample, but by no more than 12°C (Table 5.5). For this reason the wires had been thermally cycled twice in a furnace before being tested in the DMA under load.

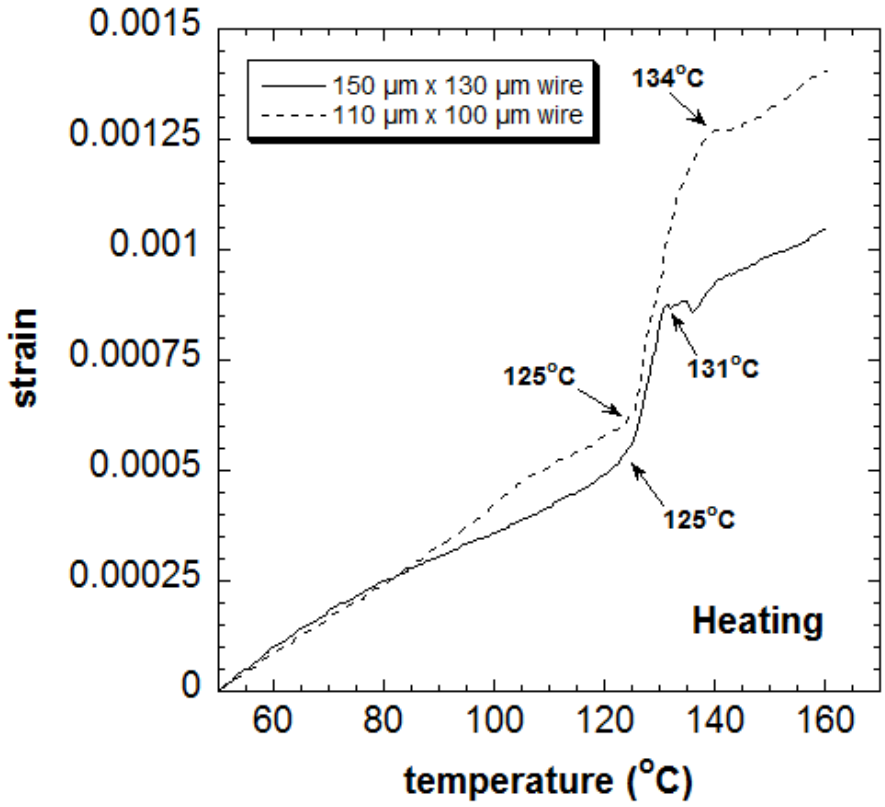

Figure 5.25: No-load heating of wires

Table 5.5: Transformation temperatures acquired during heating

	A_s (°C)	A_f (°C)
Bulk	133	143
150 µm x 130 µm Wire in DMA	125	131
110 µm x 100 µm Wire in DMA	125	134

At a hold stress of 99 MPa the wire with a cross-section that had a larger corner radius than the others displayed a response most similar, in terms of transformation strain, to the bulk sample which had a circular cross-section (Fig. 5.26). As the samples' edges got sharper the wire underwent less transformation strain as compared to the bulk sample. This can be attributed to more geometrical constraints placed on the system in terms of the orientation of individual variants for the case of sharper geometries. The transformation temperatures are lower in the wires at the 99 MPa hold stress than that of the bulk sample. The difference in the transformation temperatures can be attributed to intergranular stresses in the wire that affect the transformation temperatures. At a hold stress of 197 MPa the wires displayed more closely related values between each other for the transformation strains than for the 99 MPa hold stress case (Fig. 5.27).

At higher applied stresses, the effects of intergranular stresses are overcome and hence there is better agreement in the transformation temperatures between the wires and the bulk sample. The effect of wire geometry is also reduced since the higher applied stresses more strongly favor a certain distribution and orientation of variants. However, they did not display the same relative amount of transformation strain compared to the bulk sample at this stress level. The transformation temperatures of the wires were closer to that of the bulk sample for the 197 MPa hold stress case. At the final hold stress of 295 MPa the agreement between the wires' transformation temperatures and strains were closer than in the previous cases (Fig. 5.28). The difference between the transformation strains of the wires and the bulk sample were still present at this higher stress level. The transformation strains between the wires get closer as the applied

hold stress is increased (Fig. 5.29). They are most comparable to the bulk at the lower stress; however, get further from the bulk as stress is increased. In general at higher stresses there is an inadequate number of grains (about 200 in the case of the 150 μm x 130 μm wires) to satisfy stress and strain compatibility close to the wire surface while existing in an optimal distribution and orientation of variants as in the bulk sample. The wires effectively display the same irrecoverable strains as the bulk sample under each hold stress (Fig. 5.30). A summary of all the above results is presented in Tables 5.6 and 5.7.

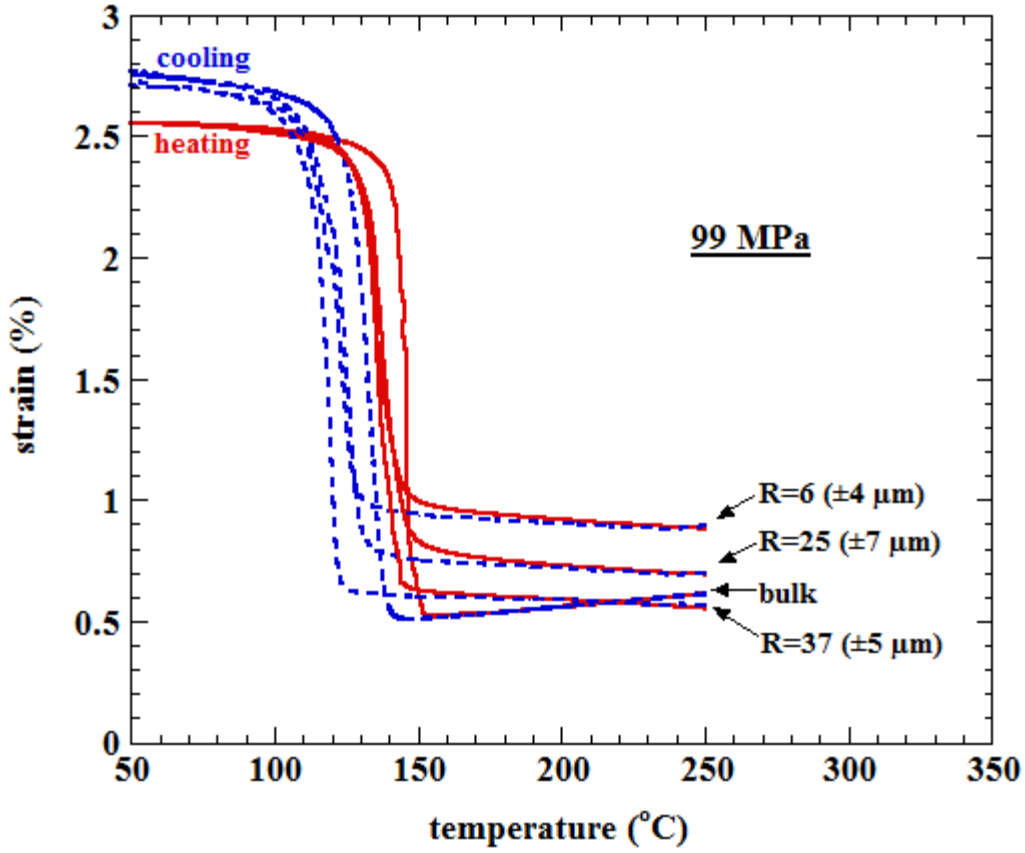

Figure 5.26: Comparison of constrained recovery response of wires and the bulk sample tested at 99 MPa

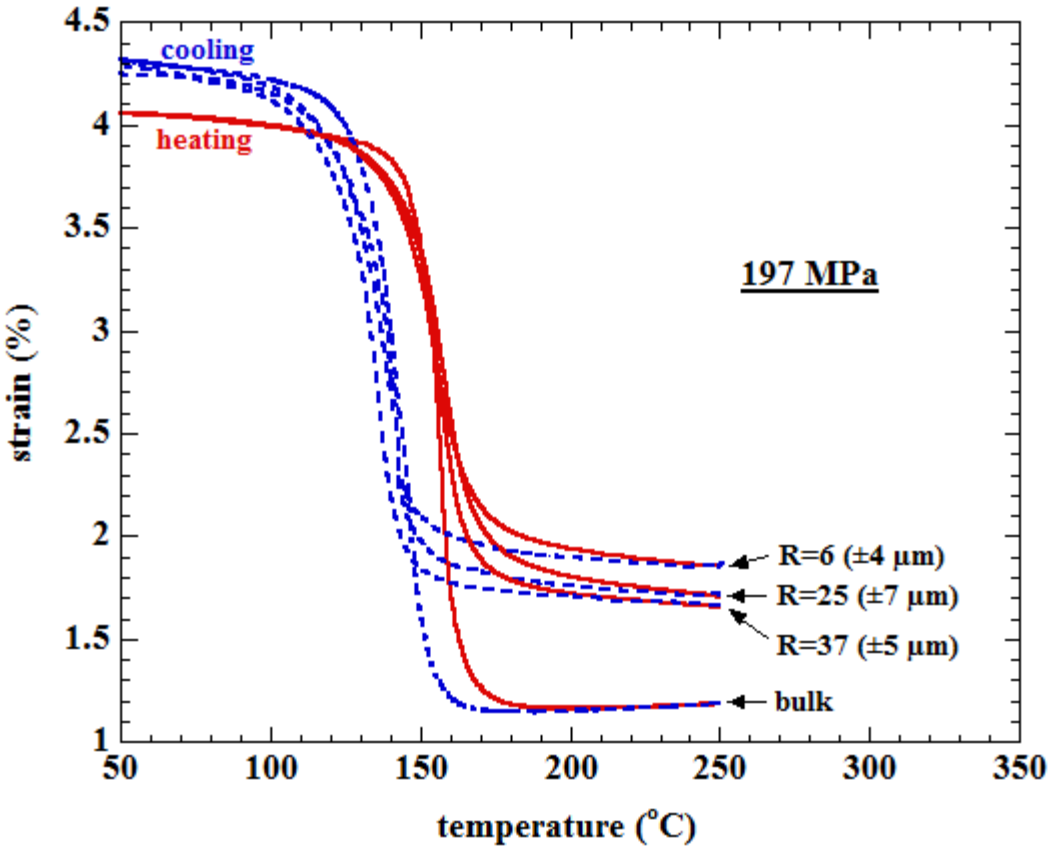

Figure 5.27: Comparison of constrained recovery response of wires and the bulk sample tested at 197 MPa

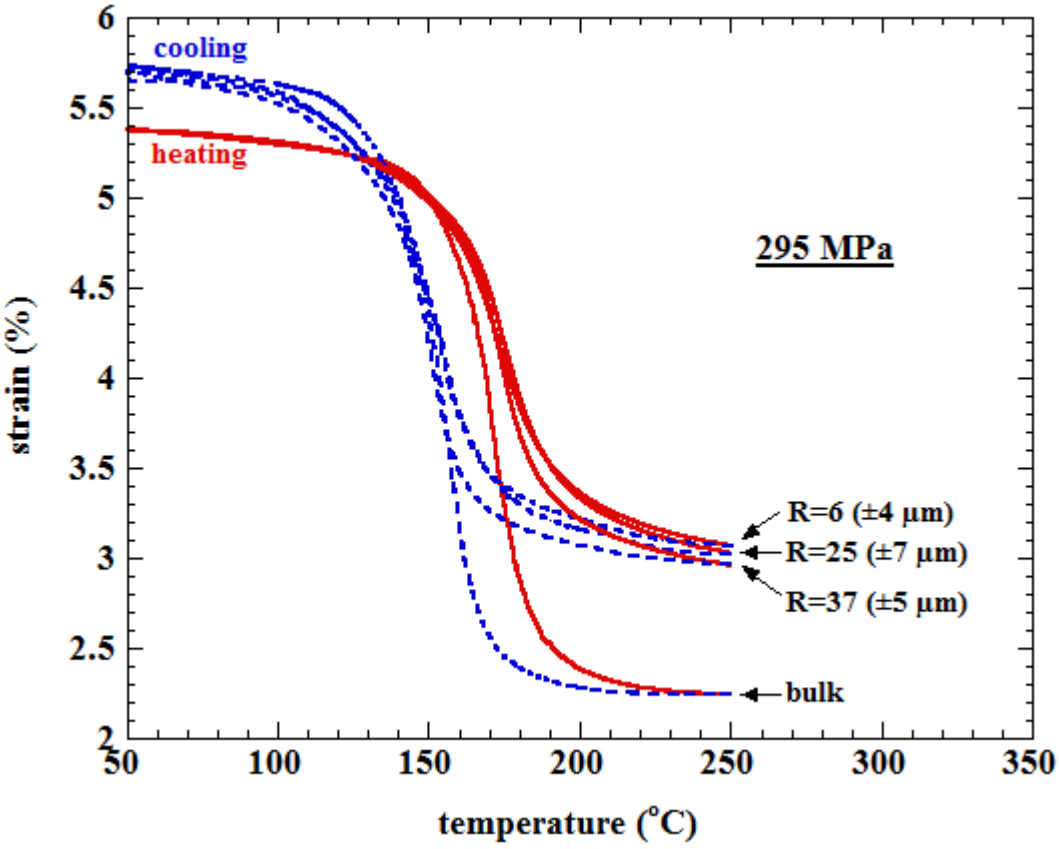

Figure 5.28: Comparison of constrained recovery response of wires and the bulk sample tested at 295 MPa

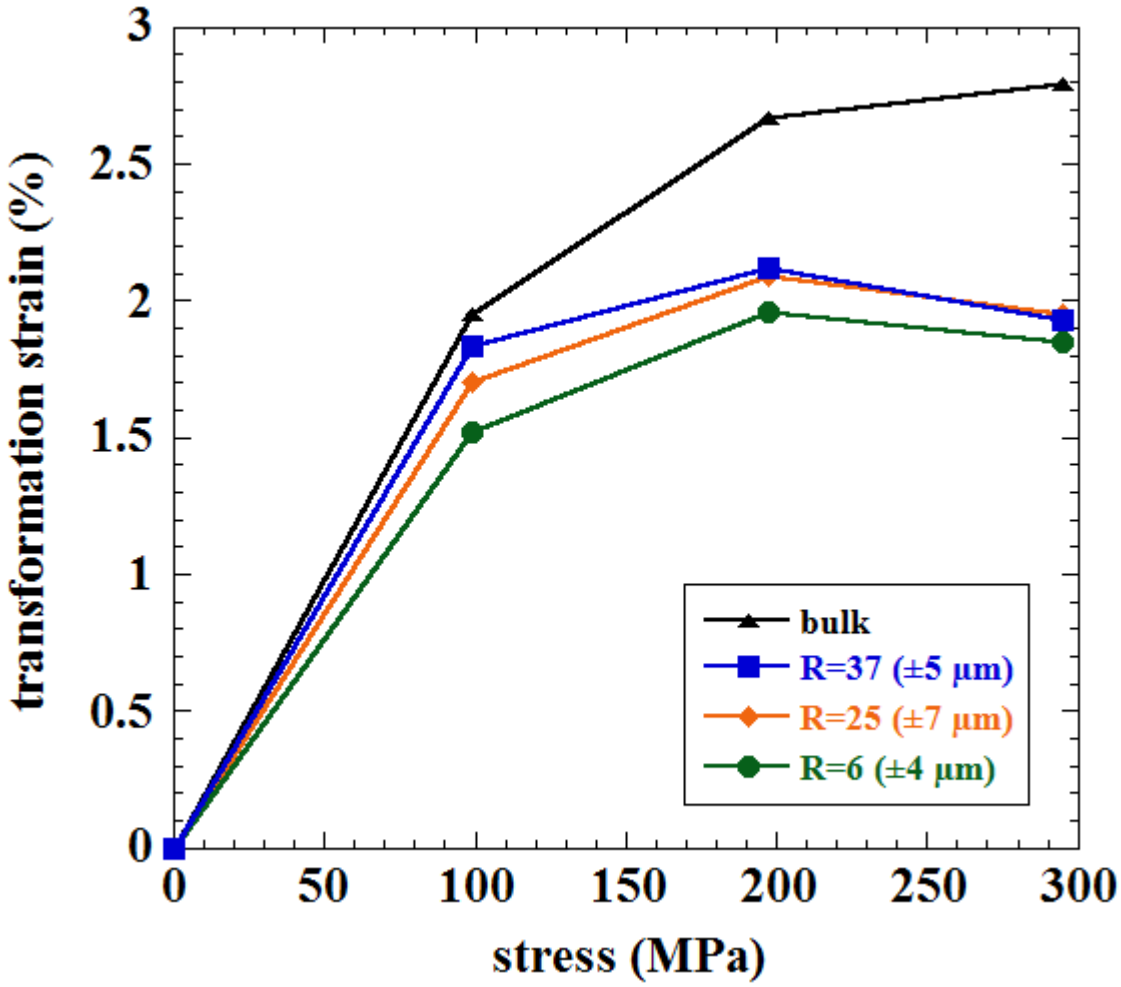

Figure 5.29: Comparison of transformation strain with holding stress for wires and the bulk sample

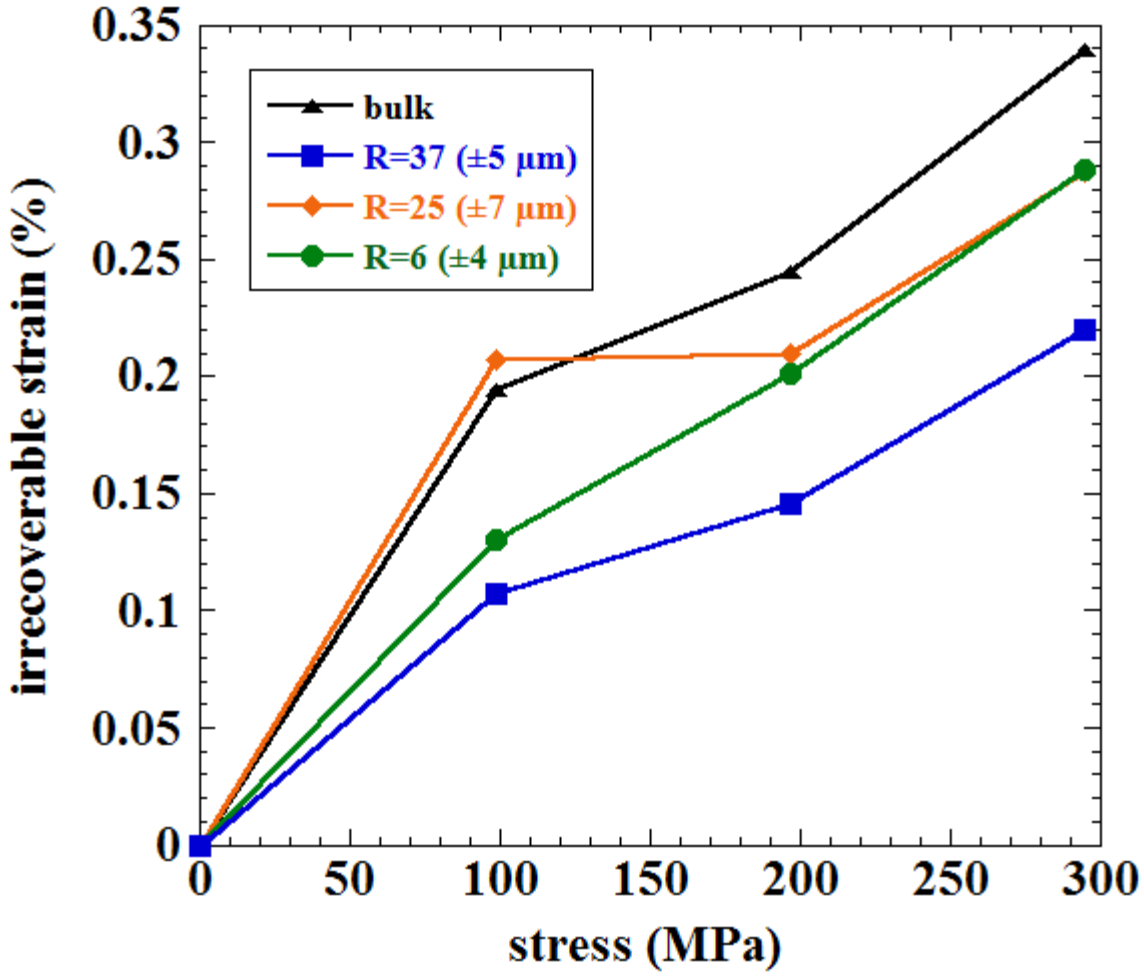

Figure 5.30: Comparison of irrecoverable strain with holding stress for wires and the bulk sample

Table 5.6: Transformation temperatures as a function of applied stress in constrained recovery for the three different micron-scale wires tested in the DMA, and the bulk sample tested on an MTS servo-hydraulic load frame

	Hold Stress (MPa)											
	99				197				295			
	M_f (°C)	M_s (°C)	A_s (°C)	A_f (°C)	M_f (°C)	M_s (°C)	A_s (°C)	A_f (°C)	M_f (°C)	M_s (°C)	A_s (°C)	A_f (°C)
Bulk	125	139	143	148	132	154	150	162	139	169	158	185
Wire 1 R= 37 ±5 µm	119	130	133	143	132	148	147	168	137	167	160	191
Wire 2 R= 25 ±7 µm	119	126	131	141	125	149	143	167	133	168	155	189
Wire 3 R= 6 ±4 µm	113	123	133	140	125	143	148	166	137	162	161	187

Table 5.7: Open-loop strain (ε_{OL}), transformation strain (ε_{TF}), and work output as a function of applied stress in constrained recovery for the three different micron-scale wires tested in the DMA, and the bulk sample tested on an MTS servo-hydraulic load frame

	Hold Stress (MPa)								
	99			197			295		
	ε_{OL} (%)	ε_{TF} (%)	Work Output (J/cm^3)	ε_{OL} (%)	ε_{TF} (%)	Work Output (J/cm^3)	ε_{OL} (%)	ε_{TF} (%)	Work Output (J/cm^3)
Bulk	0.19	1.95	1.93	0.24	2.67	5.26	0.34	2.79	8.23
Wire 1 R= 37 ±5 µm	0.11	1.83	1.81	0.15	2.12	4.18	0.22	1.93	5.69
Wire 2 R= 25 ±7 µm	0.21	1.70	1.68	0.21	2.09	4.13	0.29	1.95	5.76
Wire 3 R= 6 ±4 µm	0.13	1.52	1.51	0.20	1.96	3.86	0.29	1.85	5.45

CHAPTER SIX: CONCEPT FOR A VARIABLE AREA LABYRINTH SEAL

Turbines are mostly designed around a "cold-build" clearance where the unstressed, room temperature components are designed to have dimensions necessary to achieving minimum clearance at equilibrium conditions during operation. Considering that the blades expand faster than the shroud can accommodate, due to centrifugal forces, the shroud must be designed to be slightly larger in radius. Otherwise, the blades will contact the shroud causing significant wear, or even catastrophic failure. When the blades reach equilibrium the shroud continues expanding due to thermal effects. This means the clearance gap at equilibrium conditions will be wider than desired. By incorporating a labyrinth seal that is composed of shape memory actuators, a final clearance can be controlled after startup, and not have to depend on a "cold-build" clearance.

6.1 Background

Efficiency is a great concern with current turbine technologies. While it is desired to have each stage in the turbine operating at optimum efficiency, the inlet compressor stages are some of the most influential on the overall performance of a turbine. The inlet compressor stages are also usually the least hot areas in a turbine's flow-path area, and given the current temperature limitations for shape memory alloys (SMA), is the most likely area to first apply SMA actuators to aid in optimizing turbine efficiency. One of the biggest reasons for losses in a

turbine is the gaps present between the rotating components and the stationary components in the flow-path. In order to maximize the efficiency of a given turbine stage all the incoming flow must go through the rotating blades, and not "spill" over the top. Clearance control is usually the most cost-effective way to increase turbine efficiency, by preventing or minimizing the amount of fluid which "spills" over the blade tips [Chupp *et al.* 2006].

6.1.1 Clearance Control in Turbine Compressors

Maintaining the clearance gap between the rotating and stationary components is not easy because of the deflections each component undergoes during the path to thermal and axial force equilibrium (Fig. 6.1). Blade tip clearance is governed by the expansion of the shroud, blade and rotor, with respect to time. The internal variables that control the deflection of these components are pressure differentials, thermal stresses and centrifugal forces, among others.

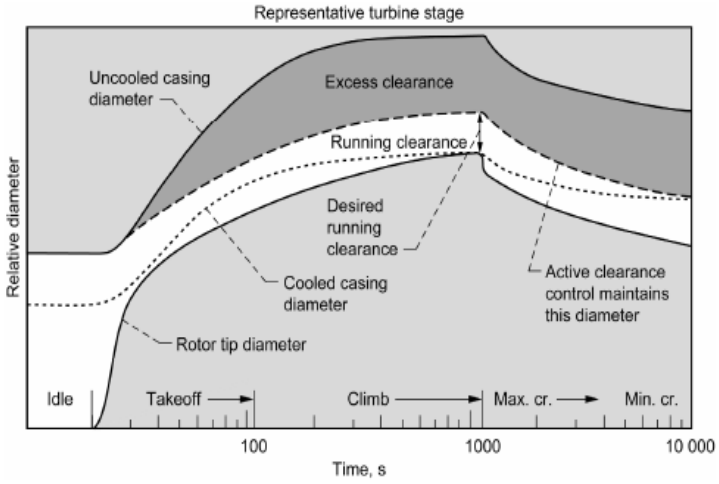

Figure 6.1: General clearances in a jet turbine during flight [Chupp *et al.* 2006]

Equation 6.1 is the general equation for an instantaneous tip clearance gap, where r_{shroud} is the inner wall position with respect to the center of rotation of the rotor, r_{rotor} is the outside surface position of the rotor with respect to its center of rotation and l_{blade} is the protrusion length of the blade out from the outer surface of the rotor to its outer tip.

$$Clearance\ (t) = r_{shroud}\ (t) - [r_{rotor}\ (t) + l_{blade}\ (t)] \quad \textbf{(6.1)}$$

The shroud radial deflection is governed by the pressure differential between the outer and inner walls, and thermal stresses. The pressure differential effect on the shroud radial deflection is dependent on the thickness of the shroud, the material properties of the shroud, the mean internal pressure of the turbine at that location and the shroud external pressure. The thermal stress effect on the shroud radial deflection is dependent on the thermal expansion of the shroud material, the thickness of the shroud, and the temperature at the inner and outer wall of the shroud.

The blade deflection is due to centrifugal forces and thermal stresses. The blade deflection due to centrifugal forces is dependent on the material properties, the unstressed length, and the angular speed of the blade. The blade deflection due to thermal stresses is dependant on the coefficient of thermal expansion, the unstressed length and the mean temperature of the blade.

The rotor deflection is also due to centrifugal forces and thermal stresses. The rotor deflection due to centrifugal forces is dependant on the material properties, the unstressed radius,

and the angular speed of the rotor. The rotor deflection due to thermal stresses is dependant on the coefficient of thermal expansion, the unstressed radius and the mean temperature of the rotor.

By knowing the radial position profiles for each component in the system with time a shape memory labyrinth seal can be designed to actuate with the timing necessary to avoid tip contact with the seal, and to achieve and maintain a minimum clearance during steady-state operation.

6.2 Proof-of-Concept

An ideal design would incorporate shape memory alloy segments positioned circumferentially about a center point, and actuate to accommodate the gap change between the "cold-build" radial position of the blade tip and the shroud. The SMA segments would need to have biasing force acting on them in order to provide the necessary two-stage actuation. Therefore, alloy segments of another material that does not have shape memory properties can be circumferentially positioned about the center point and overlap the SMA segments. By alternating the SMA segments with the biasing segments a seal can be made and two-stage actuation can be achieved (Figure 6.2).

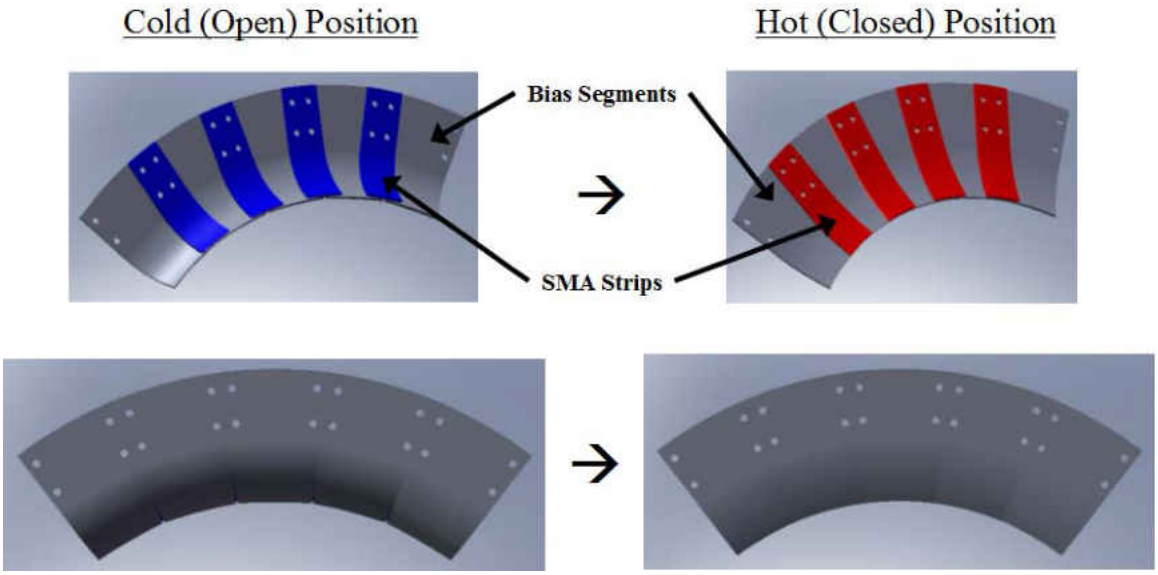

Figure 6.2: General design for proof-of-concept

6.2.1 Active vs. Passive Control

On starting the turbine, the blade tips expand rapidly and begin to come closer to the labyrinth seal tips, which are circumferentially positioned on the inner surface of the shroud. A minimum gap will be reached at a certain point, but the shroud will continue to expand at a faster rate as a result of thermal expansion and widen the gap. This can be called the "pinch-point." It is at this pinch-point that the labyrinth seal tips will need to extend radially inward to close the clearance gap.

The shape memory alloy segments can be actuated by either active or passive control. Passive control would mean that the SMA segments would transform when the ambient temperature causes it to do so. Once it reaches its austenite phase it would remain in that state

until the ambient temperature was reduced below the SMA's M_s temperature. The SMA would heat up by the hot flow inside the turbine and, when it reached its A_s temperature, it would begin to transform into its stronger austenite phase, thereby pushing against the biasing segments and changing the radial tip position of the labyrinth seal. Active control would mean that the SMA segments would be heated externally by a controlled heating source, i.e., electrical induction heating. The SMA can be actuated to position the seal at a higher radial position during startup by intrinsically heating the SMA to above its A_f temperature. Then, when the pinch-point is reached, the heating can be stopped and the SMA allowed to cool to the flow-path temperature, which would be less than the M_f temperature for the alloy. This means that the system will actually be active for a period of time, but transition to passive control once the induction heating is stopped. For a visualization of the transformation path the SMA will take during either passive or active/passive control for this application, see Figure 6.3.

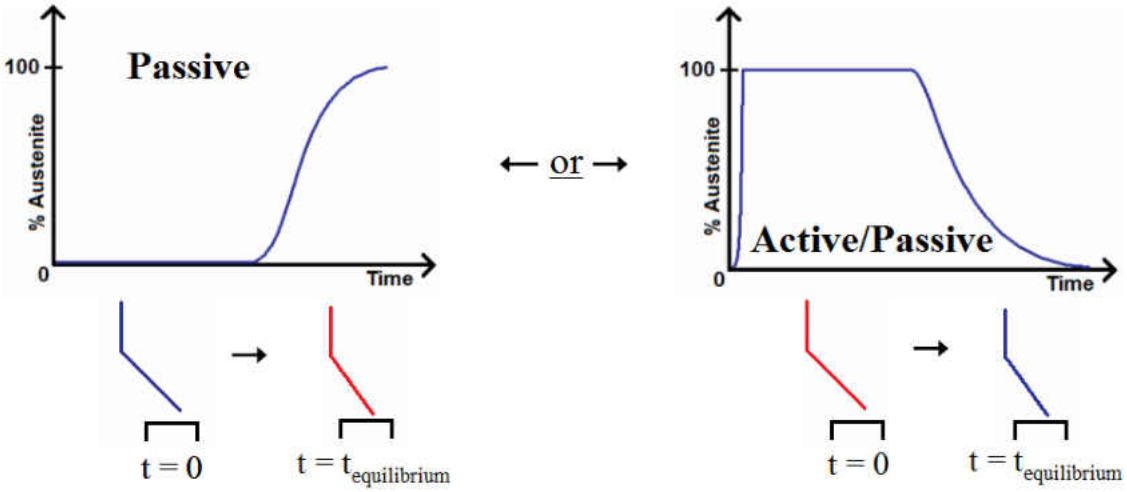

Figure 6.3: SMA phase path for both passive and active/passive control

6.2.2 Actuation Methods

There are several different ways in which the various SMA and bias segments can be positioned to provide two-stage actuation (Fig. 6.4). One method of actuation can involve the overlapping of bias segments with SMA strips fixed to the back ends, or between the overlap points. Another method can involve alternating overlapping SMA and bias segments. A combination of these ideas is also possible.

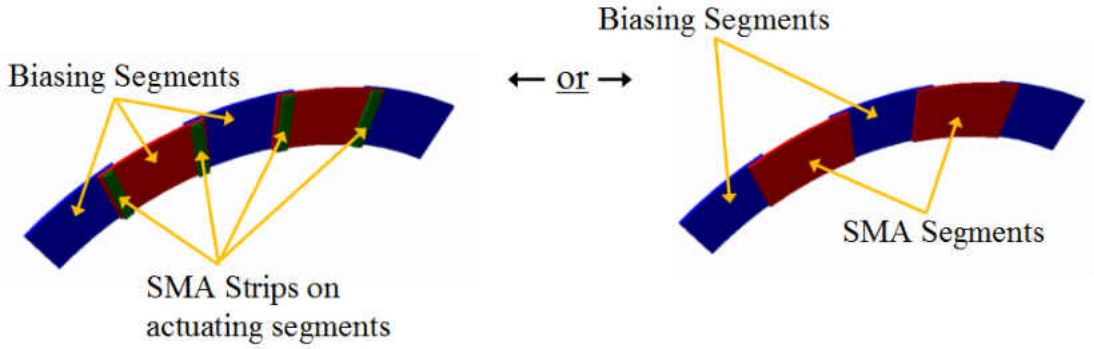

Figure 6.4: Methods of actuation for SMA labyrinth seal

6.3 Design Challenges and Issues

There are always challenges when trying to introduce a new material in a harsh environment. The environment inside a turbine is harsh given the extreme temperatures and pressures they can operate at. Corrosion and oxidation is also a concern and depends on the method of energy production, whether it be steam or gas.

6.3.1 Shape Setting of SMA Segments

The actuation force of the shape memory alloy segments on the biasing segments will be non-uniform. Biasing segments with varying thickness will have to be used to attain the proper biasing stress on the SMA segments to achieve the desired "cold-state" and "hot-state" positions. The SMA segments will also need to be shape set with a smaller bend angle than the biasing segments in order to provide a pre-stress for the SMA to do work against when actuated (Fig. 6.5).

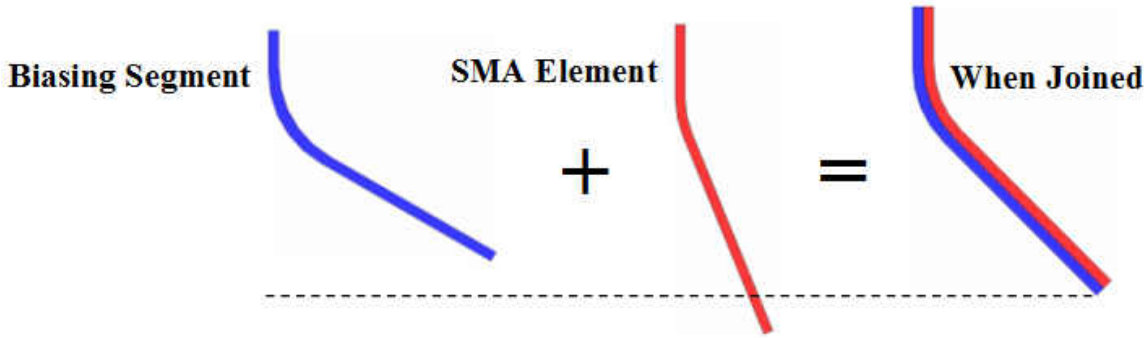

Figure 6.5: Method for producing desired pre-stress for SMA segments

6.3.2 Sealing between Segments

Given that the total radial displacement of the labyrinth seal tips should not need to exceed about 1.25 mm the total deflection of the labyrinth seal about its center of curvature will need to be on the order of 1°, depending on the height of the segments. The overlapping of the segments in the array will provide a natural mechanical seal to prevent any flow between the segments. The edges of the SMA segments will create a line contact with the contacting plane of the biasing segments and would slide during actuation. This would mean that the assembly would have to be impervious to flutter that may occur from the incoming flow. If the flow creates any kind of minimal gap between the overlapping segments it is possible for a boundary layer to form in the gap and hold the segments apart. Therefore, the rear segments of the assembly need to have a higher stiffness than the front segments, so that the more compliant segments will impact the stiffer rear segments during high-velocity flow, thus creating a better mechanical seal and preventing flutter. For the active/passive design, the SMA segments need to be placed in front of the biasing segments. Since the SMA segments will be in the martensitic

phase during steady-state operation it will be more compliant than the rear biasing segments. Martensitic NiTi-based alloys also have excellent damping capabilities, meaning the spring-back of the rear biasing segments will be greater than that of the SMA segments, thus maintaining a mechanical seal even during any possible flutter.

6.3.3 Temperature Limitations

Certain areas of a turbine can reach temperatures of over 1000°C, and since most current applications of shape memory alloys do not exceed 100°C further alloy development must be done. The compressor stages of several ground-based turbines usually do not exceed 450°C. Therefore, developing a shape memory alloy that can meet or exceed 450°C would go a long way towards integrating them into a turbine. The methodology established in this work is expected to aid in the quick and cheap development of a suitable shape memory alloy for use at high temperatures. At the time of writing, NiTiPt alloys show promise for use at high temperatures.

6.3.4 Cyclic Degradation

One of the main goals for turbine technologies is to have components that do not have to be serviced or replaced for at least 2-5 years. In order for a shape memory alloy labyrinth seal to be implemented it must also satisfy this criterion. Since the SMA segments do not undergo much deformation their cyclic performance can be expected to be favorable when actuated, and should not accumulate any plastic strain. NiTi has been able to perform for millions of cycles

after training when having to recover low strains and hence it is conceivable that new shape memory alloys will perform similarly.

6.3.5 Heat Transfer

As previously explained in section 6.2.1, active or passive control relies on the transformation temperatures of the alloy being used. It is essential that the labyrinth seal segments not contact the blade tips, so accurate design and implementation is vital to a viable SMA labyrinth seal. For passive control, the gas flow temperature will decide when the SMA segments will begin actuation, so the actuation speed of the labyrinth seal must not be too fast or it will contact the blade tips before steady-state is reached. Therefore, intimate knowledge of the heat transfer in the entire system that would affect the temperature profile of the SMA segments must be known, and accounted for in the design. For the active/passive control method, the SMA will be held at an open position for the entire startup and through the pinch-point, but knowing when to release it and allow for it to cool to the ambient flow temperature requires intimate knowledge of the heat transfer as well.

6.3.6 Corrosion and Oxidation

While NiTi has been extensively studied for its corrosion and oxidation resistance the HTSMAs being developed across the world have not been put under such rigorous testing for such properties yet. Electropolishing NiTi to create a thin layer of TiO_2 or coating it with a barrier layer is quite common for current applications, but turbine environments are much more

hostile than the current environments SMAs are used in. Considering that NiTi begins a rather rapid growth of oxidation above 600°C it is likely that some sort of special coating or isolation of the SMA components altogether might be necessary to apply SMA inside harsh turbine environments in the future.

CHAPTER 7: CONCLUSIONS

Micron-scale wires were extracted by wire electrical-discharge machining (EDM) from a $Ni_{29.5}Ti_{50.5}Pd_{20}$ bulk tensile specimen, and were subsequently electropolished to remove the heat-affected zone (HAZ) from the surfaces of the wires, and to reduce the cross-section dimensions for adequate thermo-mechanical testing in a dynamic mechanical analyzer (DMA). The results of these thermo-mechanical tests were compared to previous results acquired from corresponding $Ni_{29.5}Ti_{50.5}Pd_{20}$ bulk tensile specimens at NASA Glenn Research Center.

For purposes of direct comparison, electrical discharge machining (EDM) was used to extract wires from the bulk samples. Characterization of the wires' heat affected zone (HAZ) was undertaken using scanning electron microscopy (SEM) and transmission electron microscopy (TEM). TEM studies of the wires after EDM identified the depth affected by the EDM process and hence the layer that needed to be removed to produce test samples capable of exhibiting thermo-mechanical data representative of the core material. Electropolishing with methanolic sulfuric acid was chosen as the method to remove the HAZ from the wires and selecting the right electrolyte composition for electropolishing $Ni_{29.5}Ti_{50.5}Pd_{20}$ needed to be established. By varying the electropolisher parameters, i.e., input voltage and time, a process was established for removing the HAZ from the surfaces of the wires, while maintaining uniformity in the cross-section over the length of the sample. In addition, by varying the input voltage between the established electropolishing voltage (6-8 volts) the corner radius of the wires' cross-sections were controlled to be different from one another.

Precise measurement of the wires' cross-section area was required for determination of the mechanical properties from DMA testing. Given the small cross-section of the wires tested (of the order of 100 μm) and the delicate handling necessary for such wires it was difficult to calculate the area of the wire cross-sections by non-destructive means. Therefore, a methodology was established to measure the wire cross-section dimensions by using laser scanning confocal microscopy (LSCM) in 3-D confocal viewing mode. This method not only allowed for precise area measurement of the wires' cross-sections, but provided the tools necessary to measure the corner radius of these wires' cross-sections as well.

Once valid test samples were produced a DMA was used to characterize the thermo-mechanical properties of the $Ni_{29.5}Ti_{50.5}Pd_{20}$ wires. Aside from the prescribed DMA calibration procedure provided by the manufacturer, Perkin Elmer, additional instrument compliance was needed based on monotonic tensile test results of stainless steel, aluminum and superelastic NiTi wires. Constrained recovery tests at increasing stress levels of 99, 197 and 295 MPa were then performed on micron-scale wires with overall dimensions of 150 μm x 130 μm (though they had varying corner radii to represent different cross-section shapes); with wires having an average corner radii of 37 μm, 25 μm and 6 μm, respectively. Isothermal tensile tests were also performed on two different sets of micron-scale $Ni_{29.5}Ti_{50.5}Pd_{20}$ wires in a DMA, at temperatures of 73°C (M_f-50°C) and 193°C (A_f+50°C) to ensure fully martensitic and fully austenitic structures, respectively; with one set having overall cross-section dimensions of 150 μm x 130 μm, and the other set having overall cross-section dimensions of 110 μm x 100 μm.

On comparing the results from NASA's previous testing on bulk tensile specimens with that of the micron-scale wires, the overall thermo-mechanical trends were accurately captured by the micron-scale wires for both the constrained recovery, and monotonic tensile tests. Specifically, there was excellent agreement between the stress-strain response in both the martensitic and austenitic phase, the transformation strains at lower stresses in constrained recovery, and the transformation temperatures at higher stresses in constrained recovery. The transformation strains were sensitive to the corner radius of the wires at lower stresses in constrained recovery, and then became outweighed at higher stresses by the representative number of grains in the cross-section.

Shape memory alloys (SMAs) have been used in many aerospace and aeronautical applications, but have yet to be implemented in turbomachinery because both ground-based and jet turbines have internal operation temperatures that far exceed the operational limit of any commercially available SMA. Other factors, such as high pressures, vibrations, and creep effects from rotating components, could also affect the behavior of SMAs. While it is desired to have each stage in the turbine operating at optimum efficiency, the inlet compressor stages are some of the most influential on the overall performance of a turbine. The inlet compressor stages are also usually the least hot areas in a turbine's flow-path area, thus are the most likely area to first apply SMA-based actuators to aid in optimizing turbine efficiency. One of the ways to make a compressor stage more efficient is to reduce the gap between the compressor blade tip and the shroud. By allowing more area between the blade tips and the shroud less volume of gas will be compressed, thus negating the purpose of the compressor stage. Complex seals are used in

turbomachinery to minimize "spillage" over turbine blades, but the main drawback to those seals is they are made of rigid components which only change shape due to their respective coefficient of thermal expansion. This work additionally has presented a concept for a variable area labyrinth seal which uses high-temperature shape memory alloys (HTSMAs) to further reduce the gap between the compressor blade tips and the shroud.

In order for NiTi-based SMAs to be implemented in high-temperature environments elemental additions and special heat treatments must be used. Expensive elements, like platinum and palladium, are encouraging ternary additions that raise the transformation temperatures of NiTi. Melting large billets and machining tensile samples is expensive when trying to optimize the thermo-mechanical properties necessary for a given application. By melting smaller buttons and using a process that comprises both wire-EDM and electropolishing to produce thin wires, the thermo-mechanical trends can be realized in a DMA, and be considered representative of a bulk specimen. Once an optimized response is acquired, large-scale billets can be produced, and bulk samples extracted from those billets can be used to further evaluate the material, e.g., dimensional stability, creep, etc. By improving upon the methodology presented in this work through optimization of the EDM and electropolishing parameters, a more quantitatively similar set of thermo-mechanical data to a bulk specimen can be expected.

The results of the experiments on $Ni_{29.5}Ti_{50.5}Pd_{20}$ described in this work are very encouraging and can potentially bring down the cost of shape memory alloy development in the future. In driving down the costs associated with HTSMA development, less-expensive and vigorous alloy development can commence which could accelerate the advancement of shape

memory alloy use in high-temperature environments. With the costs of electricity generation for consumer use continually increasing and jet fuel costs poised to rise in the near future and beyond, achieving greater turbine efficiency sooner, rather than later, can help to offset these costs in the near-term. It is expected that the work presented in this thesis can help bring the use of HTSMAs in turbomachinery closer to reality.

REFERENCES

Berg B., "Mechanics of NiTi Fatigue for Vascular Stent Design", *Society of Engineering Science: 45th Annual Technical Meeting* (2008).

Bigelow G., "Effects of Palladium Content, Quaternary Alloying, and Thermomechanical Processing on the Behavior of Ni-Ti-Pd Shape Memory Alloys for Actuator Applications", NASA/TM – 2008-214702 (2008).

Bigelow G. S., Thesis, "Effects of Palladium Content, Quaternary Alloying, and Thermomechanical Processing on the Behavior of Ni-Ti-Pd Shape Memory Alloys for Actuator Applications", Colorado School of Mines, 2006.

Calkins F. T., Mabe J. H., Butler G. W., "Boeing's Variable Geometry Chevron: Morphing Aerospace Structures for Jet Noise Reduction", Proc. of SPIE Vol. 6171 (2006).

Carpenter B. F., Head R. J., Gehling R., "Shape Memory Actuated Gimbal", Proc. of SPIE Vol. 2447 (1995), pp. 91-101.

Chupp R. E., Hendricks R. C., Lattime S. B., Steinetz B. M., "Sealing in Turbomachinery", NASA/TM – 2006-214341 (2006).

DeCastro J. A., Melcher K. J., Noebe R. D., "System-Level Design of a Shape Memory Alloy Actuator for Active Clearance Control in the High-Pressure Turbine", NASA/TM – 2005-213834 (2005).

Diakunchak I. S., U.S. Patent 6,926,495 (2005).

Duerig T., Pelton A., Stöckel D., "An Overview of Nitinol Medical Applications", Materials Science and Engineering A, Vols. 273-275, (1999), pp. 149-160.

Dunne J. P., Hopkins M. A., Baumann E. W., Pitt D. M., White E. V., "Overview of the SAMPSON Smart Inlet", Proc. of SPIE Vol. 3674 (1999), pp. 380-390.

Dynalloy, Inc., Costa Mesa, CA, http://www.dynalloy.com/pdfs/TCF1140RevD.pdf

Elliott R. S., Shaw J. A., Triantafyllidis N., "Stability of Thermally-Induced Martensitic Transformations in Bi-Atomic Crystals", Journal of the Mechanics and Physics of Solids, Vol. 50, (2002), pp. 2463-2493.

Elorriaga J., U.S. Patent 6,102,307 (2000).

ESMA, Inc., South Holland, IL, http://www.esmainc.com/products/pdf/electropolishing/e1085-1s.pdf

Evans D. H., U.S. Patent 5,203,673 (1992).

Funakubo H., "Shape Memory Alloys", Gordon and Breach Science Publishers, New York, 1987.

Fushimi K., Stratmann M., Hassel A. W., "Electropolishing of NiTi Shape Memory Alloys in Methanolic H_2SO_4", Electrochimica Acta, Vol. 52, (2006), pp. 1290-1295.

Golberg D., Xu Y., Murakami Y., Morito S., Otsuka K., "Characteristics of $Ti_{50}Pd_{30}Ni_{20}$ High-Temperature Shape Memory Alloy", Intermetallics, Vol. 3, (1995), pp. 35-46.

Hsieh S. F., Chen S. L., Lin H. C., Lin M. H., Chiou S. Y., "The Machining Characteristics and Shape Recovery Ability of Ti-Ni-X (X = Zr, Cr) Ternary Shape Memory Alloys Using the Wire Electro-Discharge Machining", International Journal of Machine Tools & Manufacture, Vol. 49, (2009), pp. 509-514.

Huang X. and Liu Y., "Effect of Annealing on the Transformation Behavior and Superelasticity of NiTi Shape Memory Alloy", Scripta Materialia, Vol. 45, (2001), pp. 153-160.

Humbeeck J. V., "Non-Medical Applications of Shape Memory Alloys", Materials Science and Engineering A, Vols. 273-275, (1999), pp. 134-148.

James V. L., U.S. Patent 4,196,856 (1980).

Kim J. I., Liu Y., Miyazaki S., "Ageing-Induced Two-Stage R-Phase Transformation in Ti – 50.9at.%Ni", Acta Materialia, Vol. 52, (2004), pp. 487-499.

Lam S., Schoenwald K. D., Snyder D. W., Watson D. S., "Detailed Design Report for a Debris Free Control Release Mechanism Utilizing NiTi Shape Memory Alloys for the National Aeronautics and Space Administration", Senior Design Project – University of Central Florida (Spring 2007).

Lattime S. B., Steinetz B. M., "Turbine Engine Clearance Control Systems: Current Practices and Future Directions", NASA/TM – 2002-211794 (2002).

Lattime S. B., Steinetz B. M., Robbie M. G., "Test Rig for Evaluating Active Turbine Blade Tip Clearance Control Concepts", NASA/TM – 2003-212533 (2003).

Lin B., Gall K., Maier H. J., Waldron R., "Structure and Thermomechanical Behavior of NiTiPt Shape Memory Alloy Wires", Acta Biomaterialia, Vol. 5, (2009), pp. 257-267.

Lin H. C., Lin K. M., Cheng I. S., "The Electro-Discharge Machining Characteristics of TiNi Shape Memory Alloys", Journal of Materials Science, Vol. 36, (2001), pp. 399-404.

Lindquist P. G., Dissertation, "Structure and Transformation Behavior of Martensitic Ti – (Ni, Pd) and Ti – (Ni, Pt) Alloys", University of Illinois at Urbana-Champaign, 1988.

Lizotte A. M., Allen M. J., "Twist Model Development and Results from the Active Aeroelastic Wing F/A-18 Aircraft", NASA/TM – 2005-212861 (2005).

Mabe J. H., Calkins F. T., Alkislar M. B., "Variable Area Jet Nozzle Using Shape Memory Alloy Actuators in an Antagonistic Design", Proc. of SPIE Vol. 6930, (2008).

Mavroidis C., "Development of Advanced Actuators Using Shape Memory Alloys and Electrorheological Fluids", Res Nondestr Eval, Vol. 14, (2002), pp. 1-32.

Menard K. P., "Dynamic Mechanical Analysis: A Practical Introduction", CRC Press LLC, Boca Raton, 1999.

Miao W., Mi X., Wang X., Li H., "Electropolishing Parameters of NiTi Alloy", Trans. Nonferrous Met. Soc. China, Vol. 16, (2006), pp. 130-132.

Miller D. A. and Lagoudas D. C., "Influence of Cold Work and Heat Treatment on the Shape Memory Effect and Plastic Strain Development of NiTi", Materials Science and Engineering A, Vol. 308, (2001), pp. 161-175.

Miura S., Mogi M., Ohura Y., Hamanaka H., "The Super-Elastic Property of the Japanese NiTi Alloy Wire for Use in Orthodontics", American Journal of Orthodontics and Dentofacial Orthopedics, Vol. 90, (1986), pp. 1-10.

Nandiraju D., Thesis, "Commissioning of a Dynamic Mechanical Analyzer for the Characterization of Low Temperature NiTiFe Shape Memory Alloys", University of Central Florida, 2006.

Nishiura T., Hayashi K., Nishida M., "Electropolishing Conditions for Trace Analysis of B19' Martensite in Ti – Ni Shape Memory Alloys", Materials Science and Engineering A, Vols. 481-482, (2008), pp. 446-451.

Noebe R., Biles T., Padula S. A., "NiTi-based High-Temperature Shape-Memory Alloys: Properties, Prospects, and Potential Applications" in *Advanced Structural Materials: Properties, Design Optimization, and Applications*, edited by Sobojyejo W. O. and Srivatsan T. S., CRC Press LLC, Boca Raton, 2006.

Orgéas L., Favier D., "Stress-Induced Martensitic Transformation of a NiTi Alloy in Isothermal Shear, Tension and Compression", Acta Materialia, Vol. 46, (1998), pp. 5579-5591.

Otsuka K., Ren X., "Physical Metallurgy of Ti-Ni-based Shape Memory Alloys", Progress in Materials Science, Vol. 50, (2005), pp. 511-678.

Otsuka K. and Wayman C. M., "Shape Memory Materials", Cambridge University Press, New York, 1998.

Padula S., Noebe R., Bigelow S., Culley D., Stevens M., Penney N., Gaydosh D., Quackenbush T., Carpenter B., "Development of a HTSMA-Actuated Surge Control Rod for High-Temperature Turbomachinery Applications", AIAA Structures, Structural Dynamics, and Materials Conference, April, 2007.

Perkin Elmer, Waltham, MA, http://www.perkinelmer.com.

Pohl M., Heßing C., Frenzel J., "Electrolytic Processing of NiTi Shape Memory Alloys", Materials Science and Engineering A, Vol. 378, (2004), pp. 191-199.

Renggli B. J., U.S. Patent 7,174,704 (2007).

Rey N. M., Tillman G., Miller R. M., Wynosky T., Larkin M. J., Flamm J. D., Bangert L. S., Proc. of SPIE, Vol. 4332, (2001), 371-382

Roy D., Buravalla V., Mangalgiri P. D., Allegavi S., Ramamurty U., "Mechanical Characterization of NiTi SMA Wires Using a Dynamic Mechanical Analyzer", Materials Science and Engineering A, Vol. 494, (2008), pp. 429-435.

Ryhänen J., Dissertation, "Biocompatibility Evaluation of Nickel-Titanium Shape Memory Metal Alloy", University of Oulu, 1999.

Sanders B., Crowe R., Garcia E., "Defense Advanced Research Projects Agency – Smart Materials and Structures Demonstration Program Overview", Journal of Intelligent Material Systems and Structures, Vol. 15, (2004), pp. 227-233.

Schetky L. M. and Steinetz B. M., “Shape Memory Alloy Adaptive Control of Gas Turbine Engine Compressor Blade Tip Clearance”, Proc. of SPIE Vol. 3326, (1998), pp. 346-354.

Shaw J. A. and Kyriakides S., “Thermomechanical Aspects of NiTi”, J. Mech. Phys. Solids, Vol. 43, (1995), pp. 1243-1281.

Shimizu S., Xu Y., Okunishi E., Tanaka S., Otsuka K., Mitose K., “Improvement of Shape Memory Characteristics by Precipitation-Hardening of Ti – Pd – Ni Alloys”, Materials Letters, Vol. 34, (1998), pp. 23-29.

Stöckel D., “Status and Trends in Shape Memory Technology”, Proc. Actuators VDI/VDE Bremen, (1992), pp. 79-84.

Sulfuric Acid MSDS, Fisher Scientific, ACC# 22350, Revision #15, Updated 2/13/2008.

Theisen W. and Schuermann A., “Electro Discharge Machining of Nickel – Titanium Shape Memory Alloys”, Materials Science and Engineering A, Vol. 378, (2004), pp. 200-204.

Tian Q., Chen J., Chen Y., Wu J., “Oxidation Behavior of TiNi – Pd Shape Memory Alloys”, Z. Metallkd., Vol. 94, (2003), pp. 36-40.

Tseng W. Y., U.S. Patent 5,035,573 (1991).

Webster J., “Opportunities for Adaptive Optimisation of Gas Turbine Systems”, Proc. of SPIE Vol. 4763, (2003), pp. 101-105.

Wu J. and Tian Q., “The Superelasticity of TiPdNi High Temperature Shape Memory Alloy”, Intermetallics, Vol. 11, (2003), pp. 773-778.

Wu M. H., “Fabrication of Nitinol Materials and Components”, Proc. of SMST, (2001), pp. 285-292.

Wu M. H. and Schetky L. M., “Industrial Applications for Shape Memory Alloys”, Proc. of SMST, (2000), pp. 171-182.